| | |
|---|---|
| Title | Natural Convection induced by Internal Heat Generation |
| Author(s) | Tasaka, Yuji |
| Citation | 北海道大学. 博士(工学) 甲第7288号 |
| Issue Date | 2005-03-25 |
| DOI | 10.14943/doctoral.k7288 |
| Doc URL | http://hdl.handle.net/2115/28093 |
| Type | theses (doctoral) |
| File Information | thesis.pdf |

# Natural Convection induced by Internal Heat Generation

Presented by
**Yuji TASAKA**

Laboratory for Flow Control,
Graduate School of Engineering,
Hokkaido University

Supervised by
Prof. Dr. Dr. Y. Takeda

January 16, 2005

# Natural Convection induced by Internal Heat Generation

Thesis for Doctor of Engineering at Hokkaido University
Submitted at Dec. 10, 2004

Advisory Committee:

Prof. Dr.-Eng. Dr.-Sci. Yasushi Takeda, Chair/Chief examiner
Prof. Dr.-Eng. Shigeo Fujikawa, Co-examiner
Prof. Dr.-Sci. Masaki Sano, Co-examiner

# Acknowledgement

In the first place I with to express my gratitude to my supervisor Prof. Dr. Dr. Y. Takeda for giving me the opportunity to accomplish this work and for his helpful advises. His extensive perspective on the studies of engineering and of science has made my growth, and his international sense removed a barrier for the world made by myself.

I would like to thank Assoc. Prof. Dr. Y. Murai for giving me chances to discuss various subjects. I have been impressed with his knowledge and experience, and he is my very high aim. I wish to thank Tech. Mr. Sampo for supporting my research by his excellent techniques. I hope that all students in my lab. show respect for his great works.

I would like to thank Dr. Greg King (Warwick Univ.) for his helpful suggestions about my study and for revising my papers kindly. I wish to thank Dr. T. Yanagisawa (IFREE, JAMSTEC) for giving me good experience to discuss our project with researchers in various fields.

I have great respect for Dr. M. Kiya, Prof. Dr. M. Mochizuki and Dr. H. Ishikawa. They have been warmly keeping my growth as a researcher after they left our lab. I am fortunate to lean under respectable-great researchers.

I wish to thank T. Ohkubo and T. Ishiyama, my best friends. I never forget the hard time in which we overcame together. I want to express my best regards for the members of my research group; K. Yonekura, Y. Kudoh, R. Goto, H. Kitaura and M. Yoshida. They are also my familiar juniors, my friends, and good debaters.

Finally, I want to thank my parents, Takeshi and Sanae, and my sisters, Emi and Yuki for supporting my college life and for warmly watching me. I never forget all kindness receiving from Takanobu Hiroyama, my brother.

With my whole heart,
田坂　裕司

# Table of Contents

## Chapter 1

# Introduction

## 1.1 Preface

Natural convection in a shallow fluid layer makes a beautiful convection pattern at various places, e.g. a cloud pattern in the sky, water circulation in a paddle on the ground after the rain. Such art of Nature certainly has melted someone's heart since ancient times.

Bénard first dealt with this phenomenon as a physical problem in his work [1]. Since his works at early 1900s, it has been continuously investigated as an extremely fundamental phenomenon of a thermal convection appearing in engineering and science fields until now. Rayleigh added a mathematical explanation to a formation of the convection pattern by stability analysis [2]. After that, mathematicians have investigated this phenomenon as a typical problem of a pattern formation and a bifurcation of a solution [3]. In the long history of the investigation, the study of this problem has taken in many elements, e.g. influences of a rotation and a magnetic field [4, 5], effects of surface tension [6, 7], and it putted off great achievements respectively (See Koschmieder (1993) [8]). It has, however, misplaced important elements, "internal heat generation" and "low Prandtl number fluid", on the way.

## 1.2 Background & literature survey

### 1.2.1 Internally heated convection

Natural convection induced by internal heat generation exists everywhere in nature. Examples are motion in the atmosphere [9, 10, 11] where heat generation is generated by absorption of sunlight, and mantle convection in the earth [12]–[15] where heat is generated by radioactive decay of isotopes. In the artificial structures, microwave ovens and induction heater such as an electric melter generate internal heat. In the event of hypothetical core meltdown of the nuclear reactor heat generation is internal. There are many systems in which this phenomenon becomes dominant in geophysics and thermal engineering. Recently, the problems of such internally heated convection are investigated as realistic problems in actual equipments [16]–[20] or in evolution of the earth [21] by mainly using a numerical simulation. Since early 1970s, however, to our knowledge, there have been no fundamental investigations of this problem, and then there are unsolved problems in the internally heated convection.

Despite the importance of internal heat generation, there are few systematic investigations of its effects. Most of previous works have only considered the much simpler case in which heat generation is uniform overall the fluid layer and a thermal boundary condition at the bottom of the fluid layer is adiabatic. For example, Tritton & Zarraga [22] carried out experimental investigations and found various interesting features; formation of irregular, hexagonal cell with descending flow in the center of a cell, transition of convection cell pattern with respect to internal heat generation, particular interest was the dilatation of convection cells with increasing rate of internal heat generation. Schwiderski & Schwab [23] attempted to confirm the features by an improved experimental setup and they concluded that cell dilatation is not an intrinsic feature of the problem, but instead is induced by non-uniformity of internal heat generation in the experimental apparatus. Carrigan also denied the cell dilatation in his experimental works [24, 25] (But he used copper wires as electrodes in order to realize internal heat generation electrically and then heat generation was clearly non-uniform in the fluid layer.). Sparrow *et al.* [26] first dealt with this problem theoretically as a problem of stability of non-linear temperature gradient. Theoretical study by Roberts [27] carried out a linear stability analysis and an estimation of the preferred modes in the finite amplitude convection. Tveitereid & Palm [28] achieved enhanced analyses of Roberts's work. Thirby [29] performed a numerical simulation and compared his result with the theoretical studies. Their studies, however, could not clarify the features mentioned in the experimental studies. They attributed the cell dilatation to non-uniform heat generation due to imperfections in the experiments; that is, a deviation from uniform heating due to a spatially varying electrical conductivity.

As an enhanced model of the internally heated convection, non-uniform distribution of internal heat generation was treated by Krishnamurti [11] in the context of cloud formation in meteorology. Her experiment, however, uses a chemical reaction to simulate the internal heat generation and cannot be easily modeled for analysis. Yücel & Bayazitoglu [10] also investigated a non-uniform distribution theoretically by using a model in which the heat source increases exponentially from the lower to the upper boundary. Their model, however, was combined with complex boundary conditions which consequently did not allow the fundamental characteristics of heat source distribution to be clarified.

There are the other advanced studies; Internally heated convection in a thermally stratified layer [30], Uniform internal heating with rotation [31, 32], With isothermal boundary condition at the bottom of the fluid layer [33]. Weinstein & Olson [34] performed experimental observation of the convective motion in a mixed heating condition, internal and external heating at the bottom, at extremely high Rayleigh number. They showed a sheet shape descending motion and compared it with their numerical work [35].

### 1.2.2 Rayleigh-Bénard convection in low Prandtl number fluid layer

Rayleigh-Bénard (R-B) convection, natural convection in a shallow fluid layer induced by heating at the bottom of the fluid layer and by cooling at the top, is a classical problem and has a long history of investigations. These investigations are mainly observation of a convective flow pattern formed in the fluid layer with changing parameters, Rayleigh number and Prandtl number. Figure 1.1 shows a very famous phase diagram of R-B convection drown by Krishnamurti [36]. This diagram shows a transition of the flow pattern with respect to Rayleigh number in the wide range of Prandtl number, where symbols represent results of the observation. The flow pattern changes from steady state to turbulence passing through two-dimensional state, three-dimensional state and time dependent state. Boundaries of these states are expressed by the observation points. There is, however, no observation point in an extremely small side of Prandtl number. As working fluid of low Prandtl number is liquid metal and is opaque, we cannot use optical visualization methods in order to observe the flow pattern.

As first investigation of low Prandtl number R-B convection, Rossby [5] reported time-averaged Nusselt number for mercury layer. Recently, Yamanaka *et al.* [37] measured temperature both in a liquid gallium layer and in a copper block, which is a top plate of the fluid layer, by using a thermocouple in order to correlate convective motion and temporal oscillation of heat flux through the fluid layer. A point measurement of temperature in the fluid layer, however, is not sufficient to clarify the flow pattern in comparison with an optical visualization of the flow pattern.

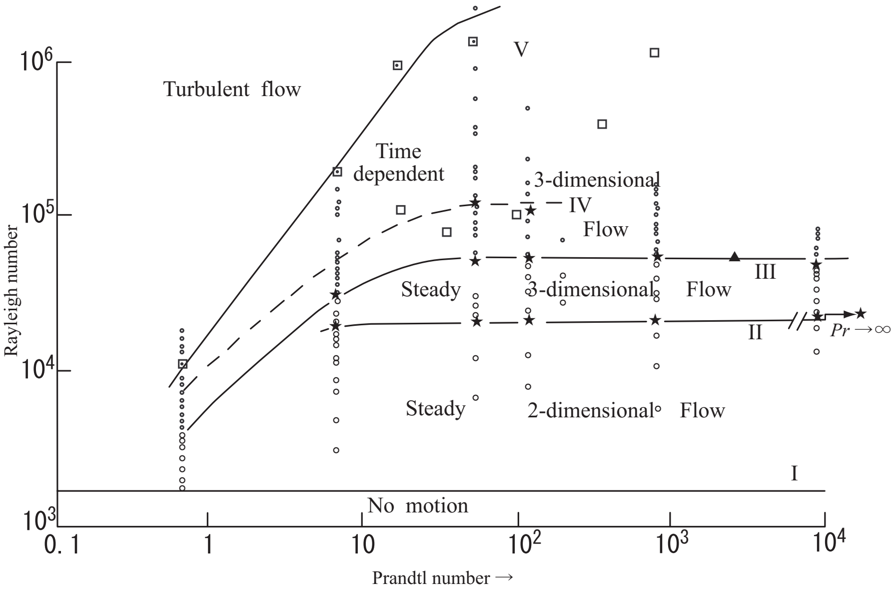

Figure 1.1: The régime diagram for Rayleigh-Bénard convection drawn by Krishnamurti [36].

## 1.3 Objectives

As a first objective, we focus our study on the influence of the heat source distribution on the convection. As we consider that most of the distribution of the internal heating is caused by absorption of radiating wave such as microwave, an exponential distribution in the vertical direction is assumed. Using a linear stability analysis, we investigate a condition at onset of convection for two cases of the distribution. Secondly, we reinvestigate the remaining problems on internally heated convection, e.g. cell dilatation, and study them in greater detail than conventional visual obserbation allowed. Thirdly, we investigate temperature behavior in the internally heated convection in order to support the qualitative investigation and to compare experimental results and theoretically estimated values quantitatively. Finally, we attempt to measure a velocity profile in a convection layer of liquid gallium by UVP, Ultrasonic Velocity Profiler, in order to visualize a flow pattern in low Prandtl number R-B convection.

## 1.4 Résumé

This thesis consists of six chapters including Introduction and four appendixes in which results of supplemental experiments and visualized photographs except for photographs appearing in the main chapters. As each chapter excluding Introduction and Conclusion is individually submitted to various journals, they have Abstract, Introduction and Conclusion part. Contents of the main chapters are summarized as follows.

In Chapter 2, the effects of heat source distribution on natural convection induced by internal heating are studied. Simple models of heat source distribution in which the distribution decayed exponentially from the bottom or top boundary were studied. A linear stability analysis was carried out to calculate the critical Rayleigh number and critical wavenumber for the onset of convection. Our results show the influence of the biased heat source distribution on the onset of convection and the effect of the thickness of the source distribution on the size of the convection cell. As a more realistic problem, the effect of additional bottom wall heating on the internal heat driven convection was studied. We show that the parameter controlling the shape of the temperature profile can be expressed as the ratio of the internal to external Rayleigh numbers (where the internal Rayleigh number is defined for internal heating and the external Rayleigh number is defined for wall heating). We found that an asymmetry in the velocity profile appears when there is a local stable layer with a positive vertical temperature gradient.

In Chapter 3, characteristics of internally heated convection, for instance convection cell dilatation, are reexamined using new experimental methods and an improved experimental apparatus in order to reduce uncertainties as much as possible. The convective motion in the fluid layer was visualized using reflecting particles (Kalliroscope) and independently using a suspension of Thermo-chromic Liquid Crystal; the latter technique also allowed the simultaneous investigation of the temperature field. Cell dilatation was conformed in the improved experimental apparatus and then investigated quantitatively by extracting the pattern wavenumber from Fourier analysis of the images recorded by a digital camera. The pattern wavenumber was found to decrease with increasing Rayleigh number. We compare our results with earlier investigations and discuss the influence of the thermal boundary condition at the bottom of the fluid layer on the variation of the wavenumber. Furthermore, we also discussed a reason of disagreement between theoretical and experimental results.

In Chapter 4, temperature behavior in the internally heated convection is quantitatively investigated. Calibration system was developed in order to convert the visualized photographs of temperature field obtained in Chapter 3 to real temperature field. Calibration curve correlating color information extracted from the photograph to temperature is determined from approximately linear temperature distribution in horizontal fluid layer by hue method. The photographs taken at various internal Rayleigh numbers are converted to temperature field by the obtained curve. A temperature profile in a cell is analyzed by extracting individual cell from a temperature field and we discussed variation of the profile with respect to internal Rayleigh number. Statistical values of the temperature field are compared with theoretically estimated values, and they are well related.

In Chapter 5, we attempt to measure a velocity profile in a convection layer of liquid gallium by UVP, Ultrasonic Velocity Profiler, in order to visualize a flow pattern in low Prandtl number R-B convection. Trial UVP measurements were performed in a fluid flow of liquid gallium driven by magnetic force and in thermal convection of glycerol solution as a test of a low velocity flow measurement. These results confirm a validity of UVP measurement on the convective motion in liquid gallium layer. An experimental apparatus of liquid gallium convection suitable for UVP measurement was developed. We could measure the velocity profile successfully and measure it at different position or at various Rayleigh numbers. These results visualize a convection pattern in the layer and show a temporal behavior of the pattern.

## 1.5 Nomenclature

$c$ : sound speed
$c_p$ : specific heat
$g$ : gravity
$H$ : volumetric heat source
$H_0$ : total power deposited
$k$ : horizontal wavenumber
$k_\mathrm{c}$ : critical wavenumber
$L$ : height of the fluid layer
$p$ : pressure
$Pr$ : Prandtl number
$q$ : distribution function of internal heat source
$R_\mathrm{I}$ : internal Rayleigh number
$R$ : external Rayleigh number
$R_\mathrm{c}$ : critical Rayleigh number
$R_\mathrm{I}^*$ : reduced internal Rayleigh number, $R_\mathrm{I}^* = R_\mathrm{I}/R_\mathrm{c}$
$t$ : time
$T$ : temperature
$\boldsymbol{u}(u, v, w)$ : velocity vector and its components
$\boldsymbol{x}(x, y, z)$ : coordinates of position

$\beta$ : bulk modulus
$\Delta T$ : temperature difference between the top and the bottom boundaries
$\varepsilon$, $\eta$ : characteristic length of heat source distribution
$\Theta$ : $= R_\mathrm{I}/R$
$\lambda$ : thermal conductivity
$\kappa$ : thermal diffusivity
$\mu$ : viscosity
$\nu$ : dynamic viscosity
$\rho$ : density

$*$ : dimension variable (In Chapter 2)
$\hat{}$ : perturbation
$\tilde{}$ : amplitude function of perturbation

## Chapter 2

# Theoretical Study on Effect of Distributed Internal Heat Source

## Abstract

Natural convection induced by internal heating, especially the effects of heat source distribution, is studied. Simple models of heat source distribution in which the distribution decayed exponentially from the bottom or top boundary were studied. A linear stability analysis was carried out to calculate the critical Rayleigh number and critical wavenumber for the onset of convection. Our results show the influence of the biased heat source distribution on the onset of convection and the effect of the thickness of the source distribution on the size of the convection cell. We estimated the total amount of heat generation necessary to cause convection for each distribution, and compared these values with these for uniform internal heating. Furthermore, we found that the asymmetry in the convective motion is induced by a "quasi-stable layer" formed in the bottom part of the fluid layer.

As a more realistic problem, we studied the effect of additional bottom wall heating on the internal heat driven convection. We show that the parameter controlling the shape of the temperature profile can be expressed as the ratio of the internal to external Rayleigh numbers (where the internal Rayleigh number is defined for internal heating and the external Rayleigh number is defined for wall heating). We found that an asymmetry in the velocity profile appears when there is a local stable layer with a positive vertical temperature gradient. Furthermore, heat source distribution is concentrated near the top boundary thickens this local stable layer and this enhances the asymmetry of the convective motion. The thicker stable layer reduces the effective height of the fluid layer which in turn causes the critical Rayleigh number and critical wavenumber to vary drastically.

## 2.1 Introduction

In Chapter 2, as the first objective, the influences of the heat source distribution on the convection are investigated by using a simple model of the distribution. The governing equations for perturbations in the internally heated convection are derived and the fundamental characteristics of the convection with uniform internal heating are explained in Section 2. In order to determine the critical Rayleigh number and the critical wavenumber, a numerical method is derived in Section 3. Since most of the distribution of the internal heating is caused by absorption of radiating wave, a simple model of heat source distribution, which varies exponentially to the vertical direction, is assumed. Both cases where heat source concentrates near the bottom or the top boundary are considered in Section 4. The models of heat source distribution have a characteristic length which expresses an extent of the concentration. Rayleigh number in which the specific scale of the distribution appears explicitly is derived for each distribution. Stability analysis is carried out the critical Rayleigh number and the critical wavenumber for each values of the specific scale.

The combination of internal heating and wall heating from the bottom boundary is considered, and as the second objective influence of the wall heating on the internally heated convection is revealed in Section 5. It is shown that the parameter controlling the shape of the temperature profile is expressed as the ratio of Rayleigh number related to internal heating (internal Rayleigh number) to that related to wall heating (external Rayleigh number) by arranging the equation shown in equation (24) in Sparrow *et al.* [26]. Furthermore this ratio is extended to the distributed internal heating in the later section.

## 2.2 Basic equations with uniform internal heating

A horizontal fluid layer unbound for the horizontal directions has steady internal heat generation $H(z^*)$ as shown in Figure 2.1. Let a top ($z^* = L$) and a bottom ($z^* = 0$) boundary be isothermal with the temperature $T^* = T_1$ and adiabatic, $\mathrm{grad} T^* = 0$, respectively. Following assumptions are made: a temperature field is dominated by heat conduction and by internal heating in stationary state, and a pressure field $p^*(\boldsymbol{x}^*)$ is in hydrostatic equilibrium. The fluid layer obeys Boussinesq approximation, and density $\rho^*$ is a linear function of temperature independently of pressure.

Basic equations in the fluid field (velocity $\boldsymbol{u}^*$, $p^*$, $T^*$ and $\rho^*$) are the continuity equation, the equation of motion, the energy equation and the equation of state, as follows.

$$\nabla^* \cdot \boldsymbol{u}^* = 0, \tag{2.1}$$

$$\rho_1 \frac{D\boldsymbol{u}^*}{Dt^*} = -\nabla^* p^* - \rho^* g \boldsymbol{e}_z + \mu \varDelta^* \boldsymbol{u}^*, \quad \boldsymbol{e}_z = (0, 0, 1), \tag{2.2}$$

$$\rho_1 c_p \frac{DT^*}{Dt^*} = \lambda \varDelta^* T^* + H(z^*), \tag{2.3}$$

$$\rho^* = \rho_1 [1 - \beta (T^* - T_1)], \tag{2.4}$$

where Laplacian $\Delta^* = \partial^2/\partial x^{*2} + \partial^2/\partial y^{*2} + \partial^2/\partial z^{*2}$. $\lambda$, $\mu$, $\beta$, $H$ and $c_p$ are thermal conductivity, viscosity, bulk modulus ($\beta = (dV/dT^*)_{T_1}/V$, $V$ is volume), amount of heat generation per unit time and per unit volume and specific heat respectively. In addition, $\rho_1 = \rho(T_1)$. It is assumed that temperature dependence of these physical properties can be neglected.

At first uniform internal heat generation $H(z^*) = H_0$ is considered. In a stationary state ($\bar{\boldsymbol{u}} = 0$), solutions of equations (2.2) to (2.4) are

$$\bar{T}^* - T_1 = \frac{H_0}{2\lambda}(L^2 - z^{*2}), \tag{2.5}$$

$$\bar{\rho}^* = \rho_1 \left[ 1 - \beta \frac{H_0}{2\lambda}(L^2 - z^{*2}) \right], \tag{2.6}$$

$$\bar{p}^* = \rho_1 g z^* \left[ 1 - \beta \frac{H_0}{2\lambda} \left( L^2 - \frac{1}{3} z^{*2} \right) \right] + \text{const.} \tag{2.7}$$

By defining perturbations as $\hat{\boldsymbol{u}}^*$, $\hat{T}^*$, $\hat{\rho}^*$ and $\hat{p}^*$, physical variables can be expressed as

$$\boldsymbol{u}^* = \hat{\boldsymbol{u}}^*, \quad T^* = \bar{T}^* + \hat{T}^*, \quad \rho^* = \bar{\rho}^* + \hat{\rho}^*, \quad p^* = \bar{p}^* + \hat{p}^*.$$

Equations (2.1) to (2.4) are transformed by substituting these definitions and equations (2.5) to (2.6), and are linearized. We define dimensionless physical variables as

$$\boldsymbol{x} = \frac{\boldsymbol{x}^*}{L}, \quad t = \frac{\kappa_1}{L^2} t^*, \quad p = \frac{p^* L^2}{\rho_1 \kappa_1^2}, \quad \boldsymbol{u} = \frac{L}{\kappa_1} \boldsymbol{u}^*, \tag{2.8}$$

where thermal diffusivity $\kappa_1 = \lambda/(\rho_1 c_p)$. By using temperature difference between the top and the bottom boundary, $\Delta T \equiv T_0 - T_1 = H_0 L^2/(2\lambda)$, dimensionless temperature is defined as

$$T = \frac{1}{\Delta T} T^*. \tag{2.9}$$

Finally linearized equations become

$$\nabla \cdot \hat{\boldsymbol{u}} = 0, \tag{2.10}$$

$$\frac{\partial \hat{\boldsymbol{u}}}{\partial t} = -\nabla \hat{p} + R_{\mathrm{I}} Pr \hat{T} \boldsymbol{e}_z + Pr \mathit{\Delta} \hat{\boldsymbol{u}}, \quad \boldsymbol{e}_z = (0, 0, 1), \tag{2.11}$$

$$\frac{\partial \hat{T}}{\partial t} + \frac{d\bar{T}}{dz} \hat{w} = \mathit{\Delta} \hat{T}, \tag{2.12}$$

where

$$\left.\begin{aligned} Pr &= \frac{\nu_1}{\kappa_1} \left( = \frac{\mu/\rho_1}{\kappa_1} \right) &&: \ \text{Prandtl number,} \\ R_{\mathrm{I}} &= \frac{g\beta H_0 L^5}{2\lambda \nu_1 \kappa_1} &&: \ \text{Rayleigh number.} \end{aligned}\right\} \tag{2.13}$$

Being distinct from usual Rayleigh number related with wall heating (external Rayleigh number), this kind of Rayleigh number is called as internal Rayleigh number. After the convection occurring, $H_0 L^2/(2\lambda)$ in the definition of internal Rayleigh number does not indicate a temperature difference between both boundaries because the temperature difference in the internally heated convection depends on convection pattern not only amount of heat generation.

Perturbations are described as

$$\begin{bmatrix} \hat{\boldsymbol{u}}(\boldsymbol{x}, t) \\ \hat{T}(\boldsymbol{x}, t) \\ \hat{p}(\boldsymbol{x}, t) \end{bmatrix} = \begin{bmatrix} \tilde{\boldsymbol{u}}(z) \\ \tilde{T}(z) \\ \tilde{p}(z) \end{bmatrix} \exp[i(\alpha_x x + \alpha_y y) + \sigma t]. \tag{2.14}$$

By substituting this formula into equations (2.10) to (2.12), perturbation equations are derived as

$$\left( \frac{d^2}{dz^2} - k^2 - \frac{\sigma}{Pr} \right) \left( \frac{d^2}{dz^2} - k^2 \right) \tilde{w} = R_{\mathrm{I}} k^2 \tilde{T}, \tag{2.15}$$

$$\left( \frac{d^2}{dz^2} - k^2 - \sigma \right) \tilde{T} = \frac{d\bar{T}}{dz} \tilde{w}, \tag{2.16}$$

where $k$ is horizontal wavenumber, $k = \sqrt{\alpha_x^2 + \alpha_y^2}$.

Boundary conditions for perturbation velocity are derived from rigid boundary condition as

$$\tilde{w} = \frac{d\tilde{w}}{dz} = 0 \ \text{ at } z = 0, 1. \tag{2.17}$$

Corresponding to adiabatic boundary ($z = 0$) and isothermal boundary ($z = 1$), boundary conditions for temperature are

$$\frac{d\tilde{T}}{dz} = 0 \text{ at } z = 0, \quad \tilde{T} = 0 \text{ at } z = 1. \tag{2.18}$$

Linear stability analysis is made on perturbation equations (2.15) and (2.16) with boundary conditions (2.17) and (2.18). Critical values, critical Rayleigh number $R_{\rm c}$ and critical wavenumber $k_{\rm c}$, for uniform internal heating calculated by Roberts [27] are $R_{\rm c} = 1386.14$ and $k_{\rm c} = 2.629$[1]. Comparing with Rayleigh-Bénard convection ($R_{\rm c} = 1707.76$ and $k_{\rm c} = 3.117$, Reid & Harris [38]), these results conclude that convection occurs more easily and convection cell becomes larger in the internally heated convection. Figure 2.2 shows neutral stability curves for internally heated convection and for Rayleigh-Bénard convection, which were recalculated in this study. The curve of internally heated convection is wider than in Rayleigh-Bénard convection especially for the small side, this difference may suggest that convection cell in the internally heated convection have various sizes.

## 2.3 Numerical method

The same method as in Sparrow *et al.* [26] and in Kulacki & Goldstein [39] was used to obtain eigenvalues. Namely, solution of governing equations of perturbation was expressed by using power series as follows:

$$\tilde{w} = \sum_{i=0}^{5} C_i f^{(i)}(z), \quad f^{(i)} = \sum_{n=0}^{\infty} b_n^{(i)} (z-a)^n, \tag{2.19}$$

then coefficients $b_n^{(i)}$ $(n = 0, 1, 2, \cdots, \infty)$ for each value of $a$ are determined as follows.

$$\begin{aligned}
b_0^{(i)} &= f(a) = \sum b_n^{(i)} a^n, \\
b_1^{(i)} &= \left.\frac{df}{dz}\right|_{z=a} = \sum n b_n^{(i)} a^{n-1}, \\
b_2^{(i)} &= \frac{1}{2!} \sum n(n-1) b_n a^{n-2}, \\
b_3^{(i)} &= \frac{1}{3!} \sum n(n-1)(n-2) b_n^{(i)} a^{n-3}, \\
b_4^{(i)} &= \frac{1}{4!} \sum n(n-1)(n-2)(n-3) b_n^{(i)} a^{n-4}, \\
b_5^{(i)} &= \frac{1}{5!} \sum n(n-1)(n-2)(n-3)(n-4) b_n^{(i)} a^{n-5}.
\end{aligned}$$

---

[1] Roberts used the definition of internal Rayleigh number as $R_{\rm I} = (g\beta H L^5)/(\lambda\nu\kappa)$, and it is twice in our definition. Thus, $R_{\rm c}$ in his paper is 2772.28.

Coefficients for $n \geq 6$ are determined from a recursion relationship. In the case with uniform internal heat generation it becomes

$$b_n = \frac{1}{n!}\Big\{3k^2(n-2)!b_{n-2} - 3k^4(n-4)!b_{n-4} \\ - [2R_{\mathrm{I}}k^2 b_{n-7} + (2R_{\mathrm{I}}k^2 a - k^6)b_{n-6}](n-6)!\Big\} \qquad (n \geq 6).$$

Only in cases in which a point is near the base point $z = a$, power series expansion can determine a value at this position with high accuracy. But if a point is far the base point, error may increase. In order to reduce such error, the range $z = [0, 1]$ is divided into $N$ parts and calculate at each part. An appropriateness of this division number $N$ is verified by comparison with exact solution of critical Rayleigh number $R$ calculated by Reid and Harris [38] in Rayleigh-Bénard problem. Table 2.1 shows an exact solution and approximate values for various number of $N$, where numbers in bold style show critical Rayleigh number $R_{\mathrm{c}}$. In approximate values with $N = 2$, $R_{\mathrm{c}}$ is the same with an exact solusion, but for higher wavenumber these values are slightly different from exact values. The values with $N = 10$ completely corresponds with an exact solusion over all values of $k$. Therefore, $N = 10$ was choosen as the division number in the calculation.

Table 2.1: Comparison between exact and approximate values for each divisonal number $N$, where the exact solution was calculated by Reid & Harris [38].

| $k$ | $R$ | | | |
|---|---|---|---|---|
| | Exact | $N = 1$ | $N = 2$ | $N = 10$ |
| 0.5 | 21009.76 | 21008.31 | 21009.76 | 21009.76 |
| 1.0 | 5854.48 | 5853.99 | 5854.48 | 5854.48 |
| 1.5 | 3090.17 | 3089.84 | 3090.17 | 3090.17 |
| 2.0 | 2177.44 | 2177.06 | 2177.44 | 2177.44 |
| 2.5 | 1822.35 | 1822.65 | 1822.35 | 1822.35 |
| 3.0 | 1711.33 | 1714.31 | 1711.33 | 1711.33 |
| **3.089** | - | **1711.89** | - | - |
| **3.119** | **1707.68** | - | **1707.68** | **1707.68** |
| 3.5 | 1742.33 | 1756.69 | 1742.33 | 1742.33 |
| 4.0 | 1879.29 | 1935.83 | 1879.29 | 1879.29 |
| 4.5 | 2111.43 | 2337.69 | 2111.43 | 2111.43 |
| 5.0 | 2439.54 | 2201.82 | 2439.54 | 2439.54 |
| 5.5 | 2871.27 | 2095.06 | 2871.27 | 2871.27 |
| 6.0 | 3417.84 | 2223.29 | 3418.58 | 3417.84 |
| 6.5 | 4094.40 | 2292.04 | 4096.26 | 4094.40 |
| 7.0 | 4918.17 | 3030.45 | 4921.65 | 4918.17 |
| 7.5 | 5908.03 | 4451.24 | 5913.79 | 5908.03 |
| 8.0 | 7084.97 | 5900.70 | 7097.37 | 7084.97 |

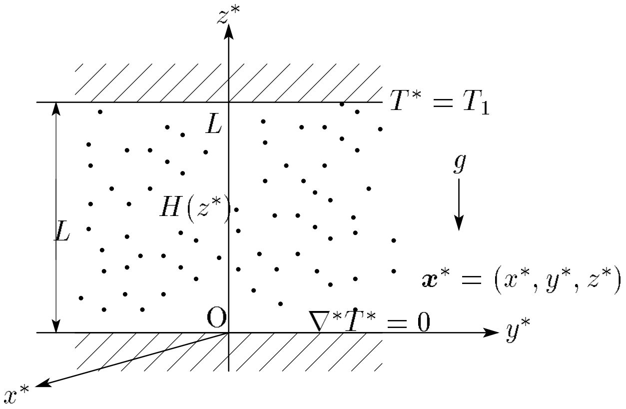

Figure 2.1: Coordinates and configuration; thermal boundary conditions at the top and bottom are isothermal and adiabatic respectively, internal heat source $H$ distributes for the vertical direction.

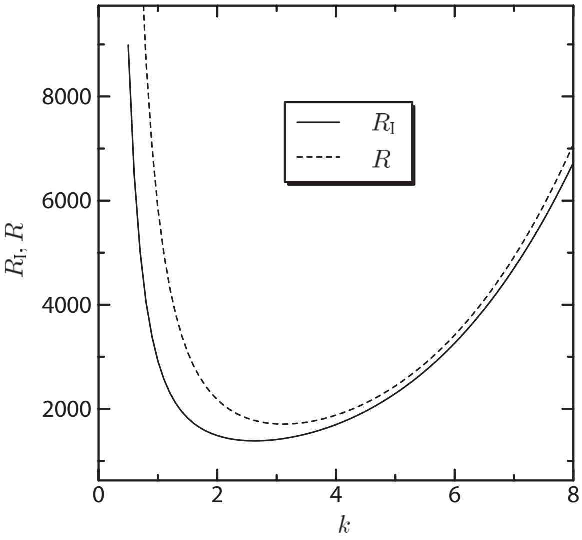

Figure 2.2: Neutral stability curves for internally heated convection(solid line) and for Rayleigh-Bénard convection (broken line)

## 2.4 Distributed heat source

### 2.4.1 General treatment of heat source distribution

Distributed internal heat source is expressed as follows.

$$H(z, \varepsilon) = \frac{H_0}{\varepsilon} q(z, \varepsilon), \tag{2.20}$$

where, $q(z, \varepsilon)$ is a normalized function which expresses a form of the heat source distribution, and $\varepsilon$ is a characteristic length related to the form.

By this definition,

$$\int_0^1 H(z, \varepsilon) dz = H_0.$$

$H_0$ is a total power induced by internal heating, and it does not depend on a distribution form. In the case with uniform internal heating, heat source distribution can be expressed by this formula with $q(z, \varepsilon)/\varepsilon = 1$.

### 2.4.2 Concentration of heat source on the bottom boundary

Heat source distribution, which concentrates near the bottom boundary, is considered. A model of heat source distribution, which has the maximum at the bottom and decreases to the upward direction exponentially as follows, is used.

$$H(z, \varepsilon) = \frac{H_0}{Q(\varepsilon)} \exp\left(-\frac{z}{\varepsilon}\right), \tag{2.21}$$

$$Q(\varepsilon) = \int_0^1 \exp\left(-\frac{z}{\varepsilon}\right) dz = \varepsilon \left[1 - \exp\left(-\frac{1}{\varepsilon}\right)\right].$$

Heat source distributions for various values of $\varepsilon$ are shown in Figure 2.3. As is seen in this figure, heat source concentrates more near the bottom with decrease of $\varepsilon$. It becomes close to uniform distribution by increasing $\varepsilon$. $H$ becomes $H_0$ when $\varepsilon$ approaches the limit of $\infty$. For this model of heat source distribution, the temperature profile in heat conduction is derived by integrating the equation of heat conduction (2.3), which includes the distribution (2.21), with boundary conditions (2.18) as follows.

$$\bar{T}^* - T_1 = \frac{H_0 L^2}{\lambda} \frac{\varepsilon^2}{Q(\varepsilon)} \left[\exp\left(-\frac{1}{\varepsilon}\right) - \exp\left(-\frac{z}{\varepsilon}\right) + \frac{1-z}{\varepsilon}\right]. \tag{2.22}$$

A temperature difference between the top and the bottom, $\Delta T$, is

$$\Delta T = \bar{T}^*(z=0) - T_1 = \frac{H_0 L^2}{\lambda} \frac{\varepsilon^2}{Q(\varepsilon)} \left[\exp\left(-\frac{1}{\varepsilon}\right) + \frac{1-\varepsilon}{\varepsilon}\right]. \tag{2.23}$$

Temperature profile for the vertical direction expressed by equation (2.22) is shown in Figure 2.3(b). In this figure a broken line shows a profile in the case with uniform heating; namely $H = H_0$. $\bar{T}^*$ approaches this curve asymptotically with respect to $\varepsilon$.

Perturbation equation on temperature for such internal heat distribution is derived as

$$\left(\frac{d^2}{dz^2} - k^2 - \sigma\right)\tilde{T} = -\frac{1}{C(\varepsilon)}\left[1 - \exp\left(-\frac{z}{\varepsilon}\right)\right]\tilde{w}, \tag{2.24}$$

where

$$C(\varepsilon) = \varepsilon\left[\exp\left(-\frac{1}{\varepsilon}\right) + \frac{1}{\varepsilon} - 1\right].$$

For a perturbation equation (2.15), the internal Rayleigh number is defined as

$$R_{\mathrm{I}} = \frac{g\beta H_0 L^5}{\lambda\nu_1\kappa_1}\frac{\varepsilon^2}{Q(\varepsilon)}\left[\exp\left(-\frac{1}{\varepsilon}\right) + \frac{1}{\varepsilon} - 1\right]. \tag{2.25}$$

$R_{\mathrm{I}}$ has a characteristic length of heat source distribution $\varepsilon$ in addition to the height of the fluid layer $L$.

In a state of neutral stability ($\sigma = 0$) an equation for $\tilde{w}$ is derived from equations (2.15) and (2.24) as

$$\left(\frac{d^2}{dz^2} - k^2\right)^3\tilde{w} = -\frac{R_{\mathrm{I}}k^2}{C(\varepsilon)}\left[1 - \exp\left(-\frac{z}{\varepsilon}\right)\right]\tilde{w}. \tag{2.26}$$

In order to obtain eigenvalues the same method used in Sparrow *et al.* [26] was used. A main part of this method was already explained in the last section. A characteristic equation is derived using power series solution (2.19), perturbation equation (2.26) and boundary conditions (2.17) and (2.18). Here, a heat source distribution function $\exp(-z/\varepsilon)$ can be expanded by Taylor series around $z = a$ as

$$\exp\left(-\frac{z}{\varepsilon}\right) = \exp\left(-\frac{a}{\varepsilon}\right)\sum_{m=0}^{\infty}\frac{(-1)^m}{m!}\left(\frac{z-a}{\varepsilon}\right)^m.$$

By assuming that the power series (19) is a solution of equation (2.26),

$$\sum_{n=0}^{\infty}\Bigg\{\frac{n!}{(n-6)!}b_n(z-a)^{n-6} - 3k^2\frac{n!}{(n-4)!}b_n(z-a)^{n-4} + 3k^4\frac{n!}{(n-2)!}b_n(z-a)^{n-2}$$
$$+\left[-\frac{R_{\mathrm{I}}k^2}{C(\varepsilon)}\exp\left(-\frac{a}{\varepsilon}\right)\sum_{m=0}^{\infty}\frac{(-1)^m}{m!\varepsilon^m}(z-a)^{m+n} + \left(\frac{R_{\mathrm{I}}k^2}{C(\varepsilon)} - k^6\right)(z-a)^n\right]b_n\Bigg\} = 0.$$

For this equation to hold for all $z$, all of the series coefficients $b_n$ have to be zero. And then following recursion relation can be derived.

$$\begin{aligned} b_n =& \frac{1}{n!}\Bigg\{ 3k^2(n-2)!b_{n-2} - 3k^4(n-4)!b_{n-4} \\ &+ \left[ \left( k^6 - \frac{Ra_{\mathrm{I}}k^2}{C(\varepsilon)} \right) b_{n-6} + \frac{R_{\mathrm{I}}k^2}{C(\varepsilon)} \exp\left(-\frac{a}{\varepsilon}\right) \sum_{m=0}^{\infty} \frac{(-1)^m}{m!\varepsilon^m} b_{n-6-m} \right] (n-6)! \Bigg\} = 0. \end{aligned}$$

In the actual calculation, cutoff number for $n$ and $m$ were 20 and 6 respectively, and the region $z = [0, 1]$ was divided into 10 intervals.

Critical values, $R_{\mathrm{c}}$ and $k_{\mathrm{c}}$, for several values of $\varepsilon$ were obtained. Variations in these values with respect to $\varepsilon$ are shown in Figure 2.4. In these figures, broken lines show critical values for uniform internal heating calculated by Roberts [27]. $R_{\mathrm{c}}$ and $k_{\mathrm{c}}$ increase with $\varepsilon$ and approach asymptotically to these lines; $H = H_0$. The largest difference of $k_{\mathrm{c}}$ from uniform heating is only 2% for $\varepsilon$ investigated here, so that this distribution of heat source has little influence on the size of convection cell. On the other hand, $R_{\mathrm{c}}$ for $\varepsilon$ =0.2 is 13% smaller than that for uniform heating. Therefore the concentration of heat source near the bottom would lower the stability of the convection.

Until now, critical Rayleigh number for each distribution of heat source with $\varepsilon$ was discussed. On the other hand, discussing total power necessary to induce convection is also important because we usually estimate intensity of internal heating by using the total power in experiment. $R_{\mathrm{c}}$ is divided by a part that relates to the form of heat source distribution in the definition (2.24) as

$$D(\varepsilon) \equiv \frac{\varepsilon^2}{Q(\varepsilon)} \left[ \exp\left(-\frac{1}{\varepsilon}\right) + \frac{1}{\varepsilon} - 1 \right].$$

Because $R_{\mathrm{c}}/D(\varepsilon) \sim H_0$, comparison of total power in each case is identical to estimating $R_{\mathrm{c}}/D(\varepsilon)$. Figure 2.5 shows the variation of total power with respect to $\varepsilon$. In $\varepsilon = 2$, convection occurs at the heat power smaller than that in uniform heating by 10% in spite of the heat source distribution in $\varepsilon = 2$ being nearly uniform. This result suggests that such slight concentration of heat source to the bottom can promote convection occurring significantly without increasing total heat amount as an advantage, and also slight deviation of heat source from uniform heating induces large difference of the critical Rayleigh number even the same amount of heat is added to the fluid layer. When we experiment on convection with internal heating, heat source distribution may slightly deviate from uniform. Therefore we have to estimate deviation of heat source from uniform in experiment before discussing about experimental results.

### 2.4.3 Concentration of heat source on the top boundary

A heat source distribution expressed as

$$H(z,\eta) = \frac{H_0}{Q(\eta)} \exp\left(\frac{z-1}{\eta}\right) \tag{2.27}$$

is considered, where

$$Q(\eta) = \int_0^1 \exp\left(\frac{z-1}{\eta}\right) dz = \eta\left[1 - \exp\left(-\frac{1}{\eta}\right)\right].$$

It increases to the vertical direction exponentially and becomes the maximum at the top boundary. Its variation is reverse to that in the previous section. $\eta$ is a characteristic length of heat source distribution, and as shown in Figure 2.6(a), heat concentrates on the top boundary with decreasing $\eta$.

From equation of heat conduction, a temperature profile for this heat source distribution is obtained as

$$\bar{T}^* - T_1 = \frac{H_0 L^2}{\lambda} \frac{\eta^2}{Q(\eta)} \left[1 - \exp\left(\frac{z-1}{\eta}\right) + \frac{z-1}{\eta} \exp\left(-\frac{1}{\eta}\right)\right]. \tag{2.28}$$

Temperature difference $\Delta T$ is

$$\Delta T = \bar{T}^*(z=0) - T_1 = \frac{H_0 L^2}{\lambda} \frac{\eta^2}{Q(\eta)} \left[1 - \left(1 + \frac{1}{\eta}\right) \exp\left(-\frac{1}{\eta}\right)\right]. \tag{2.29}$$

Figure 2.6(b) shows temperature profile expressed as equation (2.28). For small $\eta$, temperature variation exists only near the top and slightest near the bottom. For instance, at $\eta = 0.1$, temperature is nearly constant in the lower half of the fluid layer and decreasing amount of temperature at $z = 0.5$ is only 1% or less of the maximum.

From equation (2.16), (2.28) and (2.29), the perturbation equation is derived as follows.

$$\left(\frac{d^2}{dz^2} - k^2 - \sigma\right) \tilde{T} = -\frac{1}{E(\eta)} \left[\exp\left(\frac{z-1}{\eta}\right) - \exp\left(-\frac{1}{\eta}\right)\right] \tilde{w}, \tag{2.30}$$

where

$$E(\eta) = \eta\left[1 - \left(1 + \frac{1}{\eta}\right) \exp\left(-\frac{1}{\eta}\right)\right].$$

On the other hand, from equation (2.15),

$$\left(\frac{d^2}{dz^2}-k^2-\frac{\sigma}{Pr}\right)\left(\frac{d^2}{dz^2}-k^2\right)\tilde{w}=R_{\mathrm{I}}k^2\tilde{T},$$

$$R_{\mathrm{I}}=\frac{g\beta H_0L^5}{\lambda\nu_1\kappa_1}\frac{\eta^2}{Q(\eta)}\left[1-\left(1+\frac{1}{\eta}\right)\exp\left(-\frac{1}{\eta}\right)\right]. \tag{2.31}$$

The equation for perturbation velocity $\tilde{w}$ in the state of neutral stability ($\sigma=0$) is

$$\left(\frac{d^2}{dz^2}-k^2\right)^3\tilde{w}=-\frac{R_{\mathrm{I}}k^2}{E(\eta)}\left[\exp\left(\frac{z-1}{\eta}\right)-\exp\left(-\frac{1}{\eta}\right)\right]\tilde{w}. \tag{2.32}$$

Figure 2.7 shows variations of $R_{\mathrm{c}}$ and $k_{\mathrm{c}}$ with respect to $\eta$. Both variations are gradual for $\eta\geq 0.5$, but sharp below $\eta=0.5$. At $\eta=0.1$, for instance, $R_{\mathrm{c}}$ becomes 4.5 times as large as that for $H=H_0$. For a small value of $\eta$, the temperature is nearly constant over a wide range of the vertical direction as seen in Figure 2.6(b). Temperature gradient is gradual, but the fluid layer is certainly unstable just only gradual temperature gradient. Such a layer, however, clearly reduces instability of the fluid layer as given in Figure 2.7. Therefore, we name such a layer as a quasi-stable layer. Large deformation of a temperature profile from uniform heating with formation of the quasi-stable layer especially increases a dimensionless critical wavenumber $k_{\mathrm{c}}$. The increase of $k_{\mathrm{c}}$ from uniform heating is approximately 14% at $\eta=0.1$, and an extreme concentration of heat source on the bottom boundary may induce large influence on the size of the convection cell.

Eigenfunction $\tilde{w}$ for uniform internal heating is almost symmetrical with respect to the half line of the fluid layer. For a heat source distribution in which heat source concentrates on the top boundary, $\tilde{w}$ is not symmetric and the center of the convection cells becomes slightly higher than the half line. For instance, this distance is approximate 3% of the height of the fluid layer for the distributed internal heat source with $\eta=0.1$. Profile of $\tilde{w}$ in the internally heated convection is originally asymmetric because temperature profile in the conduction state is asymmetric being different from the standard Rayleigh-Bénard convection. It is, however, not apparent in the uniform internal heating. Concentration of heat source on the top boundary enhances such asymmetric property of $\tilde{w}$. There is no clear critical value of $\eta$ for asymmetry to be induced and thickness of the quasi-stable layer cannot be determined because temperature decreases to the vertical direction monotonically even for small value of $\eta$.

Using $R_\mathrm{c}/D(\eta)$ can estimate total power necessary to induce convection, where

$$D(\eta) = \frac{\eta^2}{Q(\eta)}\left[1 - \left(1 + \frac{1}{\eta}\right)\exp\left(-\frac{1}{\eta}\right)\right].$$

Figure 2.8 shows that total power necessary to induce convection by heat source distribution with $\eta = 0.1$ is 20 times as large as that in uniform heating. Even at $\eta = 1$, the total power becomes 1.3 times.

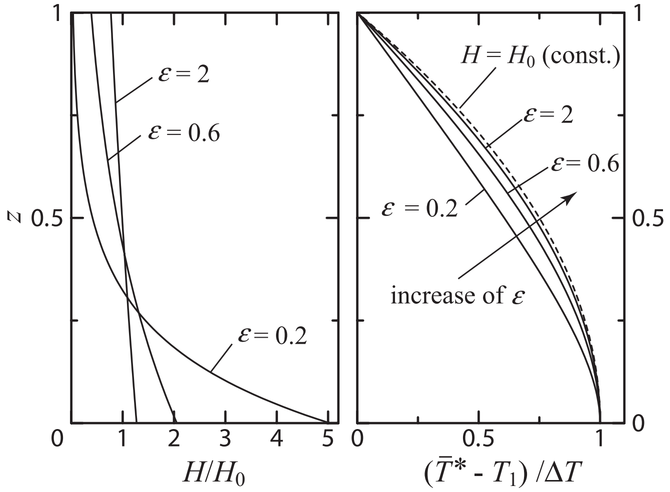

(a) Internal heat source (b) Temperature

Figure 2.3: (a) Heat source distribution and (b) temperature profile at conduction state versus $\varepsilon$, broken line shows temperature profile for uniform internal heating, $H = H_0$.

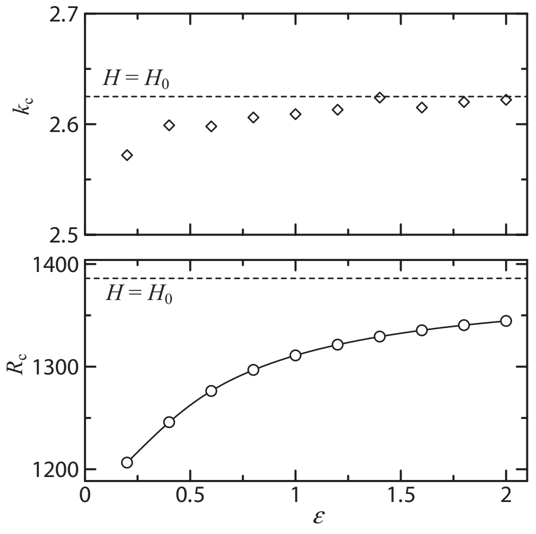

Figure 2.4: Variation of critical Rayleigh number $R_c$ (below) and critical wavenumber $k_c$ (above) versus $\varepsilon$, broken lines express $k_c$ and $R_c$ for uniform internal heating.

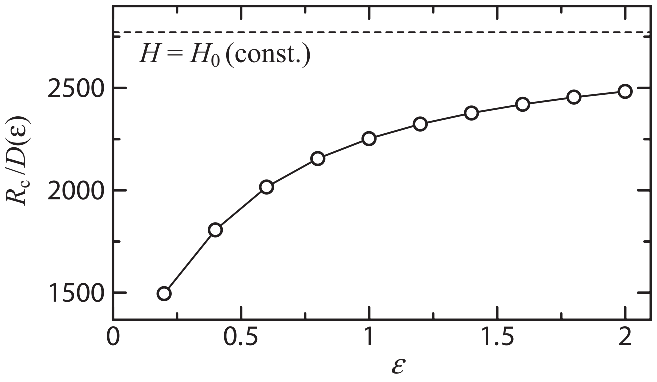

Figure 2.5: Variation of total power necessary to induce convection with respect to $\varepsilon$, broken line shows one for uniform internal heating.

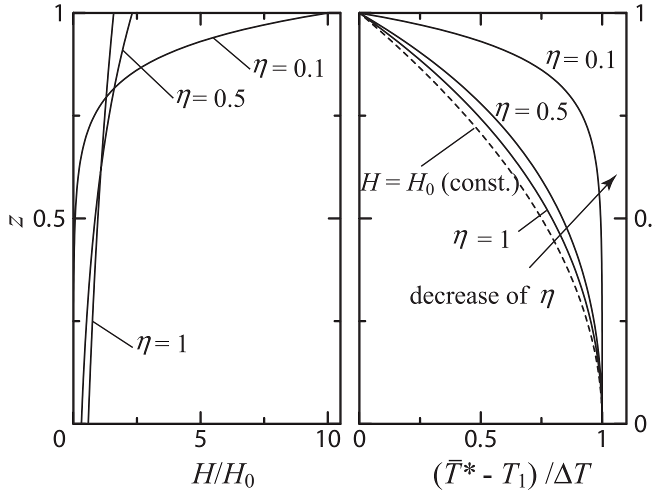

(a) Internal heat source

(b) Temperature

Figure 2.6: (a) Heat source distribution and (b) temperature profile at conduction state versus $\eta$, broken line shows temperature profile for uniform internal heating, $H = H_0$.

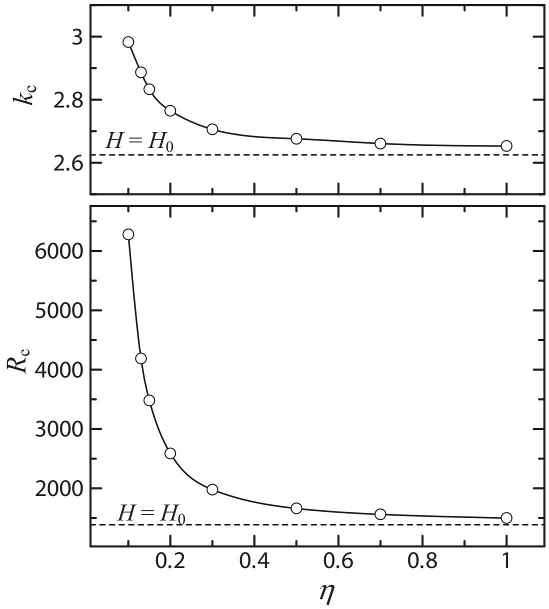

Figure 2.7: Variation of critical Rayleigh number $R_c$ (below) and critical wavenumber $k_c$ (above) versus $\eta$, broken lines express $k_c$ and $R_c$ for uniform internal heating.

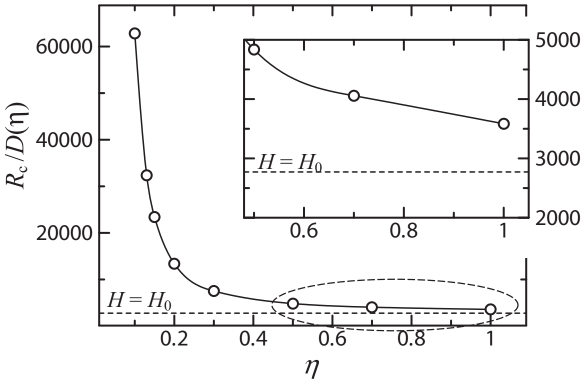

Figure 2.8: Variation of total power necessary to induce convection with respect to $\eta$, broken line shows one for uniform internal heating. Inside figure shows close-up of part enclosed by broken curve.

## 2.5 Combination with wall heating (mixed convection)

Thus far, heat flux through the bottom boundary was neglected in order to focus on only effect of distribution of internal heat source with the bottom boundary being adiabatic. In this section the case with heating from below with $T^* = T_2$, $T_2 > T_1$ is consider as more realistic problem. As shown in Figure 2.9, the configuration without thermal boundary condition at the bottom is the same in the last section. There are two kinds of heat source, namely internal heat source and external heat source as wall heating in this problem, and problems for each heat source have been studied as internally heated convection and Rayleigh-Bénard convection. This problem is a mixture of both problems and is might be called "**mixed convection**"[2].

### 2.5.1 Temperature profile with Internal and External Rayleigh number

We consider the combination of the uniform internal heating and the wall heating at the bottom. Adding of wall heating to the internally heated convection changes a form of a temperature profile for the vertical direction. Temperature in the conduction state $\bar{T}^*$ is derived as

$$\bar{T} = \frac{\bar{T}^* - T_1}{T_2 - T_1} = -\Theta z^2 + (\Theta - 1)z + 1, \tag{2.33}$$

$$\text{where} \quad \Theta = \frac{H_0 L^2}{2\lambda(T_2 - T_1)}.$$

$\Theta$ is a dimensionless parameter, which determines a form of a temperature profile. Figure 2.10 shows examples of temperature profile for two $\Theta$ values. In a case with $\Theta \leq 1$, as a curve with a broken line shown in this figure, the temperature profile is similar to that with an adiabatic boundary. Namely, temperature has the maximum on the bottom and decreases to the vertical direction monotonically. On contrary, in case with $\Theta > 1$, as a curve with solid line, the profile has the maximum at $h_\mathrm{s}$ which is higher than the bottom and the maximum temperature $T_\mathrm{M}$ is greater than the bottom temperature $T_2$. Therefore in this case, a local stable layer is formed in range of $0 \leq z \leq h_\mathrm{s}$. It is easy to derive from equation (2.33) that $h_\mathrm{s} = (\Theta - 1)/2\Theta$. $h_\mathrm{s}$ increases with increase of $\Theta$, and $h_\mathrm{s}$ becomes $1/2$ at $\Theta \to \infty$.

---

[2] We perform experimental observation of mixed convection in Appendix 1.

The definition of $\Theta$ is represented as

$$\Theta = \frac{H_0 L^2}{2\lambda} \Big/ (T_2 - T_1), \\ = \frac{R_{\mathrm{I}}}{R}. \tag{2.34}$$

It is a ratio of the internal Rayleigh number to the external one. For $\Theta \leq 1$, wall heating is dominant and the overall fluid layer is unstable. On the other hand, $\Theta > 1$, internal heating is dominant and a locally stable layer is formed.

Stability analysis for this problem was already made by Sparrow *et al.* [26]. Their interests were, however, only effects of nonlinear temperature profile on convection and they did not discuss about $\Theta$. Critical "external" Rayleigh number and critical wavenumber for each $\Theta$ changes by a selection of a characteristic temperature and a characteristic length. For instance, at $\Theta = 5$, $R_{\mathrm{c}}$ calculated by using temperature difference between both boundaries and height of the fluid layer is 1463. By using the maximum temperature in the fluid layer and height of an unstable layer $L(1 - h_{\mathrm{s}})$, it becomes 569 [26].

At $\Theta > 1$, convective motion may change from that of pure internal heating or that of pure wall heating. Figure 2.11 shows profiles of perturbation velocity $\tilde{w}$. The profile without wall heating is symmetrical with respect to the horizontal centerline of the fluid layer. The profile with large value of $\Theta$, $\Theta = 20$, however, becomes asymmetric and the position of the maximum $\tilde{w}$ moves to upward. Therefore the center of convective motion is displaced to upward. As already mentioned in the last section, convective motion of internally heated convection is potentially asymmetric, and then a local stable layer formed near the bottom may enhance such asymmetric convective motion.

### 2.5.2 With distributed internal heating

Formation of a local stable layer in the combination of internal heating and wall heating at the bottom and symmetry breaking of a profile of velocity perturbation $\tilde{w}$ were discussed. Distributed internal heating in which heat source concentrates on the top boundary makes a quasi-stable layer and also induces such a symmetry breaking as mentioned in the last section. Such distributed internal heat source may accelerate asymmetry of $\tilde{w}$ in convection which has internal heating and wall heating at the bottom. Formation of a local stable layer and asymmetry of $\tilde{w}$ are investigated.

Temperature profile in conduction state is derived as

$$\bar{T} = \frac{\bar{T}^* - T_1}{T_2 - T_1} = -\Theta_\eta f(z,\eta) + (\Theta_\eta - 1)\, z + 1, \tag{2.35}$$

$$\text{where} \quad \Theta_\eta = \frac{H_0 L^2 \eta^2}{\lambda (T_2 - T_1)},$$

$$\text{and} \quad f(z,\eta) = e^{-1/\eta}\left(e^{z/\eta} + z - 1\right), \quad 0 \le f(z,\eta) \le 1 \ \text{ for } \ 0 \le z \le 1, \ \eta \ge 0.$$

This equation and parameter $\Theta_\eta$ are generalized temperature profile of equation (2.33) and generalized parameter of $\Theta$, and $\Theta_\eta$ is also an important parameter of the form of temperature profile. Figure 2.12 shows temperature profile for $\Theta_\eta = 0.6$ and that for $\Theta_\eta = 1.5$, where $\eta = 0.2$. As shown in this figure, a local stable layer is not formed in the case with $\Theta_\eta = 0.6$ but is formed at $\Theta_\eta = 1.5$ in the lower part of the fluid layer. Its height $h_\mathrm{s}$ becomes approximately half of the fluid layer although $\Theta_\eta$ is still small. It is easy to derive from equation (2.35) that

$$h_\mathrm{s} = \eta \ln \left\{ \eta \left[1 - e^{-1/\eta}\right] - \frac{\eta}{\Theta_\eta} \right\} + 1, \qquad \lim_{\eta \to \infty} h_\mathrm{s} = 1.$$

This equation shows that height of a stable layer for large $\Theta_\eta$ becomes large beyond half height of the fluid layer, which is the maximum height in uniform heating case. Such thicker stable layer enhances asymmetry of $\tilde{w}$ than in wall heating with uniform internal heating in which it needs large value of $\Theta$. For instance, at $\eta = 0.2$ and $\Theta_\eta$, the center of the circulation in which $\tilde{w}$ is the maximum moves to upward by 5% of height of the fluid layer even small value of $\Theta_\eta$.

Perturbation equations for this problem are derived. By substituting equation (2.35) into equation (2.16), it becomes

$$\left(\frac{d^2}{dz^2} - k^2 - \sigma\right)\tilde{T} = -\left\{ \frac{\Theta_\eta}{\eta} \exp\left(\frac{z-1}{\eta}\right) - \Theta_\eta \left[1 - \exp\left(-\frac{1}{\eta}\right)\right] + 1 \right\} \tilde{w}. \tag{2.36}$$

From equation (2.15),

$$\left(\frac{d^2}{dz^2} - k^2 - \frac{\sigma}{Pr}\right)\left(\frac{d^2}{dz^2} - k^2\right)\tilde{w} = Rk^2\tilde{T}. \tag{2.37}$$

where this Rayleigh number is the external Rayleigh number expressed as

$$R = \frac{g\beta(T_2 - T_1)L^3}{\nu_1 \kappa_1}. \tag{2.38}$$

Because both boundaries are isothermal, boundary conditions for temperature perturbation are

$$\tilde{T} = 0 \text{ at } z = 0, 1. \tag{2.39}$$

Stability analysis calculated $R_c$ and $k_c$ for each $\Theta$ with $\eta = 0.2$ as shown in Figure 2.13. $\Theta_\eta = 0$ means no internal heating, namely this case is the same to Rayleigh-Bénard convection. Here critical values calculated in Reid & Harris [38] are used as critical values at $\Theta_\eta = 0$. $R_c$ increases monotonically with respect to $\Theta_\eta$. When $\Theta_\eta \leq 1$, temperature gradient at the bottom becomes small with increase of $\Theta_\eta$, and then inflow of heat at the bottom becomes small. On the other hand, when $\Theta_\eta > 1$, reversal of temperature gradient near the bottom causes outflow of heat at the bottom. These might increase $R_c$. The slope of variation of $k_c$ with respect to $\Theta_\eta$ increases greatly from $\Theta_\eta = 1$. Therefore an increase of wavenumber may be induced by formation of a local stable layer.

## 2.6 Conclusion

Linear stability analysis was used to clarify the effects of heat source distribution on internally heated convection. The conditions for the onset of convection, namely the critical Rayleigh number $R_c$ and critical wavenumber $k_c$, were determined for non-uniform distributions of heat source in which heat source is concentrated in the lower or the upper part of the fluid layer. Concerning the effects of the heat source distribution a function of $R_c$ and $k_c$, (defined with respect to the characteristic length of the source distribution), the following conclusions have been drawn. Concentration of the heat source near the bottom boundary lowers $R_c$ and eases convection occurring, namely it lowers the temperature difference at which convection occurs. Variation of $k_c$, however, is small, and there is only a slight influence of this distribution on the size of the convection cell. Concentration of the heat source near the top boundary increases $R_c$ and prevents convection occurring. When the concentration is extreme, with extremely small $\eta$, $k_c$ changes greatly in contrast to when the heat source is concentrated near the lower boundary. Furthermore, an asymmetry of the vertical velocity $\tilde{w}$ appears, and then convective flow near the bottom boundary becomes weak. These variations of the characteristics of convective motion may be caused by a quasi-stable layer formed on the lower part of the fluid layer. In common with both heat source distributions, even a slight deviation from uniform heating induces a large difference in the total power input, even though the temperature profiles are similar.

"Mixed convection" where wall heating at the bottom boundary is combined with internal heating was also investigated. The dimensionless parameter $\Theta$, defined as the ratio of internal to external Rayleigh number, determines the form of the temperature profile. A local stable layer in which temperature increases in the vertical direction is formed near the bottom boundary when $\Theta$ is greater than 1, and a temperature profile similar to pure internally heated convection for $\Theta < 1$. For large values of $\Theta$ a strong asymmetry in the vertical velocity $\tilde{w}$ appears, and flow near the bottom boundary becomes weak. When the heat source distribution is non-uniform and concentrated near the upper boundary, an asymmetry appears even for small internal Rayleigh numbers; that is, small value of $\Theta_\eta$. The local stable layer formed in this case is thicker than for uniform internal heating. It spreads into the upper half of the fluid layer even for a small value of $\Theta_\eta$. Such a local stable layer might cause a large change in $R_c$ and $k_c$.

The system investigated in this study is typical in nature and may be different in industrial configurations. The results, however, might be common characteristics related to many convective phenomena. Asymmetry of convective motion caused by a local stable layer is typical of internally heated convection with distributed internal heat source. It is often explained that such asymmetry is caused by temperature dependence of physical properties such as kinematic viscosity. But it might happen even in the ideal system without such a temperature dependence.

As mentioned in the Chapter 1, an improved experiment for internally heated convection will be explained in Chapter 3 and we have found that the cell undergoes elongation with increasing $R_\mathrm{I}$. The wavelength changes by nearly 100% in the range $R_\mathrm{I} = 2700$ to 8100. In my experiment, the heat source is not strongly concentrated near the upper boundary as modeled here, and this elongation of the cell might not be caused by non-uniform distribution of heat source as concluded from the present results.

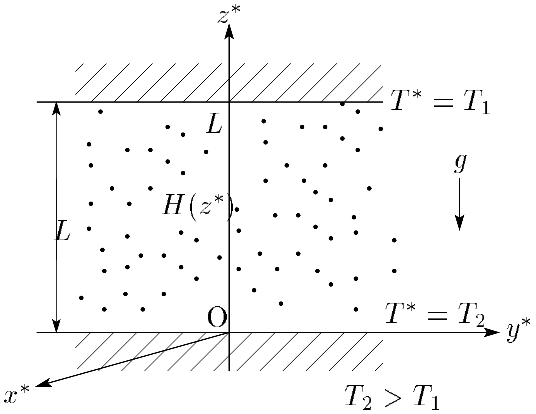

Figure 2.9: Coordinates and symbols for mixed convection, combination of internal heating with the wall heating from below

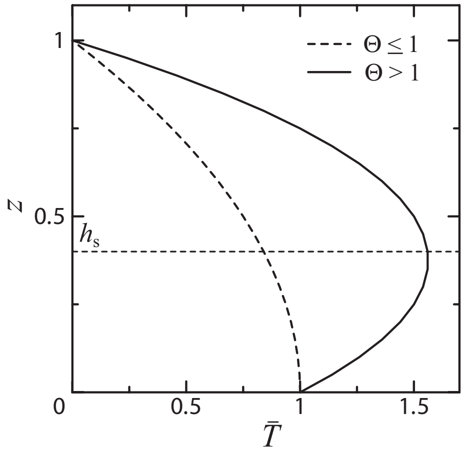

Figure 2.10: Comparison of temperature profiles for difference $\Theta$; solid line $\Theta \leq 1$ and broken line $\Theta > 1$. $h_s$ shows height of local stable layer in which temperature gradient is positive for the vertical direction.

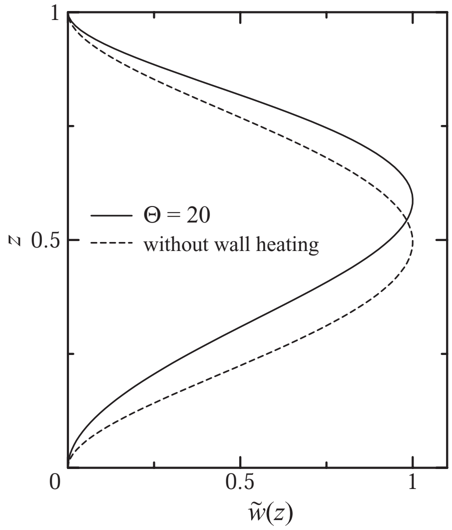

Figure 2.11: Comparison of perturbation velocity profiles $\tilde{w}(z)$; solid line $\Theta = 20$ and broken line internally heated layer without wall heating.

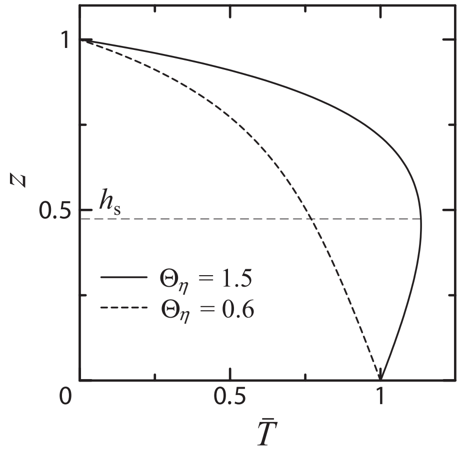

Figure 2.12: Comparison of temperature profiles for difference $\Theta_\eta$ at $\eta = 0.2$; solid line $\Theta_\eta = 1.5$ and broken line $\Theta_\eta = 0.6$. $h_\mathrm{s}$ shows height of local stable layer in which temperature gradient is positive for the vertical direction.

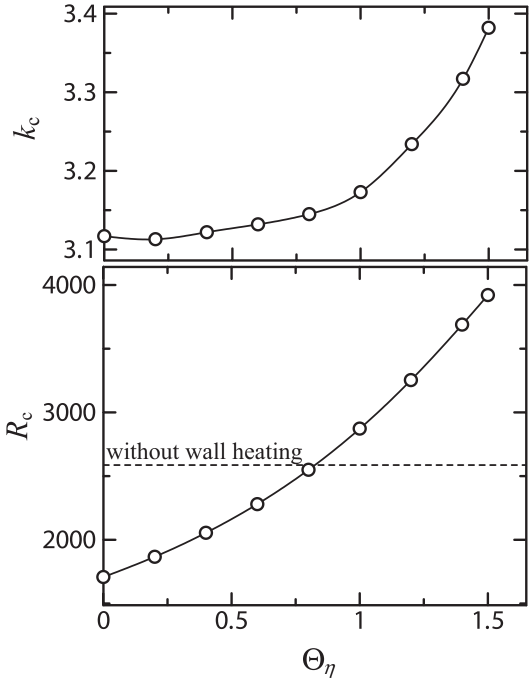

Figure 2.13: Variation of critical Rayleigh number $R_c$ (below) and critical wavenumber $k_c$ (above) versus $\Theta_\eta$ at $\eta = 0.2$, broken line expresses $R_c$ for distributed internal heating with $\eta = 0.2$ without wall heating.

## Chapter 3

# Experiment on Internally Heated Convection

## Abstract

Natural convection induced by internal heat generation has various interesting characteristics, for instance convection cell dilatation. These characteristics are reexamined in this chapter using new experimental methods and an improved experimental apparatus in order to reduce uncertainties as much as possible. The convective motion in the fluid layer was visualized using reflecting particles (Kalliroscope) and independently using a suspension of Thermochromic Liquid Crystal; the latter technique also allowed the simultaneous investigation of the temperature field. Cell dilatation was conformed in the improved experimental apparatus and then investigated quantitatively by extracting the pattern wavenumber from Fourier analysis of the images recorded by a digital camera. The pattern wavenumber was found to increase with increasing Rayleigh number. We compare our results with earlier investigations and discuss the influence of the thermal boundary condition at the bottom of the fluid layer on the variation of the wavenumber. Disagreement between experimental and theoretical study on the cell dilatation is discussed qualitatively.

## 3.1 Introduction

### 3.1.1 Characteristics of internally heated convection

Several characteristics of the internally heated convection were already mentioned in earlier studies [22, 23], which are (a) 3-dimensional and irregular cell shape, (b) cell arrangement aligned with electric current, (c) localized descending flow at the center of a cell and (d) drastic cell dilatation with respect to internal Rayleigh number. There are, however, many problems in the earlier studies, therefore these characteristics should be reexamined. Moreover a method was almost only classical observation of convective motion. We confirm these characteristics, especially drastic cell dilatation, by using innovative method in improved experimental setup.

### 3.1.2 Problems with previous studies

Three problems criticism of past studies that we address in the work reported here are: (1) After convection cells appear, the temperature field in the fluid layer becomes non-uniformity in the horizontal directions. This temperature variation induces non-uniformity in the electrical conductivity of the fluid. As a result, the amount of internal heat generation also varies in the horizontal directions. This problem was already pointed out by Schwiderski & Schwab [23]. (2) For convenience the theoretical studies assumed adiabatic boundary for the bottom plate. However, the true boundary condition was non-adiabatic – the experiments used a bottom plate made of Plexiglas or glass. Thus in the experiments a local stable layer where the temperature increases in the vertical direction formed in the fluid layer near the bottom plate. This stable layer may causes the critical Rayleigh number and critical wavenumber to vary, as estimated by Sparrow *et al.* [26] and Kulacki & Goldstein [39]. (3) Schwiderski & Schwab [23] estimated the diameter of a convection cell identified in a photograph and showed that it varied as a function of the internal Rayleigh number. Clearly their method of estimation lacks objectivity.

In this experiments we used a more precise experimental setup minimized or eliminated the first and second difficulties described above. We also studied the variation of the cell dilatation with Rayleigh number more systematically and objectively by measuring the pattern wavenumber using Fourier transform of images of both the convective motion and the temperature field taken by a digital camera.

## 3.2 Configurations

Figure 3.1 shows coordinates and thermal boundary conditions of this problem, where spatial variables $x$, $y$ and $z$ have dimension unlike in Chapter 2. The horizontal fluid layer with thickness $L$ is sandwiched between two rigid plates and that are unbounded in the horizontal directions. The fluid layer generates heat uniformly at rate $H$ per unit time and per unit volume. To emphasize only the effect of internal heat generation, the thermal boundary conditions on the top and the bottom plate were set as isothermal and adiabatic, respectively. The control parameter in this problem is internal Rayleigh number, which was already explained in Section 2.1, defined as

$$R_{\mathrm{I}} = \frac{g\beta H L^5}{2\lambda\kappa\nu}, \tag{3.1}$$

where $g$ is gravity, $\beta$, $\lambda$, $\kappa$ and $\nu$ are thermal expansion coefficient, thermal conductivity, thermal diffusivity and kinematic viscosity of the fluid respectively. Instead of $R_{\mathrm{I}}$, we use the reduced internal Rayleigh number $R_{\mathrm{I}}^* = R_{\mathrm{I}}/R_{\mathrm{c}}$, where $R_{\mathrm{c}}$ is critical Rayleigh number and Roberts's calculations yield $R_{\mathrm{c}} = 1386$ [27].

## 3.3 Experimental setup and method

### 3.3.1 Experimental apparatus

The experimental apparatus was designed and constructed in order to minimize non-uniformities in the internal heat generation and to realize the adiabatic boundary condition at the bottom of the fluid layer. Figure 3.2 shows the schematic illustration of the experimental apparatus, and Figure 3.3 shows photographs of the apparatus. The apparatus mainly consists of two parts, a fluid container shown in Figure 3.3(a) and a cooling part as the lid of the container also shown in Figure 3.3(b). All but the bottom plate of the fluid container is made of Plexiglas with a thickness of 10 mm. Horizontal area of the container is a nearly square with sides measuring 220 mm and 210 mm, and the plate separation is 7 mm, yielding an aspect ratio of 30. In order to realize the adiabatic condition, 6 mm vacuumed glass with 0.2 mm vacuumed space (to $10^{-6}$ atm), is used as the bottom plate. The heat flux through the bottom plate is reduced to one third the maximum heat flux of a Plexiglas plate. Moreover, the vacuum glass is transparent, and thus it becomes easy to take photographs of the fluid layer. Photographs of the fluid layer were taken from the bottom by setting a mirror under the fluid container at an angle of 45 degrees from the horizontal.

The lid of the container, the cooling part, is an aluminum block 18 mm thick. The temperature at the bottom surface of this block was kept constant by flowing water over the lid. The temperature of the flowing water was controlled by a thermostatic bath to within ±0.1 °C. The water temperature was initially set to room temperature, which is about 20 °C, to reduce an initial perturbation in the fluid and heat flux through the sidewall of the container. The bottom of the aluminum block was coated with black paint for the sake of electric insulation and visualization. The height of fluid layer (7 mm) was about 1.5 times greater than that used in previous experimenal studies [22, 23]. Therefore, to achieve the same internal Rayleigh number as used in previous experiments, the amount of internal heat generation was reduced to one eighth that used in previous studies [22, 23].

A 0.5 wt % potassium chloride (KCl) solution was used as the ionic fluid. In comparison with past studies, this ionic fluid has a small electric conductivity and furthermore is only weakly dependent on temperature. Copper electrodes were located at the both sides of the fluid layer. There were 5 mm gaps between the electrodes and the aluminum lid in order to remove bubbles generated by electrolysis and also to insulate electrically between the both metals. A stabilized AC power supply, NF model EPX4104, was used for electric heating to avoid bubble generation at the electrodes. The ACPS was driven with 50 Hz but there was no time depending phenomenon in the fluid layer.

2 digital multimeters (DMM) were used as the auxiliary apparatus for measurement of electric current and electric potential. These were connected to the fluid layer in parallel or serial as shown in Figure 3.4(a). Minimum measurable ranges of these DMMs are 1 $\mu$A for electric current and 1 mV for electric potential. Figure 3.4(b) is a photographs of an assembled experimental setup with DMMs. Table 2 shows specifications of the experimental setup.

### 3.3.2 Verification of apparatus and determination of internal Rayleigh number in the experiment

#### Uniformity of temperature on the cooling plate

In the experiments, heat exchange between the cooling plate and the cooling water may not be uniform for each position at the top surface of the cooling plate, and the temperature field at the top surface may be also non-uniform. This non-uniformity of the temperature

Table 3.1: Specifications of the experimental setup

| | |
|---|---|
| Fluid container | |
| Size | 220 mm (including 5 mm gaps) × 210 mm × 7 mm |
| Lateral wall | 10 mm thick Plexiglas |
| Bottom plate | vacuumed glass (which has $10^{-6}$ atm vacuum layer) |
| Lid of the container | |
| Material | 18 mm thick aluminum block |
| Cooling | flowing water by thermostatic bath |
| Ionic liquid | 0.5 wt % potassium chloride (KCl) solution |
| Electrode | 1 mm thick copper plate |
| Power supply | stabilized AC power supply, NF model EPX4104 |
| Ammeter | DMM with 1 $\mu$A minimum measurable range |
| Voltmeter | DMM with 1 mV minimum measurable range |

field is, however, almost reduced at the bottom surface of the cooling plate because material of this plate, aluminum, has high thermal conductivity and this block is enough thick to even out temperature. The non-uniformity of the temperature may induce the temperature perturbation in the fluid layer and changes the problem more complex. We confirmed the uniformity by measuring the temperature field using a K-type thermocouple. Figure 3.5 shows the temperature field at the bottom surface, where setting temperature is 20 °C and an interval of the measuring point is 21 mm in the horizontal axes. The temperature is slightly large at the left side of the fluid layer, but this difference is only 1 % at the maximum for the setting temperature. An average of the surface temperature is 20.0 °C and a standard deviation is only less than 0.4 % for the average. It may show that temperature is enough uniform.

### Uniformity of heat generation

As already mentioned, it has been assumed that internal heat generation is uniform. After convection cells appear, however, the temperature field in the fluid layer becomes non-uniform and varies in the horizontal directions. This temperature variation induces non-uniformity in the electrical conductivity of the fluid. As a result, the amount of internal heat generation also varies in the horizontal directions. It is not possible to wholly eliminate the non-uniformity. In actual experiment, moreover, it may not be completely uniform although before convection cells appear. We estimated such non-uniformity induced by the setting configuration, which are location of the electrodes and so on.

Amount of heat generation is determined by a product of electric current and difference of electric potential. If the concentration of the ionic solution is enough uniform at the initial condition, measuring the difference of electric potential can estimate non-uniformity of heat generation. Electric potential was measured at each position overall the horizontal fluid layer, whose temperature is kept constant. Height of the measurement position is $z = 5$ mm and an interval in the horizontal directions is 30 mm. Figure 3.6 shows the contour of electric potential for two conditions of electric current and voltage between the electrodes, where the shown value is the difference of electric potential from the left side electrode. As shown in this figure, electric potential in the fluid layer is almost uniform, and standard deviation of the difference of electric potential is 1% for the average at the both conditions. It is negligibly small because this deviation appears as square in heat generation.

The variation of electric potential in the vertical direction was also measured with 1 mm interval as shown in Figure 3.7 in order to estimate non-uniformity of heat generation in the vertical direction. As already discussed in Chapter 2, even heat source distribution with slight deviation induces large difference of critical Rayleigh number. In the present configuration, such deviation, however, was 0.2 % at a maximum overall measuring points in the horizontal plane, and corresponds to $\varepsilon$, $\eta > 100$ in distributed internal heating defined in Chapter 2. Furthermore this distribution of voltage has no regular trend. Therefore we can conclude that this deviation makes no influence for the convection.

### Variation of electric power

Internal heat generation is realized as Joule heating induced by passing electric current through the fluid layer, and its amount per unit volume and per unit time is determined from Joule's low defined as $H = I \times E/V$, where $I$ is effective value of electric current, $E$ effective value of difference of electric potential between both electrodes and $V$ volume of the fluid layer. Since electric conductivity in ionic liquid depends on temperature, which generally increases with respect to temperature, electric current passing fluid layer slightly increases with respect to mean temperature in the fluid layer. Figure 3.8 shows a variation of electric power, which is a product of $I$ and $E$, with respect to time, where initial values are 3.29 W, 26.3 V and 125.4 mA. Electric power slightly increases, and then it reaches equilibrium state after two hours. At this time convective motion also becomes equilibrium. The equilibrium value is larger than initial value with 7 %, and this value was used for the determination of internal Rayleigh number $R_{\mathrm{I}}$.

### 3.3.3 Visualization

Kalliroscope, AQ-1000 rheoscopic concentration [43], was used in order to visualize the fluid motion. It is a suspension of microscopic crystalline platelets, which has size of $6 \times 30 \times 0.07$ $\mu$m and is made from guanine, 1.62 g/cm$^3$ density, and these platelets are aligned parallel to the planes of share flow [44, 45]. By incident light sheet it can visualize large-scale fluid motion easily as contrast of brightness. Moreover it does not make chemical reaction; therefore it may be extremely useful for the experiment of internally heated convection. Figure 3.9 shows an example of a flow visualized by Kalliroscope, which is the fluid flow passing a circular cylinder, i.e. Karmann vortices.

A visualized fluid motion, however, is not a physical variable, which characterizes the convective phenomena quantitatively. Thermo-chromic Liquid Crystals (TLC), Japan capsule products type KW, was also used for the visualization of the temperature field. TLC is a microcapsule of liquid crystal, which changes its color with respect to temperature, where the microcapsule has 10$\sim$20 $\mu$m diameter and $1.01 \sim 1.02$ g/cm$^3$ density. Suspension of TLC, therefore, can easily visualize the instantaneous temperature filed, and then it is a great tool to investigate heat transfer in the fluid [40, 41]. It has no guarantee for chemical and electrical reaction, but there was no an especial problem induced by such reactions during the experiments.

Visualized photographs were taken from the bottom of the fluid container through the transparent vacuumed glass by a digital camera, Nikon D1X. Light sheet generated by a halogen lamp, Moritex MHF-G150LR, was emitted in the middle height of the fluid layer. Thickness of the sheet is about 2 mm (Figure 3.10). These photographs have a lot of image elements about 1500 times 1500 pixels for accurate analysis of the images.

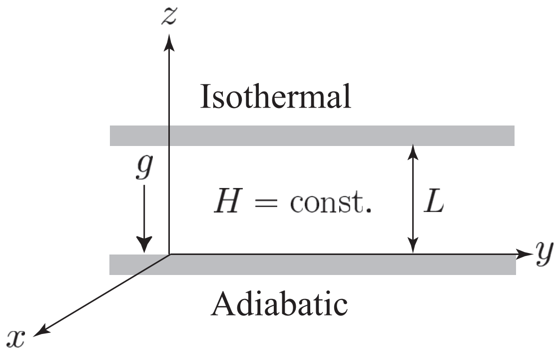

Figure 3.1: Coordinates and thermal boundary conditions; The top boundary is isothermal and the bottom adiabatic. Two rigid plates are unbounded in the horizontal directions.

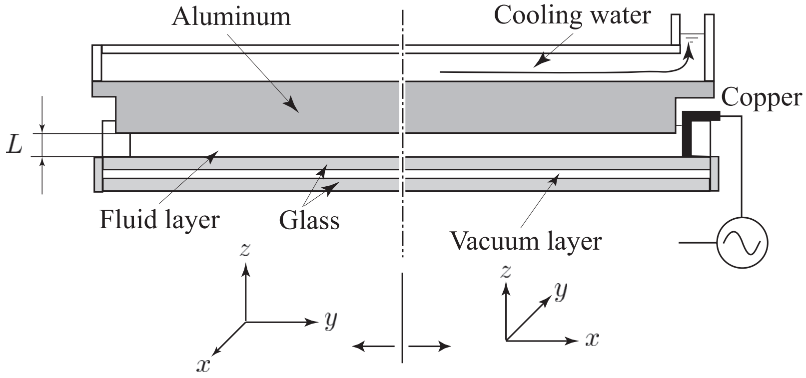

Figure 3.2: Schematic illustration of experimental apparatus; $y - z$ cross section (left) and $z - x$ cross section (right).

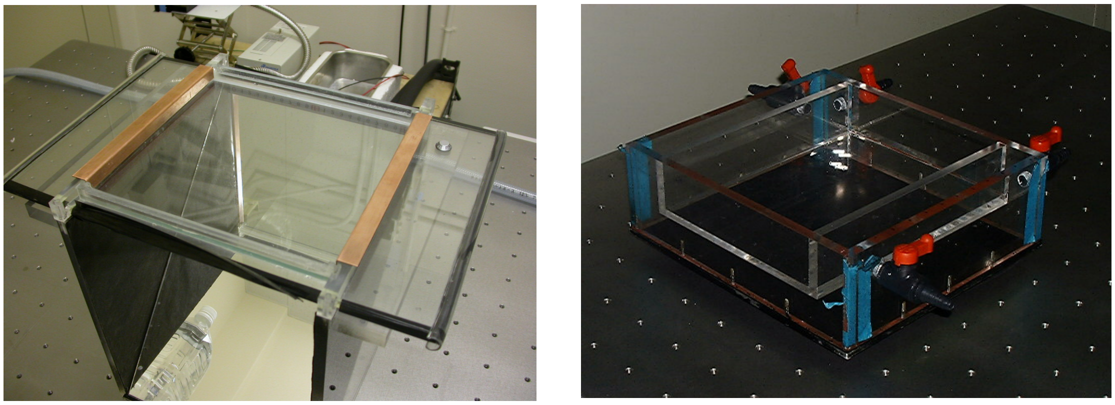

(a) Fluid container

(b) Cooling part

Figure 3.3: Photographs of experimental apparatus; (a) Fluid container and (b) Cooling part as the lid of the container.

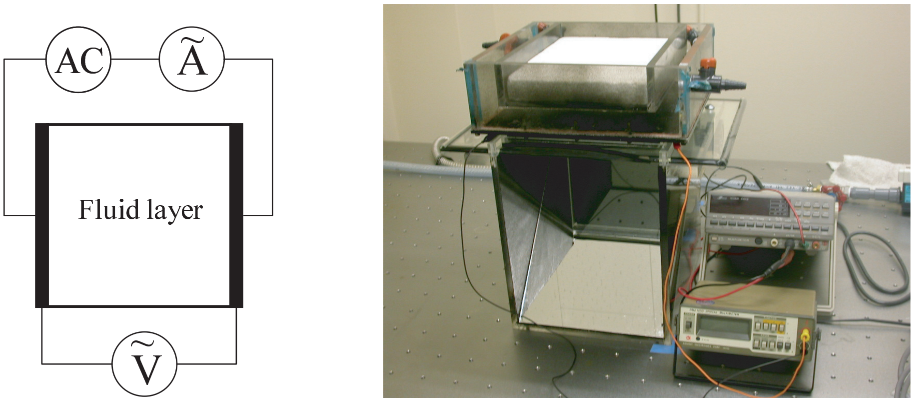

(a) Schematic illustration

(b) Photograph

Figure 3.4: Connection of DMMs with the fluid layer.

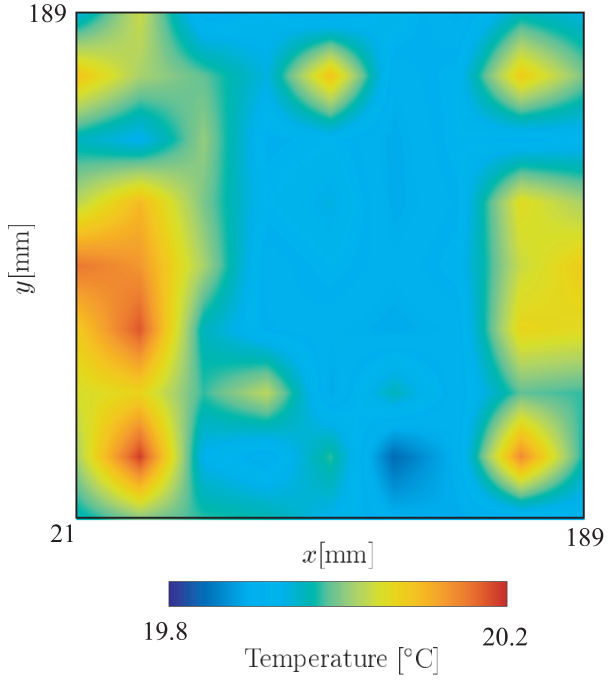

Figure 3.5: The temperature field at the bottom surface of the cooling plate.

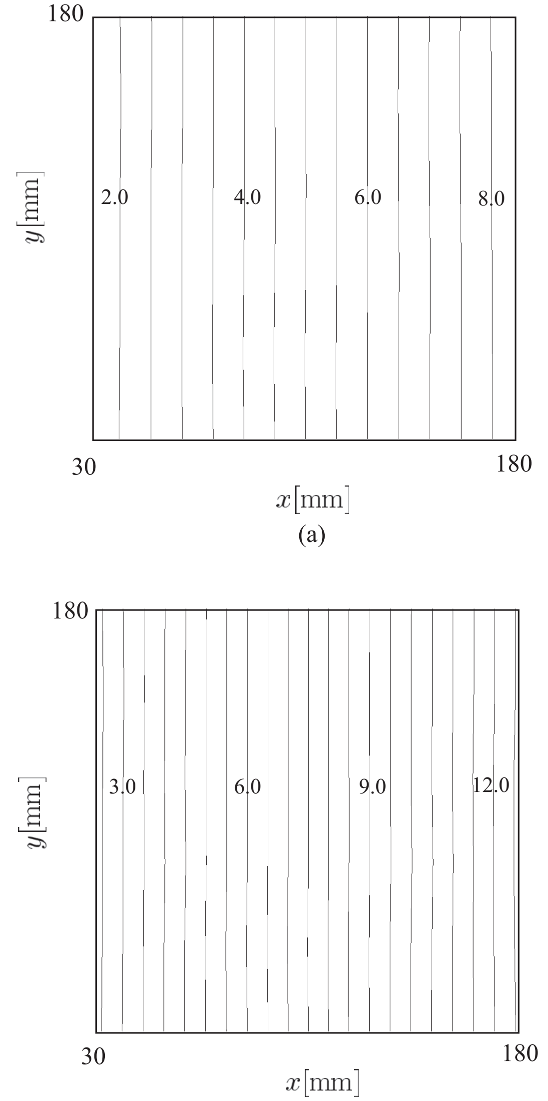

(b)

Figure 3.6: Contour of electric potential in the fluid layer; (a)10V, 0.05A and (b) 15V and 0.1A (these voltages show interelectrode potential).

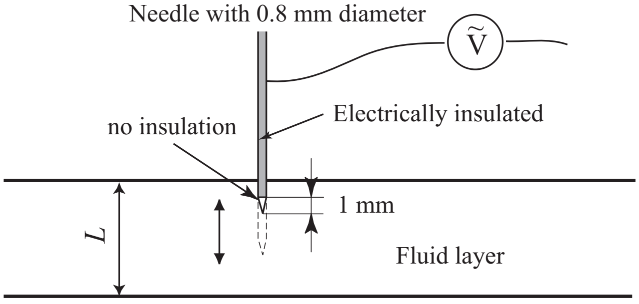

Figure 3.7: Schematic illustration of the measurement setup for measureing the vertical voltage distribution.

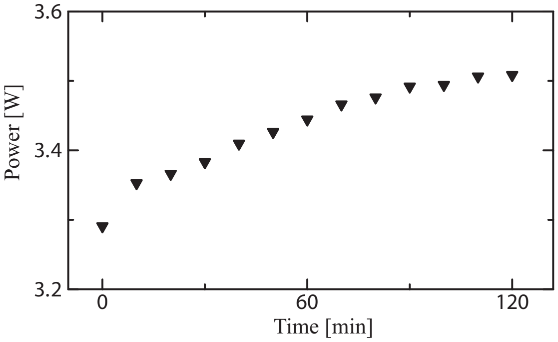

Figure 3.8: Variation of electric power with respect to power distribution time.

Figure 3.9: Example of flow visualized by Kalliroscope [43]: Karmann vortices behind a circular cylinder.

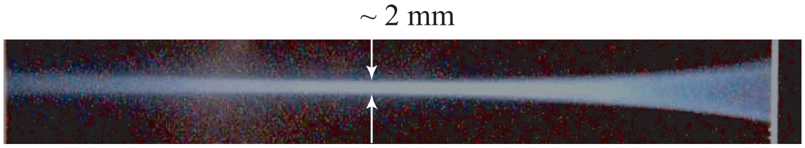

Figure 3.10: Visualized photograph of light sheet for the visualization. Its thickness is approximately 2 mm.

## 3.4 Results and discussions

### 3.4.1 Visualization

**Evolution of convection cells**

Figure 3.11 shows the evolution of convection cells after the fluid layer is suddenly added a setting voltage. Figure 3.11(a) shows the fluid layer immediately after adding voltage, where the electrodes are located at the both horizontal sides of the fluid layer. There is no perturbation in the center of the layer, but a roll like convection cell appears near the top and the bottom side in a photograph. Temperature difference between inside and outside of the fluid layer may induce these roll cells. A local convective motion appears as black spot overall the fluid layer, and roll cells appear near the left and the right side (Figure 3.11(b)). Such local motion gradually change into a bending roll cell (Figure 3.11(c)). In Figure 3.11(d) and (e) roll cells repeats breakup and fusion, and becomes individual polygonal cell, whose size is nearly constant. The shape of the cell changes into a quasi-hexagon (Figure 3.11(f) to (h)), where each cell fringed by various color lines in the photographs shows the same cell. In addition roll cells near the every side of the fluid layer remains in the equilibrium state (Figure 3.11(h)).

Figure 3.12 shows the evolution of convection cells when heat generation increases gradually with a constant rate. Variation of electric power is an approximate linear function of time (Figure 3.13), and its rate is about 0.18 W per 6 min, which is equivalent to 0.08 W per 6 min in increase of $R_{\mathrm{I}}^*$. There is no convective motion immediate aftermath of adding small voltage (Figure 3.12(a)). In Figure 3.12(b), a local convective motion seems everywhere as a distributed black spot. At about half value of critical rayleigh number, roll cells perpendicular to the both electrodes appear near the electrodes, and at the center of the fluid layer there is complex convective motion (Figure 3.12(c)). At slightly under the critical Rayleigh number, $R_{\mathrm{I}}^* = 0.92$, roll cells near the electrodes remains as the same shape but such complex convective motion changes to an organized motion like a meandering roll (Figure 3.12(d)). Such roll cell gradually changes into an individual-small cell with respect to $R_{\mathrm{I}}^*$, and instead of these roll cells irregular polygonal cells spread over the fluid layer (Figure 3.12(e)). These polygonal cells eventually become a quasi-hexagonal cell similar to convection cell in the case that the fluid layer is suddenly added setting voltage shown in Figure 3.11 in the equilibrium state (Figure 3.12(f)). Finally there is no difference between both ways of adding voltage, and then we choose the first way to add voltage. In this experiment, an organized convective motion appeared at near the critical Rayleigh number calculated by Roberts [27] and this observation supports his calculation.

### Convective motion

Photographs of convection patterns for 3 values of $R_{\mathrm{I}}^{*}$ are shown in Figure 3.14. Each picture was taken after convection pattern relaxed to a time-independent steady state. This took about 2 hours in the experiments. The white square in the upper right corner of these photographs is an indication of $2L$. A light sheet was emitted from above in these photographs. The copper electrodes were located on the both sides and then the direction of the electric current in these photographs is the horizontal direction, i.e. $x$-direction.

There are cells with irregular shape in every photograph taken at different $R_{\mathrm{I}}^{*}$ and this is in accord with the results of the past studies [22, 23]. As is well known, the shape of a convection cell in Rayleigh-Bénard convection at Rayleigh numbers, slightly larger than the critical Rayleigh number, is a two-dimensional roll. In these experiments, however, the convectin cell has a polygonal (nearly hexagonal) shape. The same experiment with a thinner fluid layer with 3 mm thickness was performed and the patterns were similar, irregular hexagonal shape. This result confirmed that the irregularity of the cell shape may not be induced by variation of physical properties in the vertical direction, which is caused by a thicker fluid layer. This irregularity of cell shape in the internally heated convection may be induced by the wide range of a selectable wavenumber. As already mentioned in Chapter 2, a neutral stability curve of internally heated convection has a wider range of a wavenumber than in Rayleigh-Bénard convection especially in the small side, and a slope of the curve near the critical Rayleigh number is flatter than in Rayleigh-Bénard convection as shown in Figure 3.15. Schwiderski & Schwab [23] pointed out that the arrangement of cells depends on the direction of the electric current and cells are arranged as shown in Figure 3.16. However, in these experiments we could find no significant dependence of the arrangement on the direction of the current.

Because we used a thick fluid layer in order to reduce internal heat generation non-uniformity, we expected the cell dilatation to be much weaker in the present experiments compared to previous studies [22, 23]. However, as the photographs illustrate, the convection cells clearly expand while at the same time keeping their shape as $R_{\mathrm{I}}^*$ increases.

At large $R_{\mathrm{I}}^*$, about $R_{\mathrm{I}}^* > 8$, the cell dilatation saturates by influence of the lateral wall or other reasons. When $R_{\mathrm{I}}^*$ increase furthermore, a different cell structure appears as shown in Figure 3.17(a), which has double circulations in a cell, namely flow ascends at the periphery and the center of a cell, and descends at the middle position between the center and the periphery as shown by a schematic illustration of circulation (Figure 3.17(b)). Such "double cell structure" was observed by Schwiderski & Schwab at similar $R_{\mathrm{I}}^*$. This structure, however, was unstable in their observation, and they concluded that the double cell structure is a transitional state to the single-polygonal cell. But this particular cell structure stably existed during present experiment, 2 hours or more, and it became a stable cell structure at least. Convection cells at large $R_{\mathrm{I}}^*$, $R_{\mathrm{I}}^* \sim 21$, are obviously influenced by the lateral wall of the fluid container, and a stability of this double cell structure may strongly depend on the size of the fluid layer. Transition to the double cell structure will be discussed in the next chapter.

### Temperature field

We also studied the shape of cells from photographs of the TLC visualized temperature field. The photographs in Figure 3.18 show the temperature field in the fluid layer for three value of $R_{\mathrm{I}}^*$. TLC responds to higher temperature by turning blue and to lower temperatures bu turning red. An intermediate range of temperature is expressed by continuous variation of color from red to blue, which includes green in the half way. The range of temperature, which can be used in the experiment, is determined by the kind of TLC. In this experiment the range was usually from 23 to 28 °C.

Temperature in the horizontal layer is distributed concentrically about the center of a convection cell until it reaches the lateral boundary of an adjacent cell. This temperature distribution is similar to the mathematical model of a hexagonal cell suggested by Christopherson [42]. This model is expressed as

$$T(x, y, z) = \hat{T}(z) \left\{ \cos\left[\frac{k}{2}\left(\sqrt{3}x + y\right)\right] + \cos\left[\frac{k}{2}\left(\sqrt{3}x - y\right)\right] + \cos(ky) \right\}, \tag{3.2}$$

where $k$ is a horizontal wavenumber. Temperature field according to this model is shown in Figure 3.19. After this, we assume that cell shape can be expressed by this this mathematical model.

The photographs visualized with TLC also show irregular cell patterns and dilatation of the convection cell that varies with $R_{\mathrm{I}}^{*}$. Moreover the colors in the photographs show the flow direction in a cell. Namely, the fluid descends in the center of the cell and ascends along the polygonal outer boundary. These directions are the reverse of those found in Bénard convection cells (Figure 3.20). Localized descending flow in the cell center was previously observed in an experiment at high Rayleigh number [34], in a numerical simulation [35], and in an experiment for internal heated convection with external heating at the bottom [30]. Therefore the descending flow in the center may be characteristic of convection driven by internal heating.

### 3.4.2 Qualitative explanation for the flow direction in a cell

As shown in the last section, localized descending flow appears at the center of a cell in internally heated convection. Such flow circulation in a cell was already mentioned in previous studies, Tritton & Zarraga [22], Schwiderski & Schwab [23], moreover the present study expressed the descending flow by the temperature field. We will explain the reason of occurring such descending flow simply.

Chandrasekhar [4] explained occurring convection as follows:

> *Instability occurs at the minimum temperature gradient at which a balance can be steadily maintained between the kinetic energy dissipated by viscosity and the internal energy released by the buoyancy.*

Figure 3.21 shows the temperature profile in the conduction state as the solution of the equation of heat conduction. The temperature profile in Rayleigh-Bénard convection is a linear function of the vertical direction, however, that in internally heated convection is not a linear function, it varies parabolically in the vertical direction. According to Equation (2.4) discussed in Section 2, gradient of buoyancy is not uniform in internally heated convection. If viscous dissipation of kinetic energy is the same overall the fluid layer, at first the balance may break up near the upper boundary and a local convective motion occurs, it is, of course, descending flow. Descending flow is the essence in internally heated convection and ascending flow is induced by continuity of the fluid.

An influence of a non-linear temperature profile on the form of a convection cell has been discussed in Rayleigh-Bénard problem [46]–[51]. Weakly non-linear stability analysis for the non-linear temperature profile showed results as follows: In a non-linear temperature profile, which slightly deviates from the linear profile as concave upward, a roll cell or a hexagonal cell with ascending flow at the center (HU) is stable in the fluid layer. On the other hand, in a convex upward temperature profile, a hexagonal cell with descending flow (HD) becomes stable. Numerical and experimental studies support this result. Although the thermal boundary condition is different to Rayleigh-Bénard problem, temperature profile in the internally heated convection is convex upward and a cell shape observed in the experiment, HD, does not contradict this result.

In a discussion of such non-linear temperature profile, local Rayleigh number, which is defined as

$$R_\ell = \frac{g\beta(-dT/dz)L^4}{\kappa\nu}, \tag{3.3}$$

was used for explanation of stable cell shape [52]. It is a function of $z$ and contains a temperature gradient as derivative of a temperature profile in the vertical direction. Figure 3.22 shows profile of $R_\ell$ for the internally heated convection and for Rayleigh-Bénard convection. A profile of $R_\ell$ in internally heated convection has the maximum at the top boundary, then convective motion may occur near the top boundary, i.e. descending flow. On the other hand, in Rayleigh-Bénard convection, the profile is constant, then ascending flow or descending flow generates in the same probability, namely a roll cell may appear.

### 3.4.3 Wavenumber analysis by Fourier transform

#### Analysis

In internally heated convection, a convection cell drastically expands with increasing $R_\mathrm{I}^*$ as shown in Figure 3.14 and also in Figure 3.18. These results are qualitatively similar to the earlier studies [22, 23]. Schwiderski & Schwab [23] estimated the cell dilatation as a function of $R_\mathrm{I}$ by estimating the diameter of a single cell identified in photographs of the patterns. However, as illustrated in the photographs shown in Figure 3.14, the boundary between cells is not very clear. Therefore the choice of which cell in the photograph to select for measurement, as well as the measurement of the cell diameter itself, cannot be made objectively. We have studied the cell dilatation more systematically and objectively by extracting the pattern wavenumber from the Fourier transform of the high resolution digital images.

Each element in a visualized image of convective motion has brightness information with 256 levels and this brightness is modulated in space by the convective motion of a cell. Therefore, we can determine the cell wavenumber from a Fourier analysis of this brightness variation. For instance, Figure 3.23(b) shows an extracted brightness variation on the horizontal centerline of the visualized photograph shown in Figure 3.23(a). There is a certain period in this figure. The result of Fourier transform is shown in Figure 3.23(c). The spectrum has a clear peak at $n = 21$, but meaning of peak number $n$ is not clear. The photograph shown in Figure 3.24 shows one convection cell. The brightness information on the straight line passing through the cell center varies periodically. One cell contains two periods of brightness variation but the length of a period is different for each line passing through the cell. If we can assumed that shape of a cell is regular hexagon, then from a simple thinking of statistics, an averaged period over the full area of a photograph equals to a length of the mean passing length of the circle, which has the same area with hexagonal convection cell. Details of this assumption will be explained in the next section. The scale attached on the apparatus was also taken at the same time in the photograph and it may tell us an actual scale of a cell. We can determine a wavenumber of convection cells by this way from an averaged spectrum. The true peak is determined by a parabolic approximation of three points, which contain a provisional peak point, in a spectrum. The half-width of this parabola expresses its error, which contains various uncertainties caused by effects of the side boundary, irregularities on the form of the convection cells, etc.

An image of the temperature field visualized by TLC is expressed in RGB system, which has three color components: Red $R$, Green $G$ and Blue $B$ with 256 levels respectively. This color system can express almost all colors as mixture of these components. Brightness can be calculated from the value of $G$ and $B$ as follows.

$$\text{Brightness} = 0.0565G + 5.5928B.$$

We can also obtain brightness information from an image of the temperature field, but a relationship between a period of a brightness variation and a wavenumber of a cell is different from the case of the fluid motion visualized by Kalliroscope. Figure 3.25(a) shows one cell extracted from a photograph of the temperature field and Figure 3.25(b) is a monotone image of this picture, namely it has only brightness information. Brightness information of a line passing through a convection cell is also changing periodically and one cell has one period of a brightness variation (3.25(c)). We can also obtain the cell wavenumber from these pictures by Fourier transform with the relationship between brightness information and the wavenumber. These results will be used for explanation of cell dilatation in the later section.

### Hypothesis for determination of wavenumber

Wavenumber given by Fourier transform of brightness information is not the true wavenumber of the convection, which is the horizontal wavenumber of perturbation defined in Section 2.2. It needs some hypothesis to determine the true wavenumber.

Following assumptions for the cell pattern observed are made.

1. A slope angle of a hexagonal cell $\theta$ defined in Figure 3.26(a) appears with the same probability in the range of $0 \leq \theta < \pi/3$.
2. Cell shape is irregular polygonal, which is regular hexagon with a slight deformation. And average of these becomes regular hexagon.
3. All cell has the same area and the convective phenomenon in the internally heated fluid layer has only one horizontal wavenumber.

According to assumption 1, if we measure a horizontal length of a cell through the center for many cells, the average of these may show the diameter of a circle $2r$, which has the same area of regular hexagonal cell with side $a$, as shown in Figure 3.26(b). In an actual measurement, furthermore, measuring lines of brightness information pass through every point on a cell, and average of these may show a mean length of lines which pass the circle. From above discussions, there is a following relationship between true wavenumber $k$ and wavenumber determined by Fourier transform of brightness information $k_{\mathrm{m}}$. Radius $r$ of a circle which has the same area of a hexagon with side $a$ is

$$r = \sqrt{\frac{3\sqrt{3}}{2\pi}}a.$$

Mean length of a passing line on a circle is

$$\lambda_{\mathrm{m}} = \frac{\pi}{2}r = \frac{\pi}{2}\sqrt{\frac{3\sqrt{3}}{2\pi}}a.$$

According to the definition of wavenumber,

$$k_{\mathrm{m}} = \frac{2\pi}{\lambda_{\mathrm{m}}} = \sqrt{\frac{2\pi}{3\sqrt{3}}}\frac{4}{a}.$$

In a mathematical model of a hexagonal cell suggested by Christopherson [42], expressed as equation (3.2),

$$k = \frac{4\pi}{3a}.$$

Therefore,

$$k = \frac{\pi}{3}\sqrt{\frac{3\sqrt{3}}{2\pi}}k_{\mathrm{m}} \simeq 0.952k_{\mathrm{m}}. \tag{3.4}$$

According to assumption 2 and 3, $k_{\mathrm{m}}$ is determined as a center value of a peak in wavenumber spectrum given by Fourier transform of brightness information.

### 3.4.4 Convection cell dilatation

We analyzed the wavenumber of convection cells from digital photographs of fluid motion taken for each $R_{\mathrm{I}}^{*}$. The analysis with Fourier transform was carried out to determine the wavenumber for parallel ($x$-direction) and perpendicular ($y$-direction) to the direction of the electric current.Figure 3.27 shows the results of the analysis, where $k$ is the cell horizontal wavenumber and the error bars for $k$ are half widths of the parabolas, which were used as estimation of $k$. A measurement deviation of electric current and voltage in the DMMs, which is explained in Section 3.1, determined error for $R_{\mathrm{I}}^{*}$, but was negligibly small. Values for the $y$-direction are slightly larger than for the $x$-direction, but these differences are within the range of the error bars for the wavenumber. Therefore, we conclude that the difference is not significant, and we use the average to represent the cell wavenumber for each $R_{\mathrm{I}}^{*}$.

Figure 3.28 shows the variation of the wavenumber $k$ estimated from the images of fluid motion visualized by Kalliroscope and from images of the temperature field visualized by TLC suspension, respectively. The results of Schwiderski & Schwab [23] and the critical wavenumber determined theoretically by Roberts [27] are also shown. The wavenumber decreases monotonically with respect to $R_{\mathrm{I}}^{*}$, and the solid line shows an approximate linear function of present data. The results calculated from images of a temperature field are slightly larger than results obtained from the fluid motion for each $R_{\mathrm{I}}^{*}$, but a discrepancy is not significant considerably the error bars, and a tendency of a variation is similar. The wavenumber decreases linearly with respect to $R_{\mathrm{I}}^{*}$ until $R_{\mathrm{I}}^{*} \sim 8$ and saturates beyond this value. This saturation might be induced by the influence of the lateral boundary. The wavenumber, however, does not become small beyond the stability curve calculated in Chapter 2, and approaches the curve asymptotically (Figure 3.29).

The slope of the variation in the data of Schwiderski & Schwab [23] is similar to the present data, but the their data is wholly larger than the present data beyond the range of the error bars. This difference might be caused by differences in the problem thermal boundary condition – we used an adiabatic boundary condition, while Schwiderski & Schwab [23] used Plexiglas, which has no negligible thermal conductivity. Figure 3.30 shows a schematic illustration of the temperature profile in the conduction state for the vertical direction. The temperature profile with thermal insulation, shown in this figure as a broken line, has the maximum at the bottom. On the other hand, without thermal insulation the maximum is not at the bottom but is at a higher position. Consequently a local stable layer with thickness $L_1$ is formed near the bottom, wherein temperature increases in the vertical direction. From the definition of the internal Rayleigh number given in equation (1), this stable layer may substantially reduce the internal Rayleigh number for the convection. Data in Schwiderski & Schwab [23], therefore, should be shifted to smaller $R_{\mathrm{I}}^{*}$, and these might become close to the present results.

As mentioned in Introduction, theoretical estimation of variation of cell size by stability analysis contradicts experimental results, thus cell dilatation has never been explained theoretically. Theoretical works assume regular hexagon with descending flow at the center as shape of cell. Cell shape observed in the experiments is hexagon but is quite irregular, thus wavenumber in the fluid layer is not unique. Such irregularity has not been considered in theoretical analysis. Furthermore, a numerical work of internally heated convection [53], which is under progress in a joint research group, shows transition of flow pattern, where spoke-like pattern appears inside the hexagonal cells. In our observation, Figure 3.18, there are lines, which radiate from the center of cell to the cell periphery, which resemble the spoke pattern. At least, flow pattern appearing in the fluid layer is not simple hexagonal cell which has been treated in the linear theory even for smaller Rayleigh number.

## 3.5 Conclusion

In order to confirm the cell dilatation, an experiment that is more closely approximated by the theoretical models was performed. The thermal boundary condition at the bottom plate became nearly adiabatic by using vacuumed glass as the bottom plate, and the non-uniformity of the internal heating was reduced by increasing the height of the fluid layer.

Fluid motion and the temperature field were visualized to estimate the cell dilatation using Kalliroscope and Thermo-chromic Liquid Crystals (TLC) suspension respectively. With the improvements of the experimental setup in the present study, cell dilatation could be observed in digital photographs for each $R_{\mathrm{I}}^{*}$. We conclude, therefore, the dilatation of convection cell with respect to internal Rayleigh number is characteristic of natural convection induced by internal heat generation.

By using the Fourier transform, the wavenumber of the convection cells for each $R_{\mathrm{I}}^{*}$ was calculated from brightness information, extracted from images of the flow obtained using Kalliroscope or TLC for visualization. The cell dilatation could be expressed quantitatively from measurements of the cell wavenumber as a function of internal Rayleigh number. The technique we used to determine the wavenumber removed the subjectivity inherent in the methods used by previous authors. The present results were compared with the results in an earlier study [23] and the influence of the thermal boundary condition at the bottom of the fluid layer on the variation of wavenumber was discussed. We mentioned that a local stable layer with a positive vertical temperature gradient, which is induced by imperfection of thermal insulation at the bottom boundary, reduces the internal Rayleigh number substantially.

As a result of the cell dilatation, an expanded cell breaks up and a smaller cell appears in the expanded cell like double structure as mentioned in Schwiderski & Schwab [23]. Such a structure does not appear in the process of the transition to turbulent flow in standard Rayleigh-Bénard convection, as shown in the phase diagram [36].

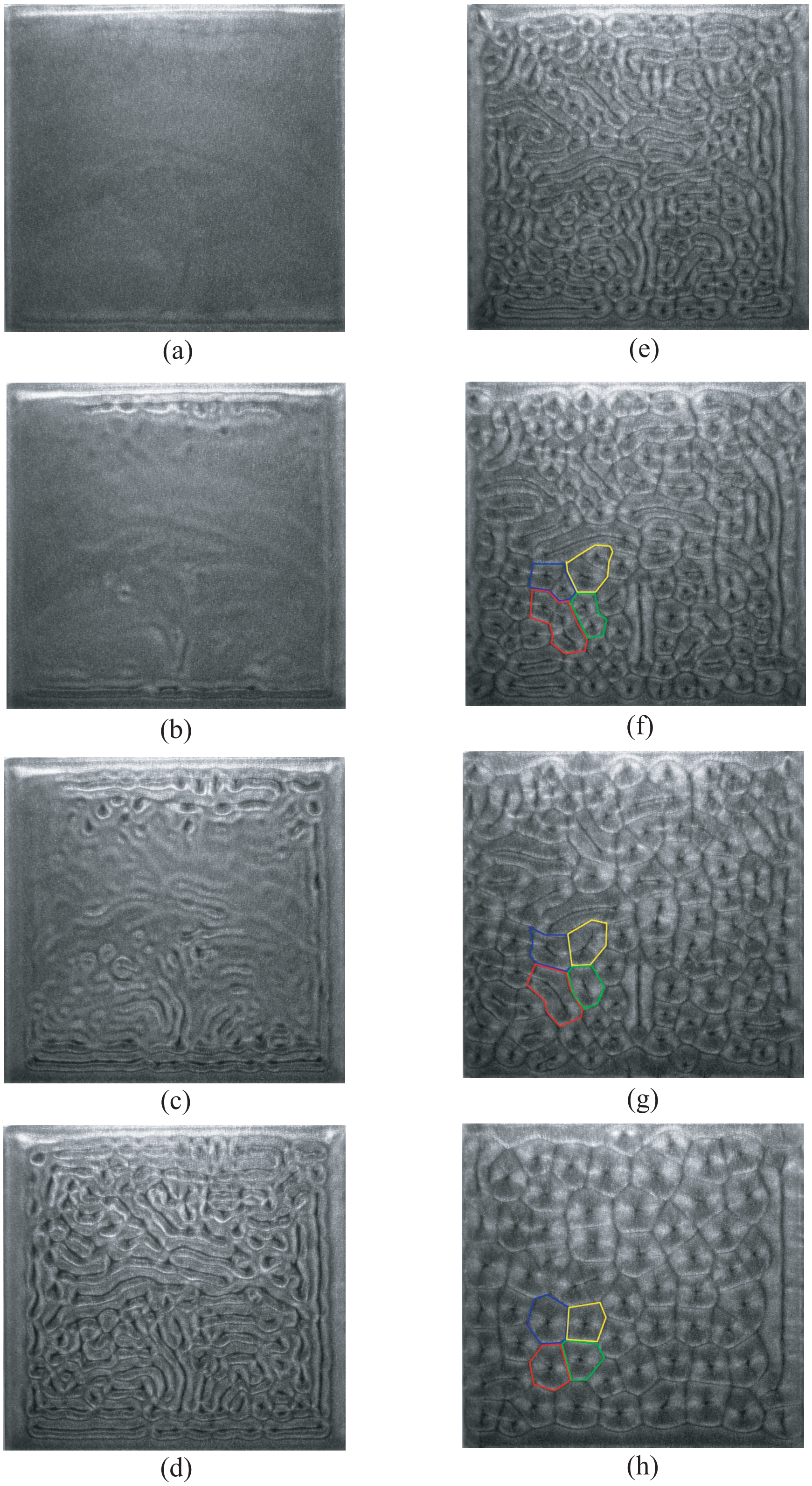

(a) (e) (b) (f) (c) (g) (d) (h)

Figure 3.11: Evolution of convection cells with respect to time. Fringed cells with various color lines in each photograph show the same cell.

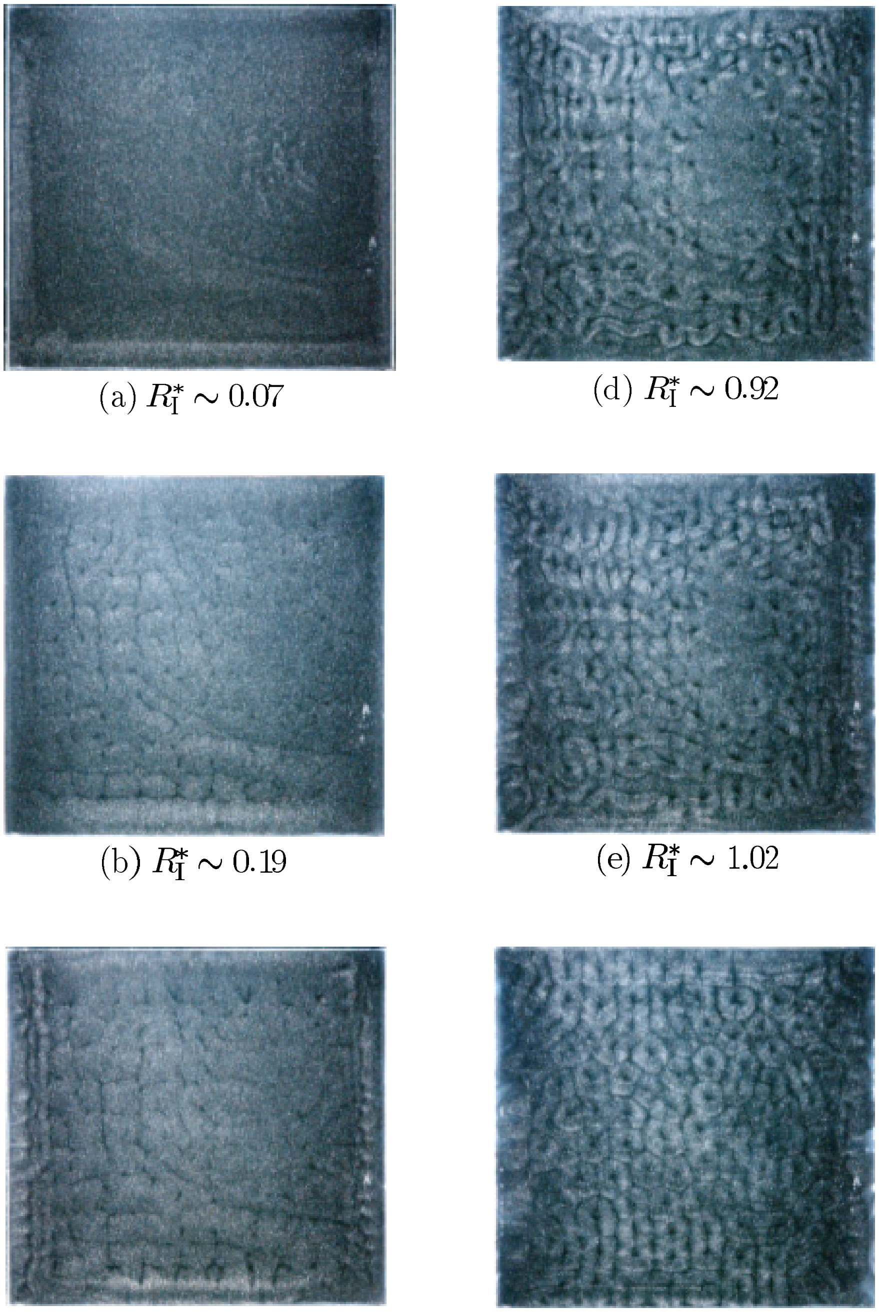

(a) $R_{\mathrm{I}}^{*} \sim 0.07$

(b) $R_{\mathrm{I}}^{*} \sim 0.19$

(c) $R_{\mathrm{I}}^{*} \sim 0.52$

(d) $R_{\mathrm{I}}^{*} \sim 0.92$

(e) $R_{\mathrm{I}}^{*} \sim 1.02$

(f) $R_{\mathrm{I}}^{*} \sim 1.52$

Figure 3.12: Evolution of convection cells in which voltage increases in a phased manner.

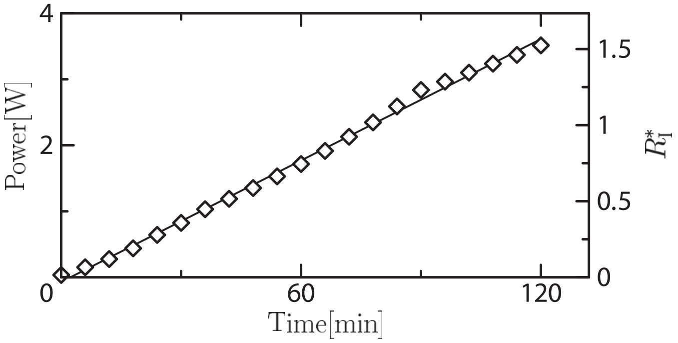

Figure 3.13: Rate of increasing of electric power. Solid line is the approximate linear function.

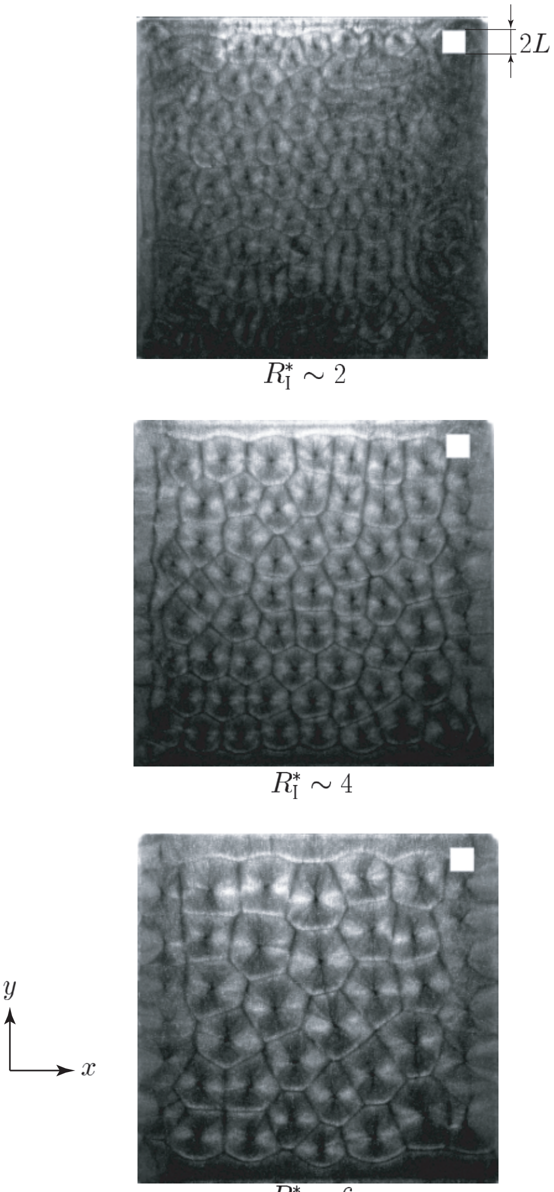

$R_{\mathrm{I}}^{*} \sim 2$

$R_{\mathrm{I}}^{*} \sim 4$

$R_{\mathrm{I}}^{*} \sim 6$

Figure 3.14: Dilatation of convection cell shown in visualized pictures, where white square on photographs are indication of $2L$.

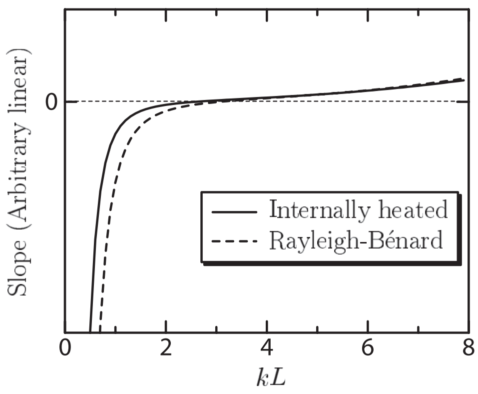

Figure 3.15: Comparison between internally heated convection and Rayleigh-Bénard convection on a slope of the neutral stability curve.

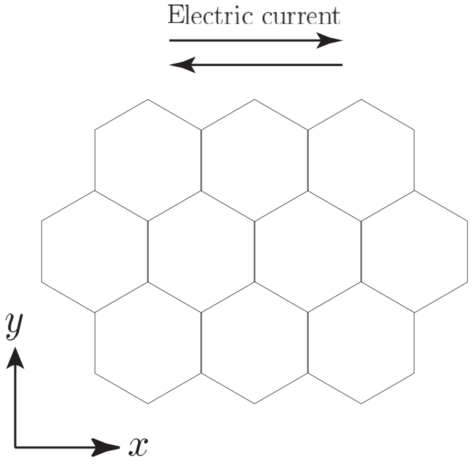

Figure 3.16: Cell arrangement depending on the direction of electric current (Schwiderski & Schwab).

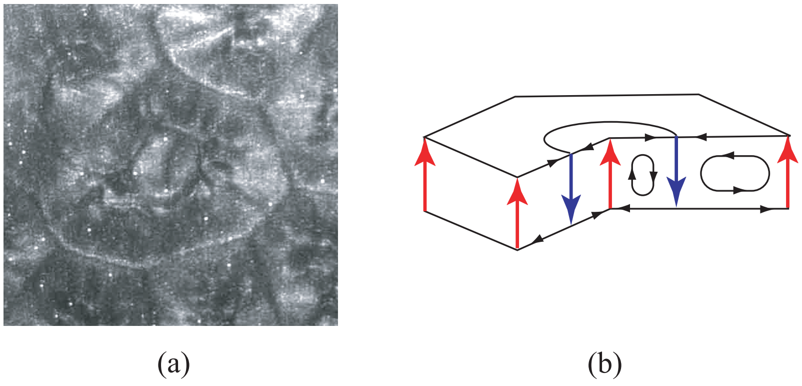
(a)

(b)

Figure 3.17: Double cell structure; (a)Visualized photograph and (b)Schematic illustration of the flow direction in this structure.

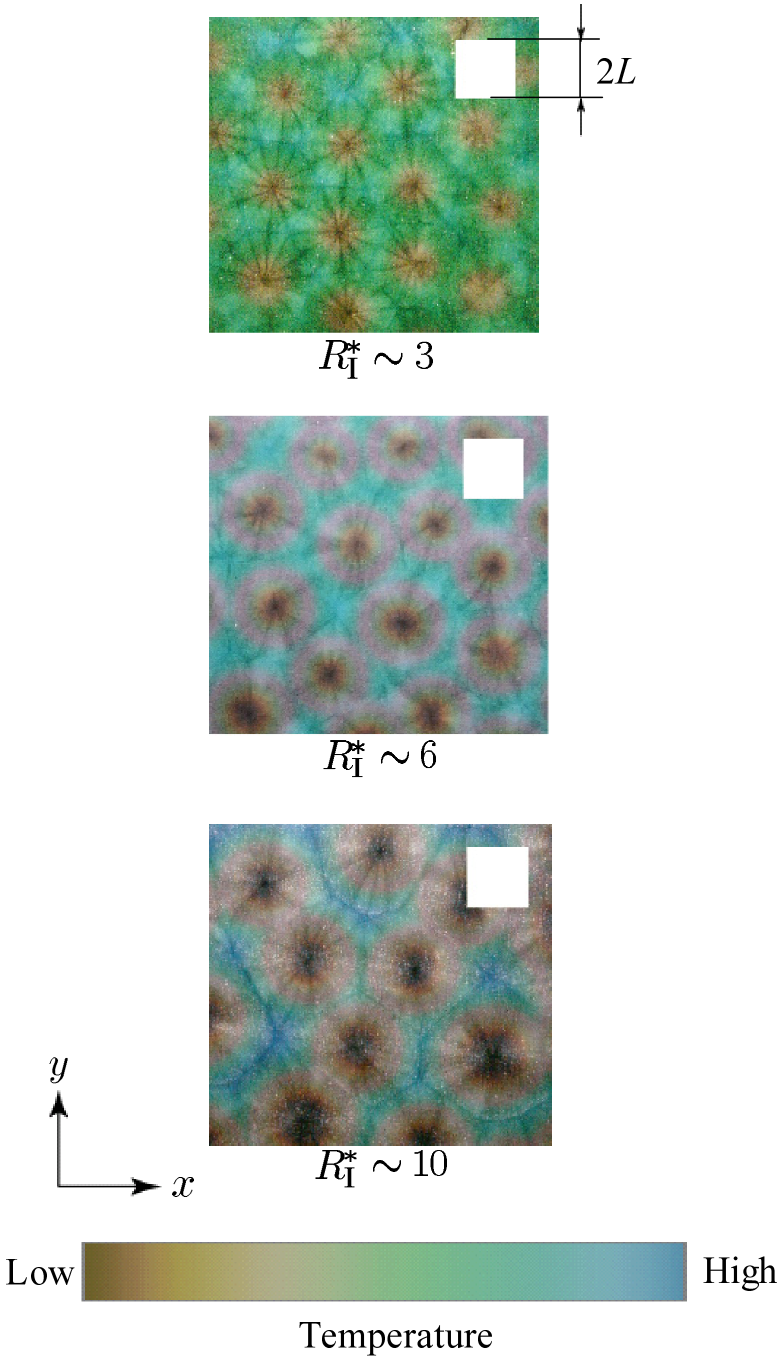

Figure 3.18: Dilatation of convection cell shown in temperature field visualized by TLC, where white square on photographs are indication of $2L$.

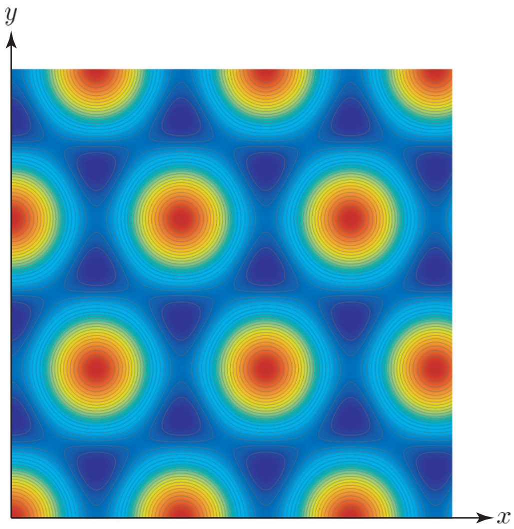

Figure 3.19: Mathematical model of plane form of temperature distribution suggested in Christopherson [42].

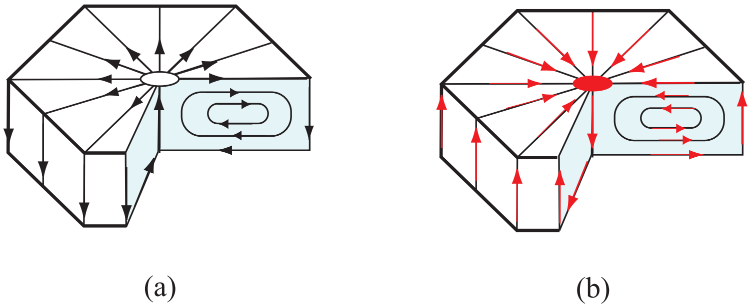
(a)

(b)

Figure 3.20: Flow direction in a convection cell; (a)Bénard convection, (b) Internally heated convection.

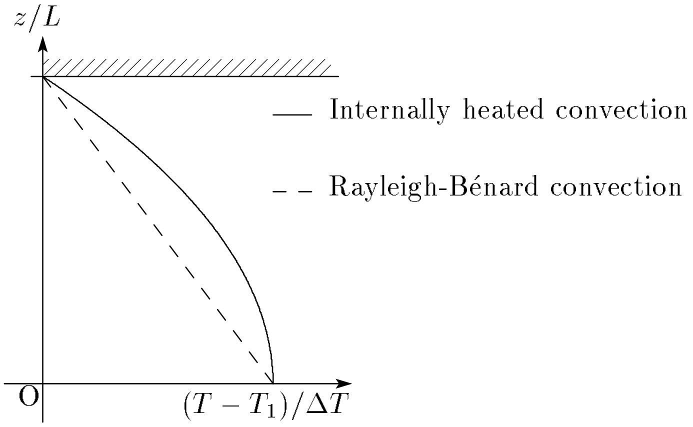

Figure 3.21: Comparison of temperature profile in the conduction state between Rayleigh-Bénard convection and internally heated convection.

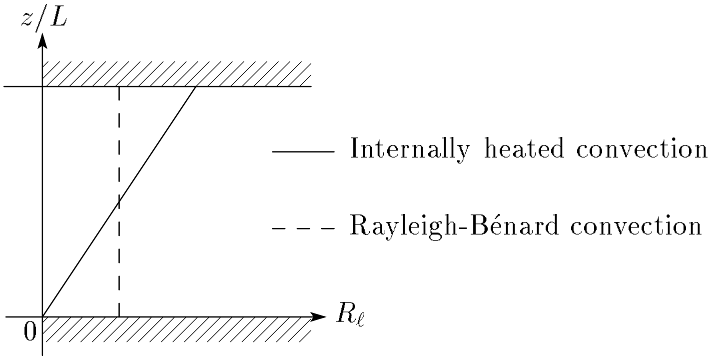

Figure 3.22: Variation of local Rayleigh number $R_\ell$ in Rayleigh-Bénard convection and internally heated convection.

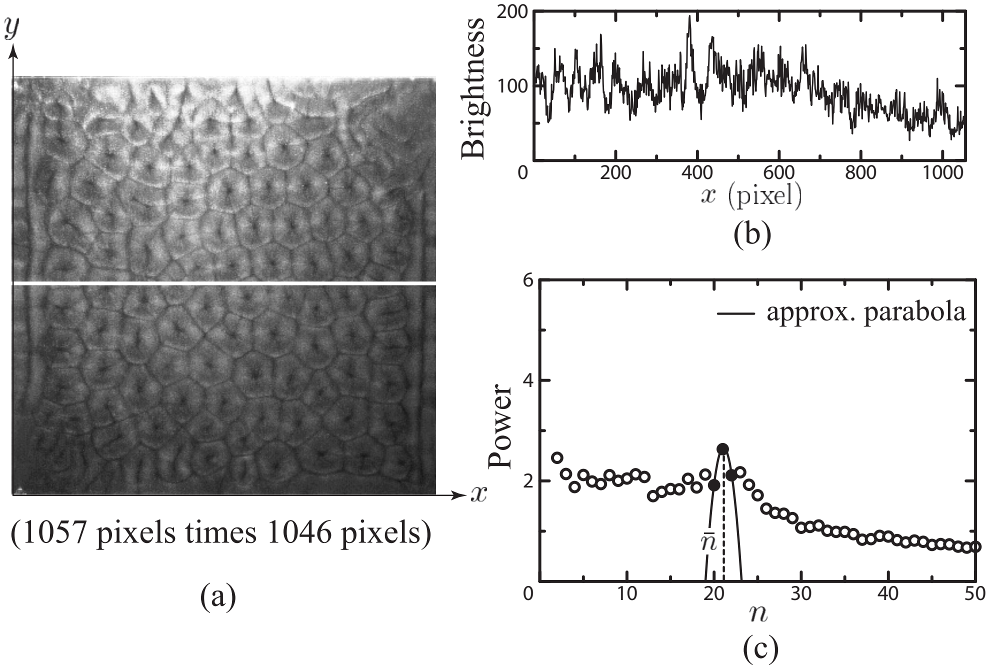

(1057 pixels times 1046 pixels)

(a)

(b)

(c)

Figure 3.23: Periodic fluctuation of brightness information in a visualized picture; (a) visualized picture, (b)brightness information, (c)spectrum of brightness information.

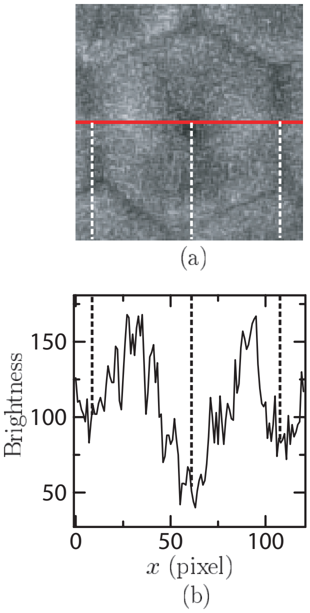

(a)

(b)

Figure 3.24: Brightness information in an image of fluid motion visualized by Kalliroscope; (a) Vizualized picture of one cell, (b) Brightness information across the center of a cell.

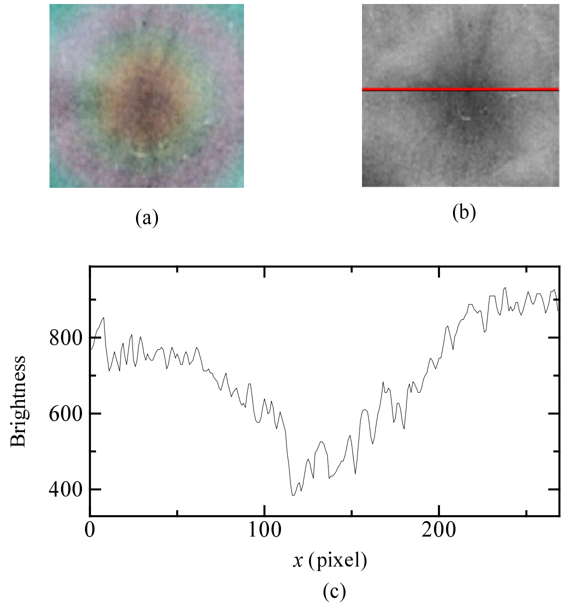

Figure 3.25: Brightness information in an image of temperature field visualized by TLC; (a) Vizualized picture of one cell, (b) Monochrome image, (c) Brightness information across the center of a cell.

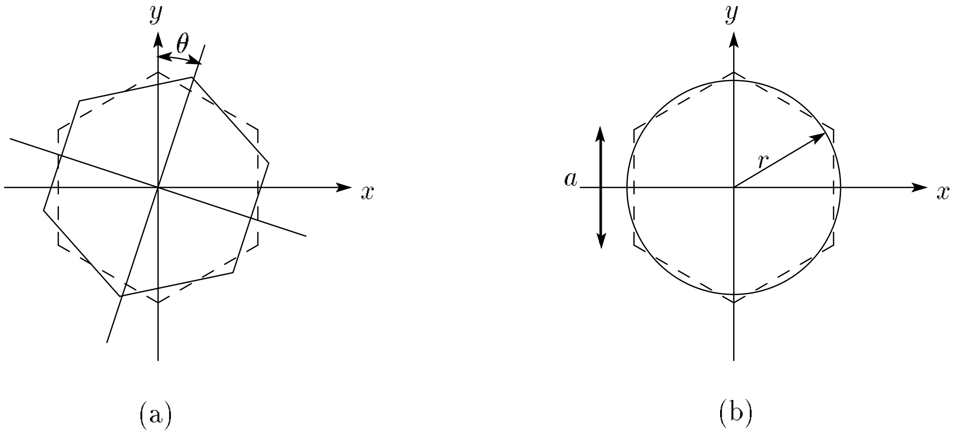

Figure 3.26: Schematic diagrams for the hypothesis on the wavenumber analysis: (a) Slope angle of a hexagonal cell $\theta$ (b) Circle with radious $r$, which has the same area of regular hexagonal cell with side $a$.

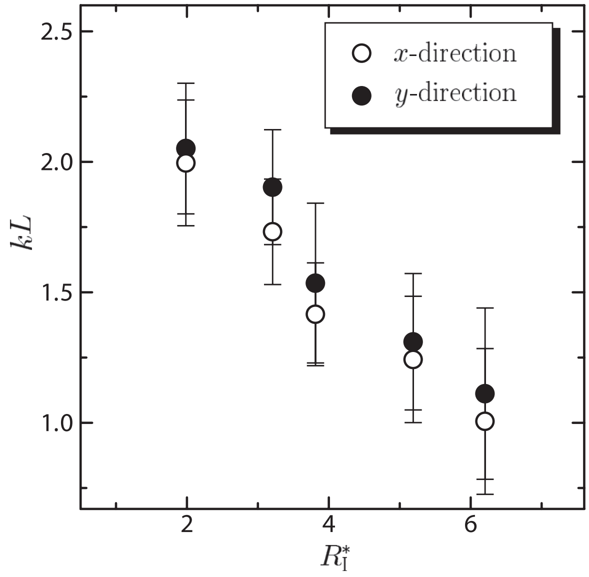

Figure 3.27: Dependence of variation of wavenumber $k$ on the direction of electric current, where the direction of the electric current is the $x$ direction.

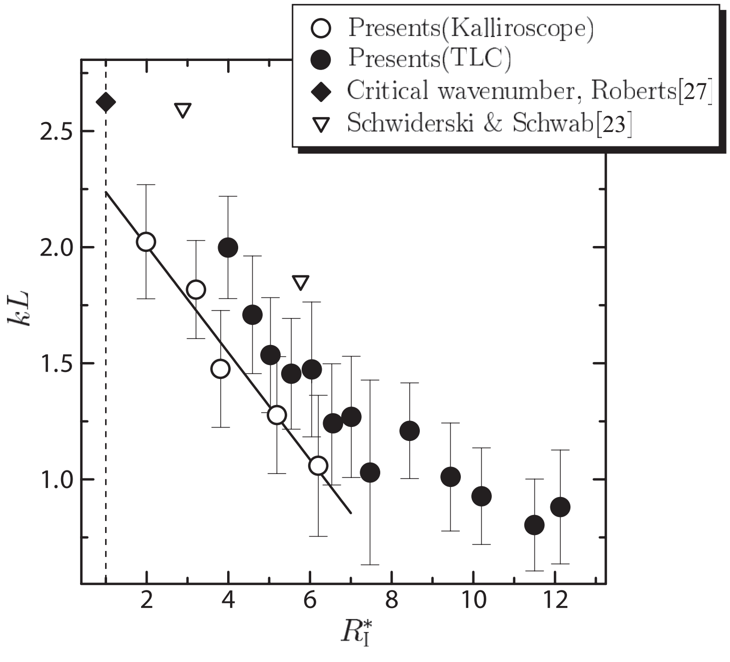

Figure 3.28: Variation of wavenumber $k$ with respect to $R_I^*$.

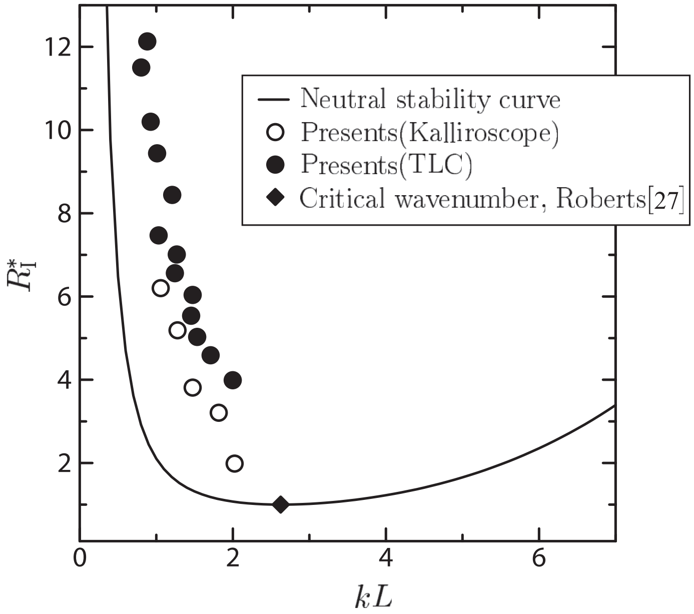

Figure 3.29: Variation of wavenumber $k$ with the neutral stability curve.

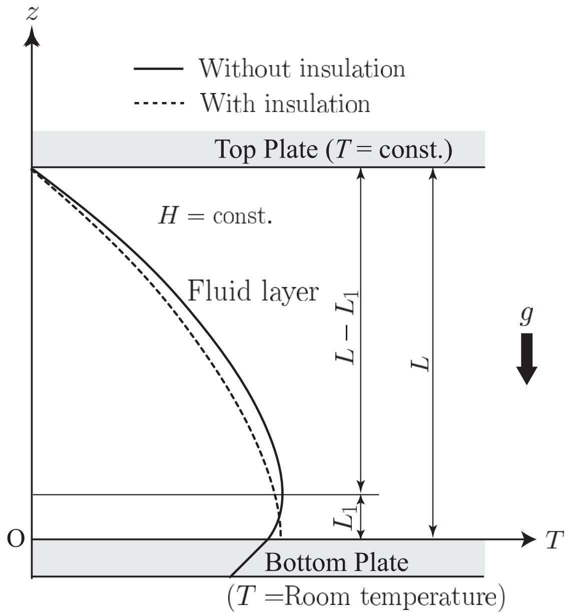

Figure 3.30: Temperature profile with thermal insulation at the bottom and without insulation.

## Chapter 4

# Temperature Behavior in Internally Heated Convection

## Abstract

Temperature behavior in the internally heated convection is quantitatively investigated. Calibration system was developed in order to convert the visualized photographs of temperature field obtained in Chapter 3 to real temperature field. Calibration curve correlating between color information extracted from the photograph and temperature is determined from approximately linear temperature distribution in horizontal fluid layer by hue method. The photographs taken at various internal Rayleigh numbers are converted to temperature field by the obtained curve. A temperature profile in a cell is analyzed by extracting individual cell from a temperature field, and we discuss form of the profile with comparing the profile given by linear theory. Variations of statistical values were determined from the temperature field, and we mention that transition of flow pattern. Critical Rayleigh number was estimated experimentally and it agrees well with theoretically estimated value by linear stability analysis.

## 4.1 Introduction

### 4.1.1 Quantitative investigation of internally heated convection

We reexamined natural convection induced by internal heat generation using new experimental methods and the improved experimental apparatus in Chapter 3. Characteristics of internally heated convection, namely irregular flow pattern, flow direction in a cell, dilatation of a cell etc., were discussed. Almost all of these investigations were performed in qualitative way by using visualized images of flow pattern and temperature field, and then we cannot answer a question, for example, how much irregular. Furthermore, comparison between experimental results and numerical or theoretical results should be discussed quantitatively, and it requires measurement of physical variables such as velocity, temperature and others. In this chapter, we attempted to measure the temperature field in the fluid layer in order to investigate the characteristics of internally heated convection quantitatively.

### 4.1.2 Temperature measurement using TLC

As already mentioned in Chapter 3, TLC, Thermo-chromic Liquid Crystal, is a microcapsule of liquid crystal and has a typical feature that it changes its coloration with respect to temperature. Temperature dependence of the liquid crystal on a reflecting property of light makes such feature. Since it can visualize a temperature field, it has been used to a qualitative investigation of a temperature field. On the contrary, a quantitative investigation by TLC is more difficult, because colors, which express degrees of temperature, strongly depend on an optical system, mainly an angles of an incident light and an observer. Therefore a temperature measurement by TLC requires a well prepared calibration at each measurement apparatus, not only taking a photograph of a visualized temperature field. For example, Ciofalo *et al.* [54] achieved a temperature calibration by using thermally stratified liquid layer, and Dabiri & Gharib [55] also did it by a constant temperature fluid layer in which temperature is set at various degrees. In this chapter, we attempted the calibration by using a horizontal temperature gradient in a horizontal fluid layer at heat conduction in order to quantitatively investigate a temperature field of internally heated convection.

## 4.2 Conversion to temperature

### 4.2.1 General concept of conversion from color to temperature

A microcapsule of TLC mixed in working fluid decomposes an incoming white light into various wave components, which have different wavelength, and scatters them with different angles depending on its temperature. A captured image of the temperature field visualized by TLC is expressed in RGB color system, which has three color components: Red $R$ (wavelength $= 700.0$ nm), Green $G$ (546.1 nm) and Blue $B$ (435.8 nm). RGB system can be converted into HSI system, which also has three components: Hue, Saturation and Intensity. Hue calibration method proposed by Dabiri & Gharib [55] has been widely used for the calibration, where a variation of hue extracted from visualized image is correlated with temperature variation. Two-components method, which uses intensity in addition to hue, is also used as an enhanced calibration method in order to extend a measurable temperature range and to improve the calibration accuracy of the hue method [56]. Full color method, which uses all components in HSI system, is a further enhanced method of the calibration [57, 58]. We choose the standard hue method for the temperature calibration.

Hue is calculated from RGB system directly according to a conversion equation. We calculate it with an intermediate state, XYZ color specification system, in order to confirm a calculation step. RGB system is converted to XYZ system as follows.

$$\begin{aligned} X &= 2.7690R + 1.7517G + 1.1301B, \\ Y &= 1.0000R + 4.5907G + 0.0601B, \\ Z &= 0.0000R + 0.0565G + 5.5928B, \end{aligned} \tag{4.1}$$

where $Z$ component corresponds to intensity. Color information in XYZ system is usually expressed in chromaticity coordinates, where each axis value is determined as a fractional form:

$$\begin{aligned} \bar{X} &= \frac{X}{X+Y+Z}, \\ \bar{Y} &= \frac{Y}{X+Y+Z}, \\ \bar{Z} &= \frac{Z}{X+Y+Z}. \end{aligned} \tag{4.2}$$

Figure 4.1 shows a relationship between RGB, XYZ, HSI and YMCK system, where HSI color space is a cylindrical coordinate representation of the RGB color space and hue is represented as angle on a $\bar{X} - \bar{Y}$ plane.

Figure 4.2 shows a schematic illustration of an apparatus and a visualized photograph of a temperature field in our preliminary experiment of the temperature calibration. A thin plastic case with height 40 mm was filled with a mixture of water and TLC, and it was heated at the top and cooled at the bottom. A white light sheet produced by Halogen lamp by 150 W power (Moritex, model MHF-G150LR) and a cylindrical lens, is emitted to the fluid layer from a side of the case. The fluid layer was thermally stratified to the vertical direction and color changes from red to blue on the vertical direction (Figure 4.2(b)). Color information of the visualized image shown in Figure 4.2(b) is expressed in a chromaticity diagram as Figure 4.3, where intensity information is compressed. As a preceding explanation of the relationship between XYZ and HSI system, hue is determined as an angle from a reference point in the $\bar{X} - \bar{Y}$ plane. When a point $(\bar{X}, \bar{Y}) = (0.32, 0.335)$ is chosen as a reference point, we can take a relationship between height of the image and hue (Figure 4.4). If we can determine a temperature at each height, this relation would give us a calibration curve between hue and temperature.

### 4.2.2 Apparatus for temperature calibration

As mentioned in Introduction, coloration of TLC depends on an angle of incident light and an angle of observer (i.e. Camera). It is required that the temperature calibration is performed in the same optical configuration as the actual measurement. The configuration in this study explained in Section 3.3 consists of a shallow fluid layer, incident light sheet from the side of the fluid layer, a mirror located at the bottom of the fluid layer with 45 ° angle from horizon and a digital camera. We attempted temperature calibration by using a horizontal temperature gradient developed in such configuration.

Figure 4.5 shows a schematic illustration of the experimental setup for the calibration; (a) Front view and (b) Top view of the apparatus, and Figure 4.6 is a photograph of an overview of the apparatus. The fluid layer has 220 mm times 210 mm horizontal cross section and 7 mm height. Working fluid is a mixture of distilled water and TLC, which has measurable temperature range from 20 to 30 °C. The layer is sandwiched by two vacuumed glass plates at the top and the bottom for thermal insulation, where the bottom plate is transparent and the top plate is made opaque by black painting. Water tanks located at the both sides of the fluid layer contact to the fluid with thin copper plate. Flowing water in the tanks circulates through a thermostatic bath and achieves isothermal boundary with high accuracy at the both sides of the fluid layer. Light sheet was emitted in the middle height of the fluid layer through a Plexiglas lateral wall of 10 mm thickness. Visualized temperature field was taken from the bottom through the transparent vacuumed glass by a digital camera [1].

### 4.2.3 Calibration curve

Setting temperatures of the cooling water and heating water are $T_{\mathrm{L}} = 22$ and $T_{\mathrm{H}} = 28$ °C respectively. In this condition, there is no convective motion in the fluid layer and thus it is in a thermal conduction state, i.e. a temperature variation on the horizontal direction $x$ is approximately liner from 21 to 28 °C. Figure 4.7(a) shows a visualized temperature field taken by a digital camera. Constant temperature line, which expresses the same color, curves near the front and the back wall of the fluid layer. It may be an influence of the boundary condition at the Plexiglas walls and then we remove such curved part by trimming the photograph (Figure 4.7(b)).

According to the conversion relation of the color system expressed in Equation (4.1) and (4.2), also in Figure 4.1, color information on RGB system extracted from the visualized photograph is converted to XYZ color specification system. Figure 4.8 shows a chromaticity diagram in which color information without brightness (or $Z$ component) is expressed as a pint on the $\bar{X} - \bar{Y}$ plane, where extracted color information is averaged for the $y$ direction before the conversion. Red arrows in the figure represent increase of temperature and these curves intersect at the lower temperature region. This intersection is caused by removing brightness information. As is already mentioned, hue is determined as an angle on the $\bar{X} - \bar{Y}$ plane. In a case labeled with A in the figure, there is one-to-one correspondence between hue and temperature. In case B, however, these are multipoint, which have the same value of hue on the plane, and then temperature is underspecified by hue if we calibrate this region. This complex region, however, has only a narrow range of the temperature, which is approximately 21 to 22 °C. Thus we abandoned this region and performed the calibration only on a left side from a broken line shown in the figure. In addition, a reference point on the $\bar{X} - \bar{Y}$ plane to

---

[1] Details of the optical system were explained in Section 3.3.1, Experimental apparatus, and in Section 3.3.3, Visualization.

determine hue is chosen as $(\bar{X}, \bar{Y}) = (0.32, 0.32)$.

A relationship between temperature and hue is determined by the approximated linear variation of temperature on the horizontal direction in the fluid layer (Figure 4.9), where usable temperature range for the calibration is 22 to 28 °C. The variation of temperature with respect to hue clearly changes its tendency at a boundary, hue $\sim$ 190, and we used two approximated curves to separated regions labeled A and B in the figure. Approximated curves are fourth power function of hue and are represented as

$$\begin{aligned} T &= 23.973 - 0.090063\mathrm{Hue} + 0.0014741\mathrm{Hue}^2 \\ &\quad - 9.6568 \times 10^{-6}\mathrm{Hue}^3 + 2.3019 \times 10^{-8}\mathrm{Hue}^4, \quad \text{for} \;\; 50 \leq \mathrm{Hue} \leq 182, \qquad (4.3) \\ T &= 112.79 - 3.0072\mathrm{Hue} + 0.028352\mathrm{Hue}^2 \\ &\quad - 0.00010438\mathrm{Hue}^3 + 1.3459 \times 10^{-7}\mathrm{Hue}^4, \quad \text{for} \;\; 182 < \mathrm{Hue} \leq 250. \qquad (4.4) \end{aligned}$$

In order to reduce error on the temperature conversion by using this calibration curve, we exclude data which is out of a range of $Y$.

### 4.2.4 Result of the conversion

In order to confirm a validity of the temperature conversion, a visualized photograph as shown in Figure 4.7(b) is converted to the temperature. Figure 4.10 shows a comparison between the converted temperature profile, which is obtained by averaging the converted profile for the $y$ direction, and the approximated linear profile of the temperature. These profiles agrees well and standard deviation of a scatter from the approximated linear function is 0.253 °C. This value would gove degree of error in this temperature conversion. Figure 4.11 shows a result of the temperature conversion for a visualized temperature field in the convection layer; (a) Visualized photograph at $R \sim 4.0$ and (b) Converted temperature field. Convection cells are more clearly revealed in the temperature field.

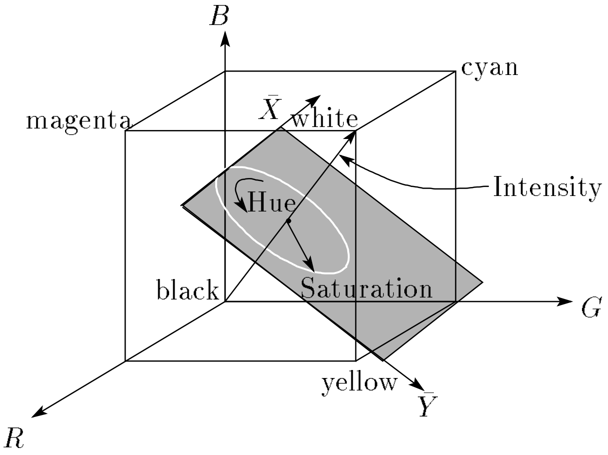

Figure 4.1: Schematic diagram of a relationship between RGB, XYZ, HSI and YMCK (yellow, magenta, cyan, black) system, where HSI color space is a cylindrical coordinate representation of the RGB color space.

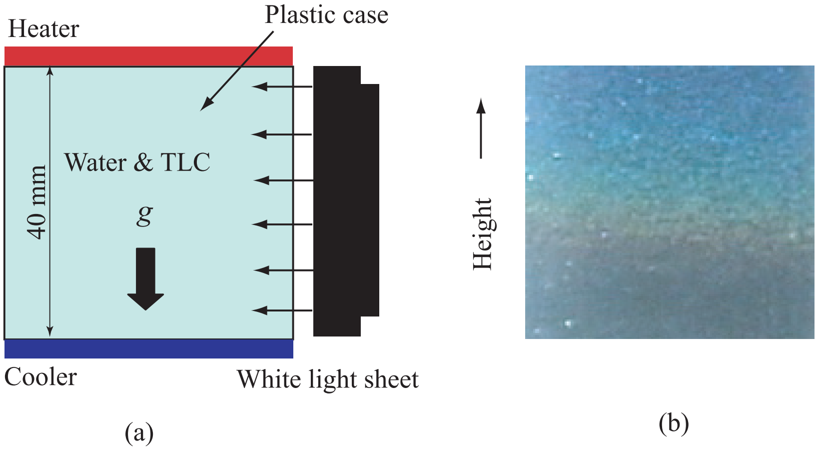

Figure 4.2: Trial experiment of the temperature calibration (a) Schematic sketch of experimental setup (b) Visualized photograph of a temperature field.

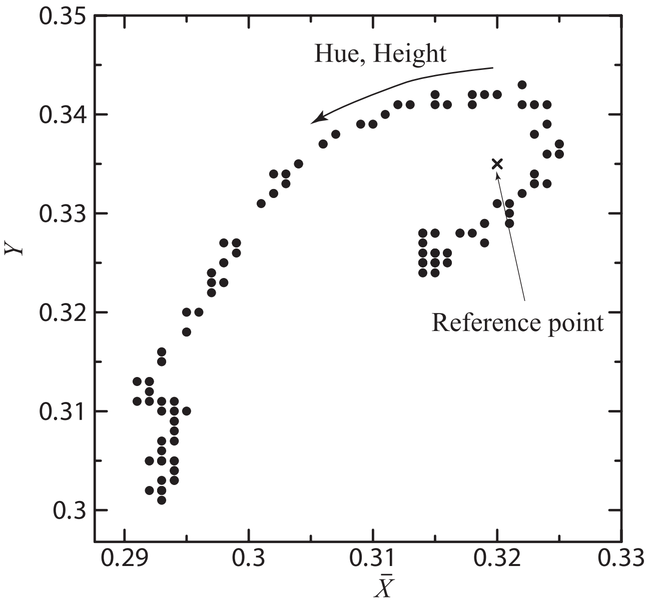

Figure 4.3: Color information of the visualized image expressed on chromaticity diagram of XYZ color specification system.

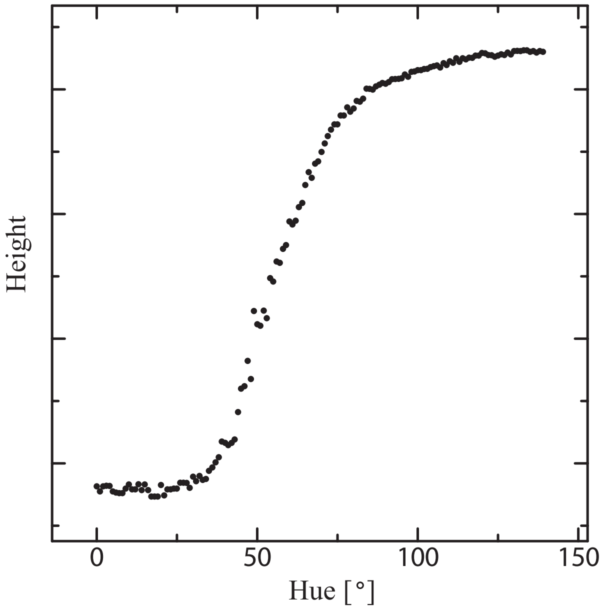

Figure 4.4: Relationship between height of the visualized image and hue.

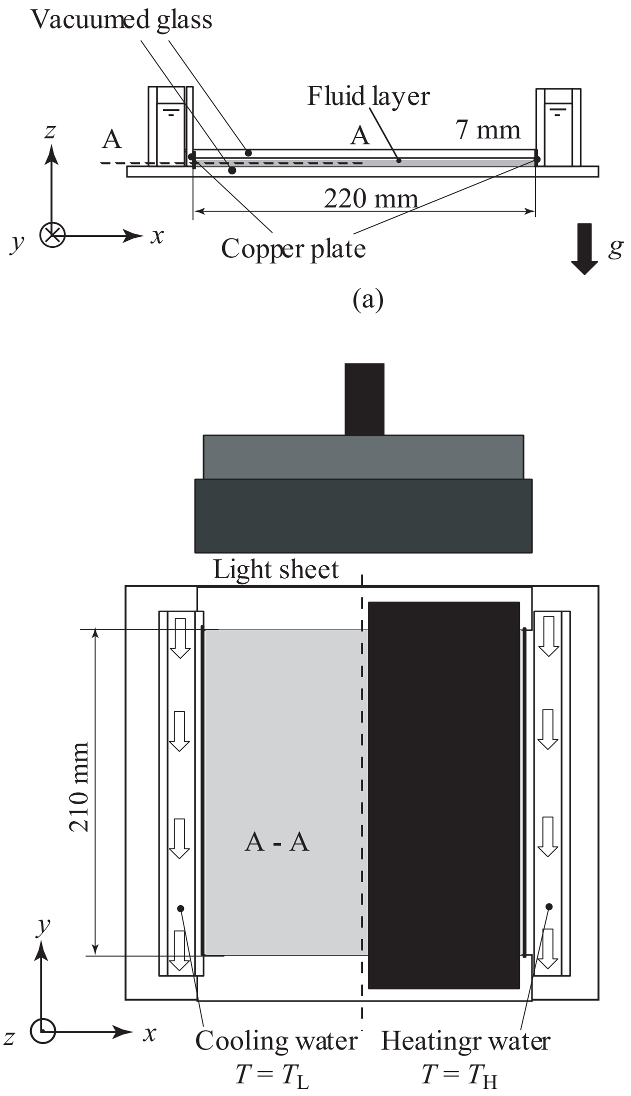

(a)

(b)

Figure 4.5: Schematic illustration of the experimental setup for the temperature calibration; (a) Front view and (b) Top view of the apparatus, where cooling water with temperature $T = T_{\mathrm{L}}$ and heating water with $T = T_{\mathrm{H}}$ circulate a left side and a right side water tank.

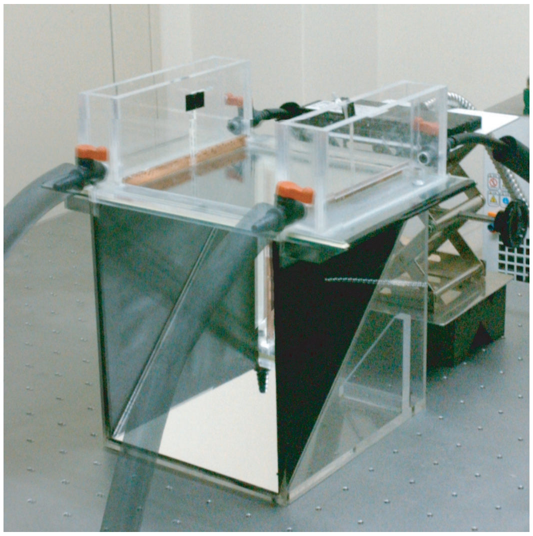

Figure 4.6: Photograph of overview of the experimental setup for the temperature calibration.

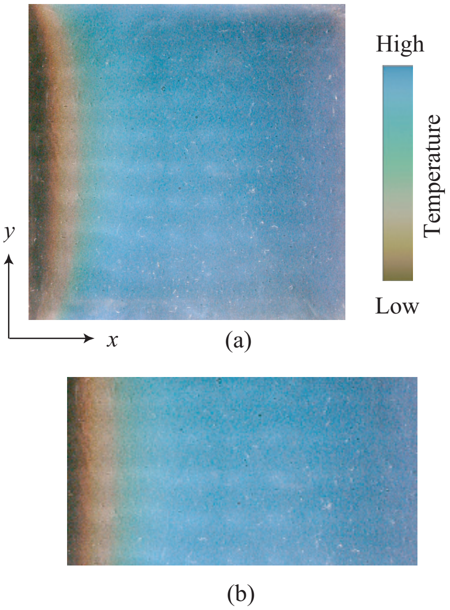

Figure 4.7: Photographs of visualized temperature field, which has a liner temperature gradient. (a) Full field and (b) Trimmed image.

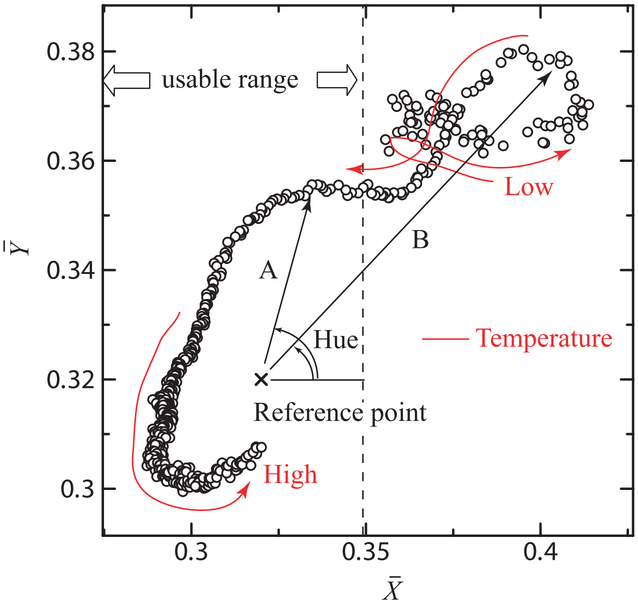

Figure 4.8: Color information of the visualized photograph taken in the calibration system expressed on a chromaticity diagram of XYZ color specification system.

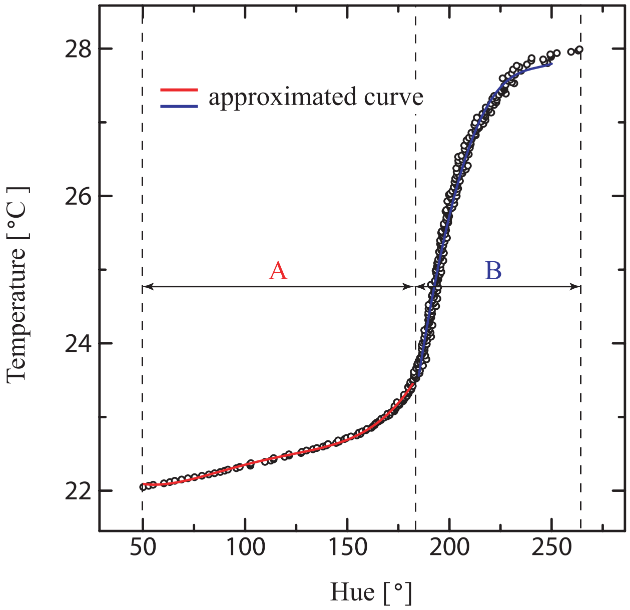

Figure 4.9: Calibration curve between temperature and hue, where a usable temperature range is 22 to 28 °C, where approximated curves are determined by each region, A or B.

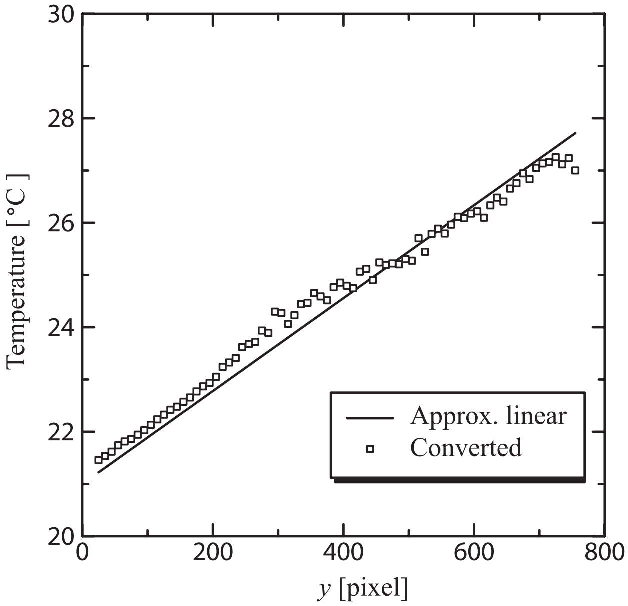

Figure 4.10: Comparison between a converted temperature profile by the calibration curve and the approximated linear profile, where the converted temperature is drawn at interval of 10 points for clear viewing.

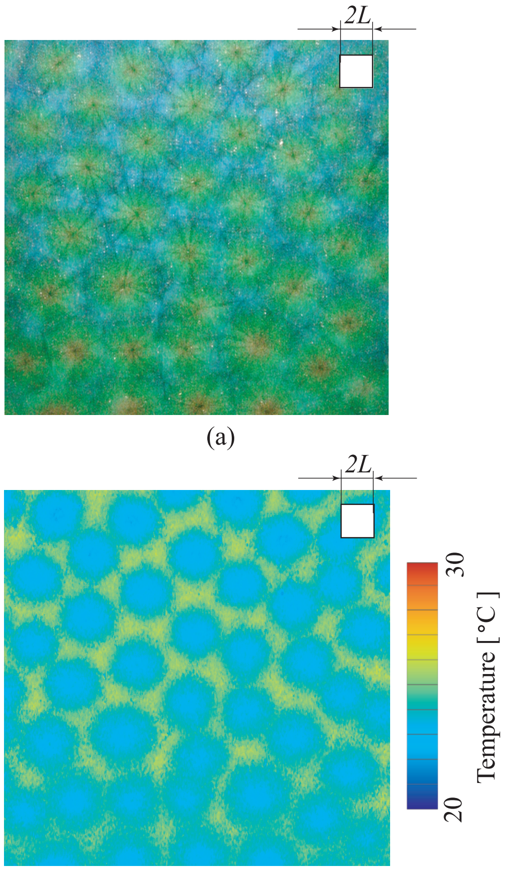

(a)

(b)

Figure 4.11: Result of the temperature conversion for a visualized temperature field in the convection layer; (a) Visualized photograph at $R_{\mathrm{I}}^{*} \sim 4.0$ and (b) Converted temperature field.

## 4.3 Results and discussions

### 4.3.1 Extraction of indivisual cells

We attempted to extract individual cells from the converted temperature field in order to investigate size and shape of the cells. The extraction was performed according to a following process.

(A) Determining the center of each cell

(B) Determining number of the apexes $N$ at each cell

(C) Providing a temporary position of the apexes $A'_N$

(D) Determining the position of the apexes $A_N$

(E) Repeating above process overall the temperature field

(A) Temperature distributes concentrically near the center of a cell as shown in Figure 3.18 and also in Figure 4.11. Figure 4.12(a) is a part of a converted temperature field and Figure 4.12(b) shows its binarized temperature field. Black pixels, which represent lower temperature, are distributed circularly, and the center of a black part, which is given by first moment of a black pixel, would correspond to the center of cell. Black points in Figure 4.12(a) represent the determined center of cells by this method.

(B) Almost all cells are hexagonal and have six apexes. In order to confirm the number of apexes $N$, we extract a temperature profile on a circumference at a middle position between the centers of neighboring two cells as shown in Figure 4.13(a). Figure 4.13(b) shows an example of an extracted temperature profile, where the horizontal axis represents angle from 0 to 360. The profile has six periods, i.e. the cell has six apexes.

(C) We assume that the apexes of a cell exist near a boundary, which is determined as perpendicular bisector of a line segment between centers of neighboring two cells. Some temporary positions of each apex $A'_N$ are provided near the line.

(D) One of the temporary positions is chosen as the position of an apex $A_N$ as follows. Temperature becomes maximum at the boundary of cells, and temperature on a line between apexes also has the maximum. The apexes are determined in order that a line segment made by two apexes has the maximal average temperature.

(E) Above process is applied for every apex and for every cell in the field, and then we can determine and separate cells as shown in Figure 4.14.

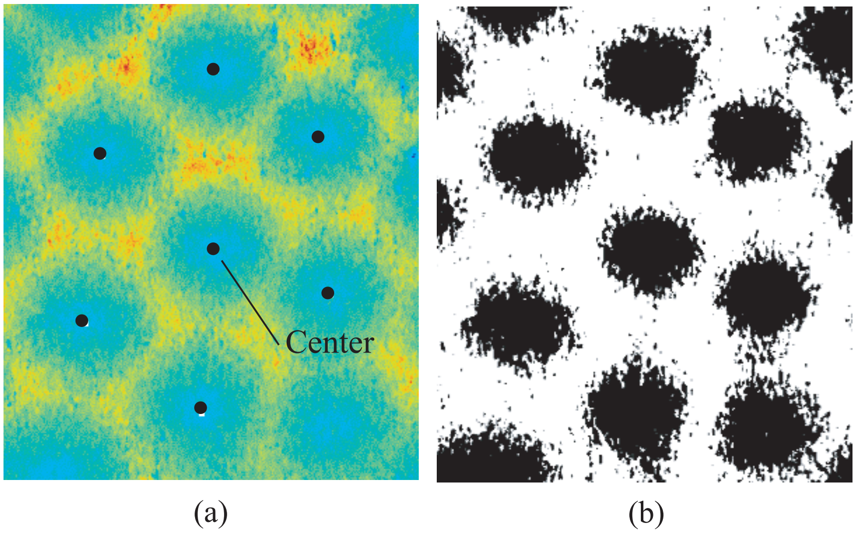

(a) (b)

Figure 4.12: (a) Converted temperature field and (b) its binarized temperature field, where black points in Figure (a) represent the center of cell determined as the center of a circular part in the binarized temperature field.

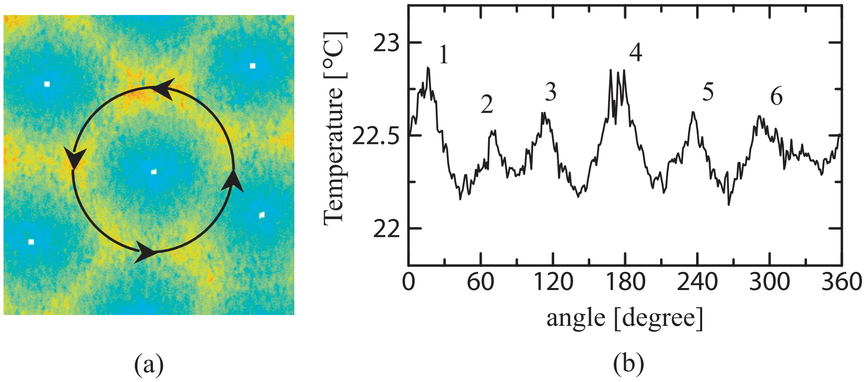

(a) (b)

Figure 4.13: Temperature profile on a circumference written in Figure (a), where a position of the circumference is a halfway between the centers of neighboring two cells.

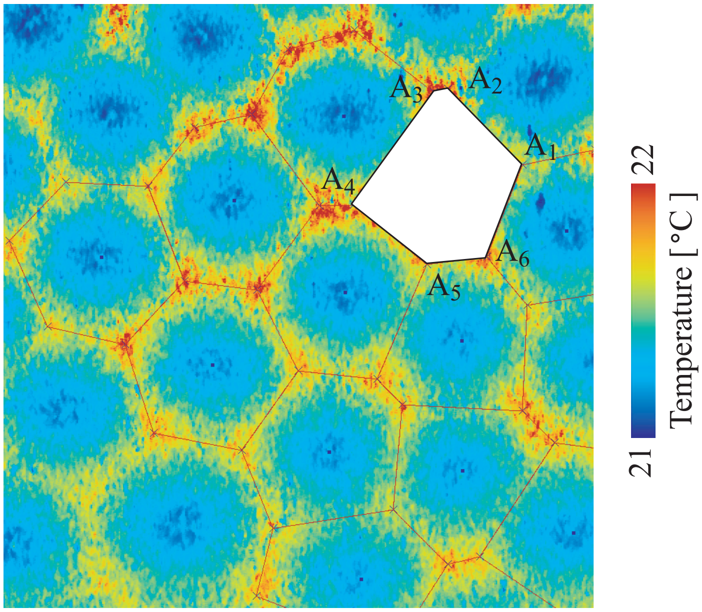

Figure 4.14: Separated cells on a temperature field, where red lines represent boundaries of cells.

### 4.3.2 Size and shape of cell

As already mentioned in Chapter 3, convection cell appearing in internally heated convection expands with respect to internal Rayleigh number, $R_{\mathrm{I}}$. Furthermore, unlike in the case of Bénard and Rayleigh-Bénard convection, shape of the cells is irregular and size of the cells deviates. We investigate these phenomena quantitatively by analyzing an extracted temperature distribution at each cell.

Figure 4.15 shows a variation of the area of a cell $S$ with respect to reduced internal Rayleigh number, $R_{\mathrm{I}}^*$, on a double logarithmic plot. $S$ is an average area of all cell on the temperature field, and error bars in the figure represent standard deviation of $S$. The area of a cell increases monotonically with respect to $R_{\mathrm{I}}^*$, however, slope of the variation changes at $R_{\mathrm{I}}^* \sim 5$. By a least square approximation, $S$ is proportional to ${R_{\mathrm{I}}^*}^{0.68}$ for a range of $0 \leq R_{\mathrm{I}}^* \leq 5$ and to ${R_{\mathrm{I}}^*}^{1.02}$ for $R_{\mathrm{I}}^* > 5$. This change of the slope may be caused by transition of flow pattern, which was discussed in Chapter 3, however, such flow transition is not clearly visible in the temperature field. Deviation of the area of a cell is in the same order of magnitude at every $R_{\mathrm{I}}^*$, and there is no typical variation of the deviation with respect to $R_{\mathrm{I}}^*$. Convection cell appearing in internally heated convection has deviation of the area of cell just after the onset of convection, and magnitude of the deviation does not vary with increasing $R_{\mathrm{I}}^*$.

Since positions of the center of the cells are already known, we define irregularity of hexagonal cell by using gap from an equivalent circle, which has the center at the same position of the cell and has the same area. Figure 4.16 represents the definition of the irregularity, where $\Gamma$ and $\ell$ represent radius of the equivalent circle and distance from the center to the periphery at an angle $\theta$. Gap between hexagonal cell and an equivalent circle is defined as

$$\Lambda = \frac{1}{S} \int_0^{2\pi} [\ell(\theta) - \Gamma]^2 \, d\theta, \tag{4.5}$$

where $S$ is an area of a cell. If cell shape is regular of hexagon, it becomes $\Lambda_{\mathrm{RH}} \sim 0.2$. Irregularity of the cells, $IR$, is expressed as normalized $\Lambda$ by $\Lambda_{\mathrm{RH}}$,

$$IR = \Lambda / \Lambda_{\mathrm{RH}}. \tag{4.6}$$

Figure 4.17 shows variation of $IR$ with respect to $R_{\mathrm{I}}^*$, where a broken line represents regular hexagon, $IR = 1$. We expected that convection cell at onset of convection is nearly regular and then irregularity increases with respect to $R_{\mathrm{I}}^*$. However, it was found that $IR$ has no typical variation at smaller $R_\mathrm{I}^*$, $R_\mathrm{I}^* < 10$, and convection cell is irregular although near the onset of convection. At higher $R_\mathrm{I}^*$, the side boundary of the fluid layer affects the shape of convection cell as shown in visualized images, and then $IR$ is slightly larger than that for smaller $R_\mathrm{I}^*$.

### 4.3.3 Statistics of horizontal temperature field

Temperature is uniform on the horizontal cross section of the fluid layer at the thermal conduction state and distributes horizontally at the convection state by formation of convection cells. The distribution of temperature may vary with growing of convection cell. We investigated the variation by analyzing horizontal temperature field statistically. Figure 4.18 shows variation of standard deviation of temperature $T_\mathrm{rms}$ determined from overall temperature field. This value expresses intensity of temperature distribution and is defined as

$$T_\mathrm{rms} = \left[ \left\langle (T - \bar{T})^2 \right\rangle_{xy} \right]^{1/2}, \quad \bar{T} = \langle T(x,y) \rangle, \tag{4.7}$$

where operator $<>_{xy}$ represents horizontal average. We found that $T_\mathrm{rms}$ is roughly proportional to $R_\mathrm{I}^*$ until $R_\mathrm{I}^* \sim 4$. Subsequently it increases substantially with respect to $R_\mathrm{I}^*$. This variation may have a transition point as well as the variation of the area of convection cell versus $R_\mathrm{I}^*$ shown in Figure 4.15. Possible reason of occurring such transition is a transition of flow pattern. This transition may not be similar to the transition appearing in Rayleigh-Bénard convection, for example, changing shape of a periphery of the cell or being time dependent. Thus the transition does not appearing clearly in the converted temperature field.

Hexagonal cell given by a linear theory has the highest temperature at the apexes and the lowest temperature at the center (Figure 4.19). Temperature varies gradually between the center and the apex. We compare temperature profile extracted from the converted temperature field and the theoretical one in Figure 4.19, which shows temperature profiles from the center to the apex of a cell at each $R_\mathrm{I}^*$. The horizontal axis represents distance from the center, $r$, normalized by distance between the center and the apex, $R_\mathrm{apex}$ (see Figure 4.19). The vertical axis shows temperature normalized by mean temperature in a cell, $T_\mathrm{m}$, and then zero corresponds mean temperature. The profiles in the figure are determined by average of profiles of all cells existing on the temperature field. Red line represents a theoretical profile given by linear theory. Temperature of the theoretical profile increases gradually from the center to the apex. In comparison with this, the measured profiles shows gradual temperature increase near the center, but a sharp increase at $r/R_{\mathrm{apex}} \sim 0.65$. Furthermore, there is large difference on a deviation of temperature from $T_{\mathrm{m}}$ at the center ($T_{\mathrm{center}}$) or at the apex ($T_{\mathrm{apex}}$). At the theoretical profile, the deviation at the center is larger than at the apex, namely $|T_{\mathrm{center}} - T_{\mathrm{m}}| < |T_{\mathrm{apex}} - T_{\mathrm{m}}|$, however such relation is reversed at present profiles, namely $|T_{\mathrm{center}} - T_{\mathrm{m}}| > |T_{\mathrm{apex}} - T_{\mathrm{m}}|$. A position at which temperature equals means temperature from the center is slightly further than the theoretical profile. These tendencies become more clear with increase of $R_{\mathrm{I}}^{*}$. They suggest that descending flow induced by separation of thermal boundary layer near the cooling plate exists comparatively wide range in a cell and ascending flow, which has higher temperature, is localized near the apexes.

We attempted to estimate a critical Rayleigh number on internally heated convection experimentally. Temperature difference between the center and the apexes, $\Delta T_{\mathrm{cell}}$ increases with respect to $R_{\mathrm{I}}^{*}$ and is zero at the onset of convection. Figure 4.21 shows a variation of $\Delta T_{\mathrm{cell}}$ versus $R_{\mathrm{I}}^{*1/2}$. At small $R_{\mathrm{I}}^{*}$, $\Delta T_{\mathrm{cell}}$ is proportional to $R_{\mathrm{I}}^{*1/2}$, and approximated linear function drawn in the figure as a solid line intersects with the horizontal axis at $R_{\mathrm{I}}^{*} = 1.050$, which has deviation $\pm 0.208$. $R_{\mathrm{I}}^{*}$ is a reduced internal Rayleigh number defined as $R_{\mathrm{I}}^{*} = R_{\mathrm{I}}/R_{\mathrm{c}}$, where $R_{\mathrm{c}}$ is critical Rayleigh number calculated by linear stability analysis, and then $R_{\mathrm{I}}^{*} = 1$ represents the onset of convection. Therefore we conclude that the experimentally estimated critical Rayleigh number agrees well with theoretical one.

## 4.4 Conclusion

In order to investigate natural convection induced by internal heat generation quantitatively, measurement of temperature field in the fluid layer was performed using TLC, Thermochromic Liquid Crystal. Calibration system was developed in order to convert color information extracted from visualized images to temperature field by taking a picture of a horizontal temperature gradient in the shallow fluid layer. Calibration curve between a Hue that is one of color information component on HSI color system and a temperature was determined as a function of Hue to fourth power, and every visualized image taken at each internal Rayleigh number was converted to temperature field. There is only small error in the temperature conversion.

Individual cells on the horizontal temperature field were extracted based on some assumptions. Variation of the area of cells, which is determined from extracted cells, with respect to reduced internal Rayleigh number, $R_{\mathrm{I}}^{*}$ were shown. We determined the slope of the variation and showed that the slope changes at $R_{\mathrm{I}}^{*} \sim 5$. Variation of deviation of the area versus $R_{\mathrm{I}}^{*}$ was also investigated and there is no typical variation. Irregularity of hexagonal cell was defined by using a deformation from equivalent circle of cell, and variation of irregularity versus $R_{\mathrm{I}}^{*}$ was shown. There are also no typical variation as well as variation of deviation of the area. We concluded that convection cell appearing in internally heated convection is initially irregular at onset of convection. Standard deviation of temperature determined from overall temperature field changes a slope of its variation with respect to $R_{\mathrm{I}}^{*}$ at $R_{\mathrm{I}}^{*} \sim 4$ as well as variation of area of cell. We discussed that there is transition point at this Rayleigh number and it may be induced by transition of the flow pattern. Temperature profile from the center to the apex of the cell extracted from converted temperature field was compared with the profile given by liner theory. As the results, we found that descending flow exists in a cell with comparably wide area and ascending flow bringing up high temperature fluid is localized near the apexes of cell. Critical Rayleigh number was determined experimentally by variation of temperature difference between the center and the apex of the cell, and it agrees well with theoretical value estimated by linear stability analysis.

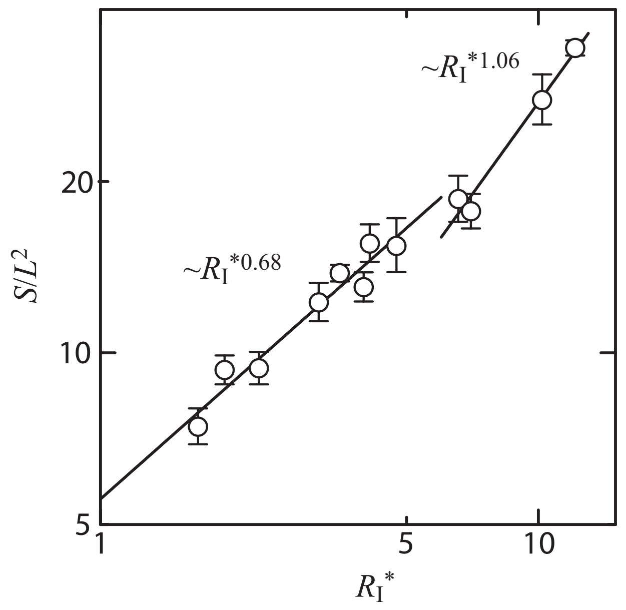

Figure 4.15: Variations of area of cell $S$ and its deviation versus $R_{\rm I}$, where solid line shows approximated curve determined by least square at each range, $0 \leq R_{\rm I}^* \leq 5$ and $R_{\rm I} > 5$.

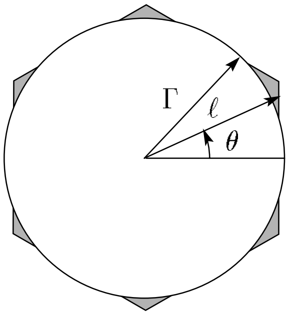

Figure 4.16: Hexagonal cell and equivalent circle, where $\Gamma$ and $\ell$ represent radius of the equivalent circle and distance from the center to the periphery at an angle $\theta$.

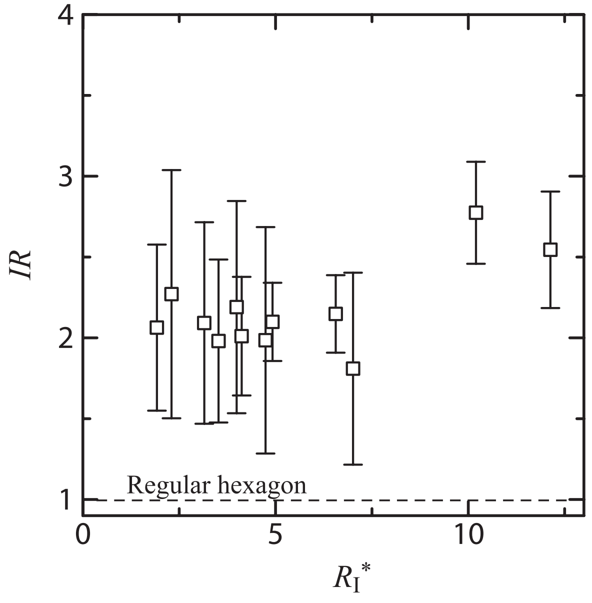

Figure 4.17: Variation of irregularity of convection cell $IR$ versus $R_{\rm I}$, where $IR = 1$ represents regular hexagon.

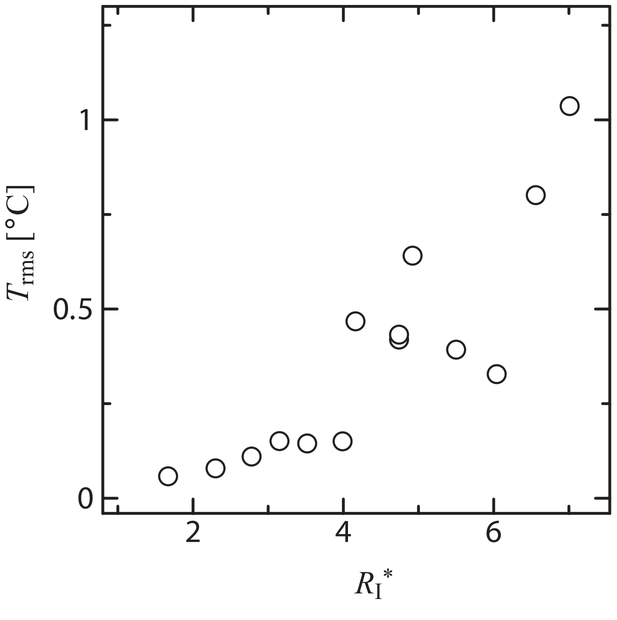

Figure 4.18: Variation of standard deviation of temperature on a horizontal cross section of the fluid layer, $T_{\rm rms}$, versus $R_{\rm I}$.

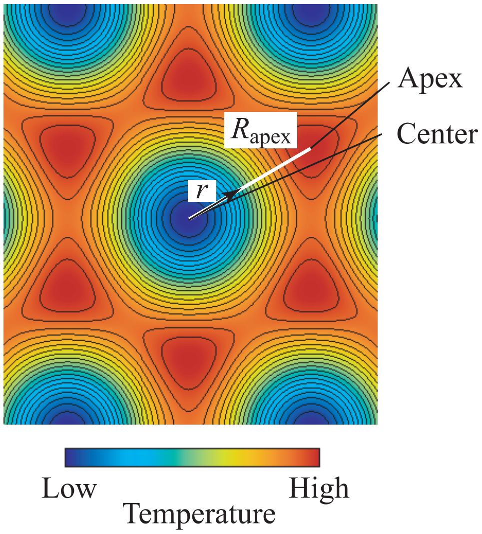

Figure 4.19: Temperature distribution of a cell given by linear theory [42]. $R_{\mathrm{apex}}$ represents distance between the center and the apex.

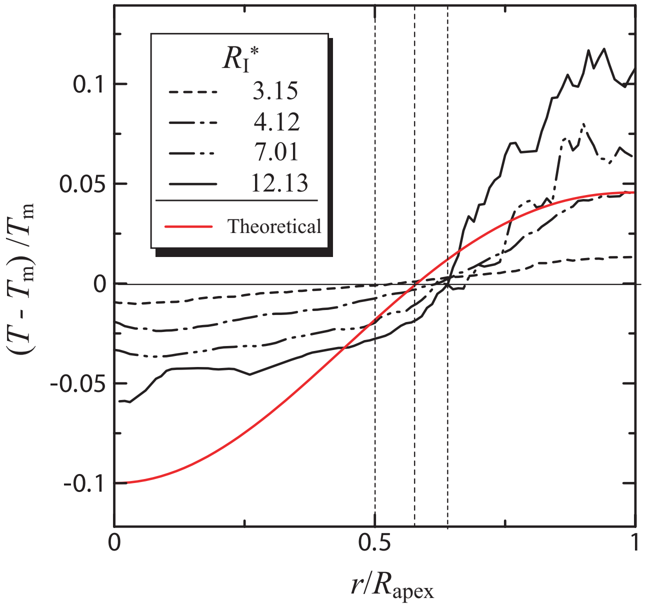

Figure 4.20: Temperature profile from the center to the apex of a cell at each $R_{\mathrm{I}}^{*}$, where $T_{\mathrm{m}}$ is mean temperature in a cell and $r$ represents distance from the center. Red line shows theoretical profile given by linear theory.

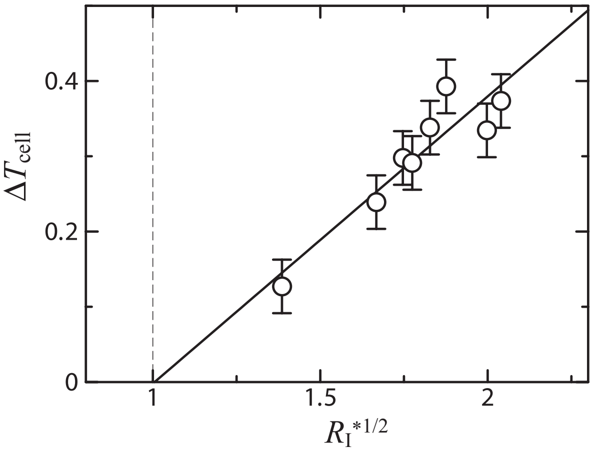

Figure 4.21: Variation of temperature difference between the center and the apexes of cell, $\Delta T_{\mathrm{cell}}$ versus $R_{\mathrm{I}}$, where solid line represents approximated linear function determined by least square.

## Chapter 5

# Ultrasonic Velocity Profile Measurement of Liquid Gallium Convection

## Abstract

In this chapter, we attempt to measure a velocity profile in a convection layer of liquid gallium by UVP, Ultrasonic Velocity Profiler, in order to visualize a flow pattern in low Prandtl number, R-B convection. Two trial UVP measurements were performed: a fluid flow of liquid gallium driven by rotating magnetic field and thermal convection of glycerol solution, which is transparent, as a test of a low velocity flow measurement. These results showed effectiveness of UVP measurement on the convective motion in liquid gallium layer.

We solved problems due to using liquid gallium, e.g. wetting, transmission of ultrasound, etc. and developed an experimental apparatus of liquid gallium convection, which is suitable for UVP measurement. We successfully measured the velocity profile of the convective motion in the liquid gallium layer and visualized convective flow pattern appearing in the layer. Estimated flow pattern from the velocity profile is quasi-regular roll pattern. Furthermore, spatio-temporal velocity distributions represented two different, periodic motions of convection roll, which may correlate with periodic variation of Nusselt number mentioned earlier studies.

## 5.1 Introduction

Rayleigh-Bénard (R-B) convection, which is a natural convection in a shallow fluid layer induced by external heating at the bottom and by cooling the top of the fluid layer, is a classical problem. It is an extremely fundamental phenomenon of natural convection appearing in science and engineering fields. Since Bénard [1], study of this problem has a long history and a large part of the studies in the scientific field is by an observation of flow pattern with changing parameters, such as Rayleigh number $R$ and Prandtl number $Pr$. Krishnamurti [36] collected observational data of R-B convection under various conditions and constructed a phase diagram (See Figure 1.1). This very famous phase diagram represents a transition of the flow pattern from steady state, which is thermal conduction state before onset of convection, to turbulent flow with respect to $R$ in the wide range of $Pr$. There is, however, no observation data for an extremely low $Pr$.

As liquid metal, which is low $Pr$ fluid, is opaque, we cannot use optical method to observe the flow pattern. Therefore, temperature measurement at points in the fluid layer by using a thermocouple was used to obtain the flow pattern until now. The objective of this study is to measure a velocity field of low $Pr$ convection in order to visualize the flow pattern directly. We used a liquid gallium layer and measured a velocity profile in this layer by UVP, Ultrasonic Velocity Profiler.

## 5.2 Characteristics of liquid gallium

We use liquid gallium as low $Pr$ fluid in this study. The advantage of using liquid gallium as working fluid is a safety. It does not easily become vapor like as mercury and does not react with water like a sodium. In addition, gallium has a conveniently low melting temperature (29.8 °C), which is much lower than lead and its alloys. Thanks to the low melting temperature, we can easily melt it or keep it as solid sate at room temperature (at least in our laboratory at Sapporo, Japan). As mentioned above, as liquid gallium is relatively easy to handle in comparison with other liquid metals, e.g. mercury and sodium, it has been used for a laboratory experiment to study a flow of low $Pr$ fluid [59, 60, 37], a magneto-convection [61, 62] and a liquid-solid phase change [63].

Table 5.1 shows physical properties of liquid gallium by Brito *et al.* [63], where the properties of water are also given in the table for comparison. Density is 6 times of that of water and kinematic viscosity is about 3 times smaller. On the other hand, thermal diffusivity is larger than water by two orders of magnitude. Then, the order of the physical property $\beta/\kappa\nu$ in the definition of Rayleigh number is

$$\frac{\beta}{\kappa\nu} \sim O(10^8),$$

while in water, it is

$$\frac{\beta}{\kappa\nu} \sim O(10^9).$$

As above estimations, liquid gallium can easily realize low Rayleigh number state than in water. This is a great advantage for a measurement by using ultrasonic beam as the present study because such measurement requires an sufficient height of the fluid layer, which has to be enough larger than effective diameter of an ultrasonic beam.

As a disadvantage, gallium oxidizes easily and quickly. Figure 5.1 shows photographs of (a) liquid gallium and (b) its oxide. The oxide does not have metallic luster and is a black fine powder. Gallium oxide is lighter than pure gallium and floats on the surface of pure liquid gallium layer as shown in this photograph. We remove oxides by deoxidization with using 10 % hydrochloric acid-ethanol solution before the experiments.

Table 5.1: Physical properties of water and liquid gallium [63].

| Physical properties | Symbol | Unit | Water* | Gallium** |
|---|---|---|---|---|
| Density | $\rho$ | kg/m$^3$ | $9.982\times10^2$ | $6.095\times10^3$ |
| Viscosity | $\mu$ | Pa·s | $1.002\times10^{-3}$ | $1.96\times10^{-3}$ |
| Kinematic viscosity | $\nu$ | m$^2$/s | $1.004\times10^{-6}$ | $3.22\times10^{-7}$ |
| Thermal conductivety | $\lambda$ | W/(m K) | 0.600 | 30.6 |
| Thermal diffusivity | $\kappa$ | m$^2$/s | $1.44\times10^{-7}$ | $1.18\times10^{-5}$ |
| Thermal expansion coefficient | $\beta$ | K$^{-1}$ | $2.08\times10^{-4}$ | $1.26\times10^{-4}$ |
| Specific heat | $c_p$ | J/(kg K) | 4182 | 381.5 |
| Electric conductivity | $\sigma$ | S/m | 0.7813† | $3.87\times10^6$ |
| Sound speed | $c$ | m/s | 1483 | 2860 |
| Acoustic impedance | $Z$ | $\times10^6$ kg/(m$^2$s) | 1.5 | 17.4 |
| Prandtl number | $Pr$ | - | 6.9 | 0.03 |

* measured at 20 °C.
** measured at 30 °C.
†Electric conductivity in the columun of water is a property of 0.5 wt % KCl solution.

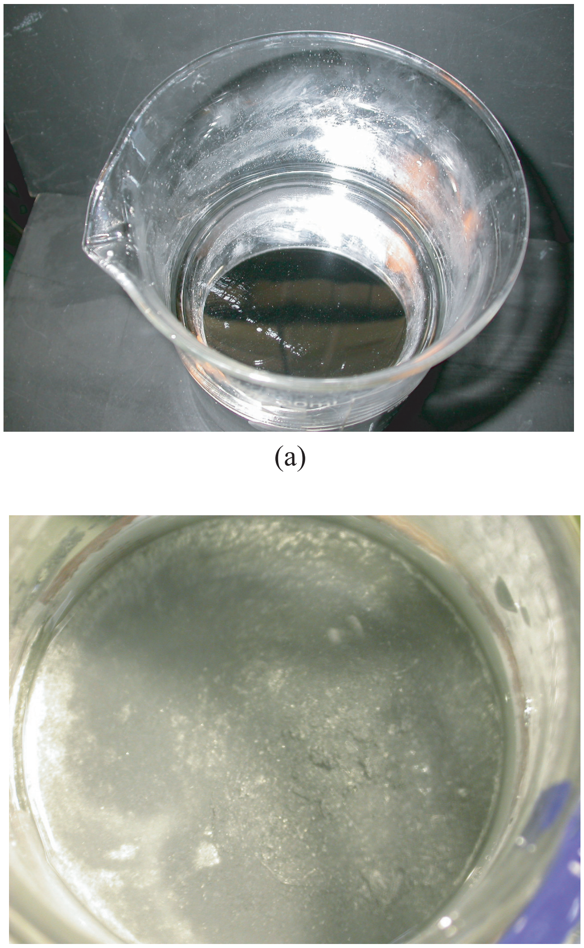

(a)

(b)

Figure 5.1: Photographs of (a) liquid gallium and (b) its oxide on the surface.

## 5.3 Ultrasonic velocity profiler

### 5.3.1 About UVP

UVP (Ultrasonic Velocity Profiler [64]) is a powerful tool in the experimental fluid dynamics [65, 66] and the fluid engineering [67, 68] because it can measure an instantaneous velocity profile in real time without post processing. As is described in Navier-Stokes equation, almost all kind of fluid flow varies spatially and temporally, and then it should be discussed at a spatio-temporal field in experimental study. In addition, UVP is applicable to a fluid flow of opaque liquid including liquid metals [67, 69]. This feature is a typical advantage in comparison with optical methods of velocity measurement such as LDA (Laser Doppler Anemometer) and PIV (Particle Image Velocimetry). Thanks to transmission property of ultrasound, UVP is applied in industries, for instance a flow metering in a large pipe [68] where a container wall is opaque, and a quality control in food processing [71, 72], in which fluid is generally opaque.

### 5.3.2 Principle

UVP utilizes Doppler shift frequency and ultrasonic (US) echography in order to determine an instantaneous velocity profile. Figure 5.2 shows (a) a basic configuration, (b) an US signal and (c) a measured velocity profile in UVP measurement. US burst with some cycles emitted from an US transducer propagates in a fluid and a part of the burst is reflected by a particle containing in the fluid. If there are sufficient particles in the fluid, such US echo comes back from everywhere on a propagating line of US burst to the same transducer. Assuming that particles move with the fluid, an echo signal contains velocity information of the fluid flow as Doppler shift frequency $f_{\mathrm{D}}$. Therefore, an instantaneous velocity at a position on the propagating direction $\xi$ is determined as

$$u_\xi(\xi, t) = c f_{\mathrm{D}} / 2 f_0, \tag{5.1}$$

where $c$ and $f_0$ are sound speed in a fluid and basic frequency of an emitted US burst. As suffix in the equation, measured velocity is a velocity component of the $\xi$ direction. Position on the $\xi$ axis is determined by time of flight of US burst $\tau$ as

$$\xi = c\tau/2. \tag{5.2}$$

Repetition of the burst emission and receiving US echo is required in order to determine an instantaneous Doppler shift frequency $f_{\mathrm{D}}(t)$ accurately. A repetition frequency of the burst emission $f_{\mathrm{prf}}$ determines possible length of measuring a velocity profile $\Xi$ as

$$\Xi = c/(2f_{\mathrm{prf}}). \tag{5.3}$$

More details of UVP measurement are written in the reference [64].

### 5.3.3 Seeding of US reflector

UVP measurement requires suspending US reflection particles in a fluid. The particle has to trace a target flow and such traceability is determined by density difference between the particle and the fluid flow, its size and its shape. Furthermore, required particle size depends on a wavelength of US burst, and a suitable size determined experientially is about quarter to half of the wavelength. We use $ZrB_2$ fine powder as a reflection particle of ultrasound, which has 50 $\mu$m diameter and 6.17 kg/m$^3$ density. It was also used in other work of UVP measurement of a liquid gallium flow and gave good results [69].

Because of large surface tension of liquid gallium, mixing $ZrB_2$ particles into liquid gallium is difficult than in water. We reduced surface tension coefficient in order to mix the particles with liquid gallium by keeping it high temperature, about 500 °C, during 30 min in a furnace.

Necessary amount of the particles depends on velocity of a target flow, i.e. it is required that enough value of a particle flux passing through a measurement volume of UVP measurement [1].

---

[1] Such seeding problem is investigated in Appendix 2, where we estimated optimum seeding experimentally.

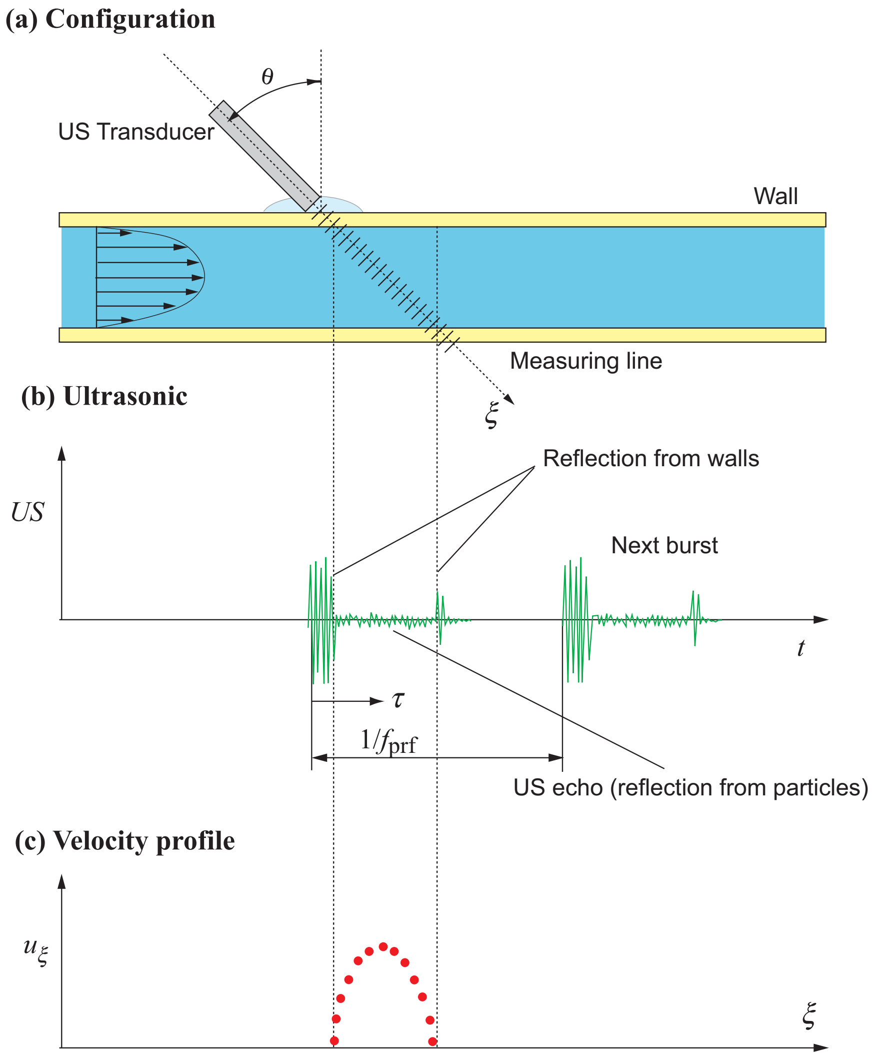

Figure 5.2: Schematic illustration of the process of UVP measurement; (a)Basic configuration, (b)Emitted US burst and echo signal and (c)Measured instantaneous velocity profile, where $\xi$ represents the propagating direction of US burst and it is the measuring direction of UVP.

### 5.3.4 Trial measurement 1

In fluid flowing with several 10 mm/s of speed, a velocity profile measurement by UVP is comparably easy than in low speed fluid flow because we do not have to consider the seeding problem. We performed a trial measurement of liquid gallium flow in a simple configuration. Figure 5.3 shows a photograph of an experimental apparatus and a supplemental illustration, where liquid gallium in a glass beaker with 87 mm inner diameter is covered with 10 % hydrochloric acid - ethanol solution. The liquid gallium layer is driven by rotating magnetic field, which is induced by a magnetic stirrer. The stirrer can keep temperature of the liquid gallium above its melting temperature by a heater in the stirrer. This is originally utilized for deoxidization of liquid gallium.

US burst, which has 4 MHz basic frequency and 5 mm effective diameter, is emitted from an US transducer located out side of the beaker. Velocity profile of liquid gallium layer along a propagating line of US burst, $\xi$ axis, is obtained by UVP, UVP monitor model Duo (Met-Flow S.A., Figure 5.4). Figure 5.5 shows an instantaneous velocity profile measured by UVP, where the horizontal and the vertical axes are distance from the transducer and velocity. The gallium layer is driven strongly near the center and weakly near the wall, and the measured velocity profile is consistent with estimated profile qualitatively. Estimated rotating speed near the center is 1 rps at the surface of the liquid gallium layer. If flow near the center has rigid body rotation, maximum velocity on the measurement line is in 90 to 100 mm/s. Therefore, the measured profile may be correct quantitatively.

Figure 5.6 shows a spatio-temporal plot of measured velocity, where color represents velocity. Measured profile varies periodically and is represented as stripes in the figure. The center of rotation in the liquid gallium layer moves with respect to time and this movement may induce the variation of velocity profile. Figure 5.7 shows a variation of the central position of rotation in the liquid gallium layer, which is determined by image analysis of a digital movie taken simultaneously with the UVP measurement. The vertical axis $x_\mathrm{c}$ and $y_\mathrm{c}$ in the figure represent the horizontal and the vertical position of the center, and the both variations have 5 periods in this time length, which corresponds to initial 20 seconds in Figure 5.6. There are also 5 periods in the spatio-temporal map.

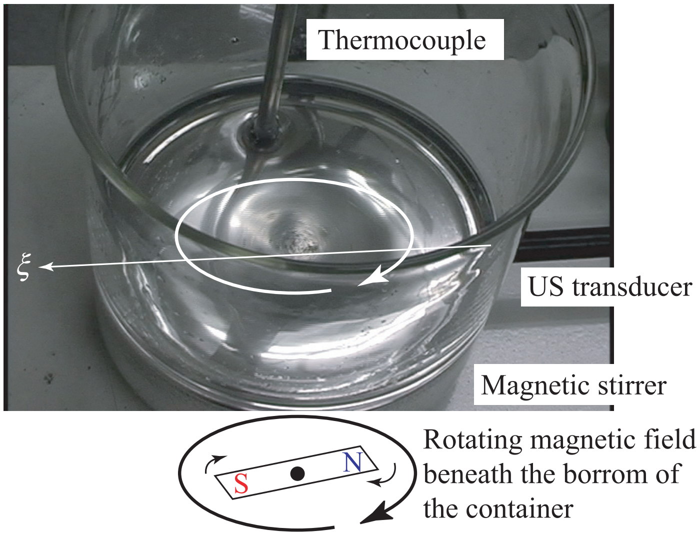

Figure 5.3: Photographs of experimental apparatus for the trial measurement and supplemental illustration, where liquid gallium layer in the beaker is covered by 10 % hydrochloric acid - ethanol solution. Rotating magnetic field made by magnetic stirrer drives liquid gallium layer.

Figure 5.4: Measurement system, UVP monitor model Duo, 4 MHz US transducer and laptop computer, Panasonic CF-T1.

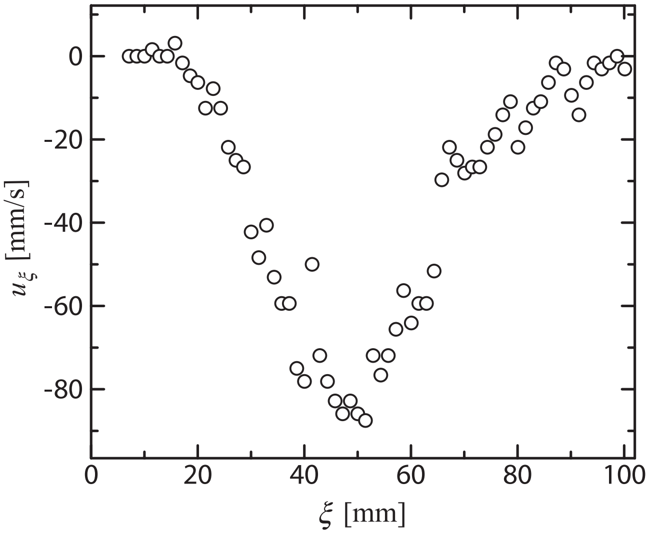

Figure 5.5: Instantaneous velocity profile in the liquid gallium layer measured by UVP.

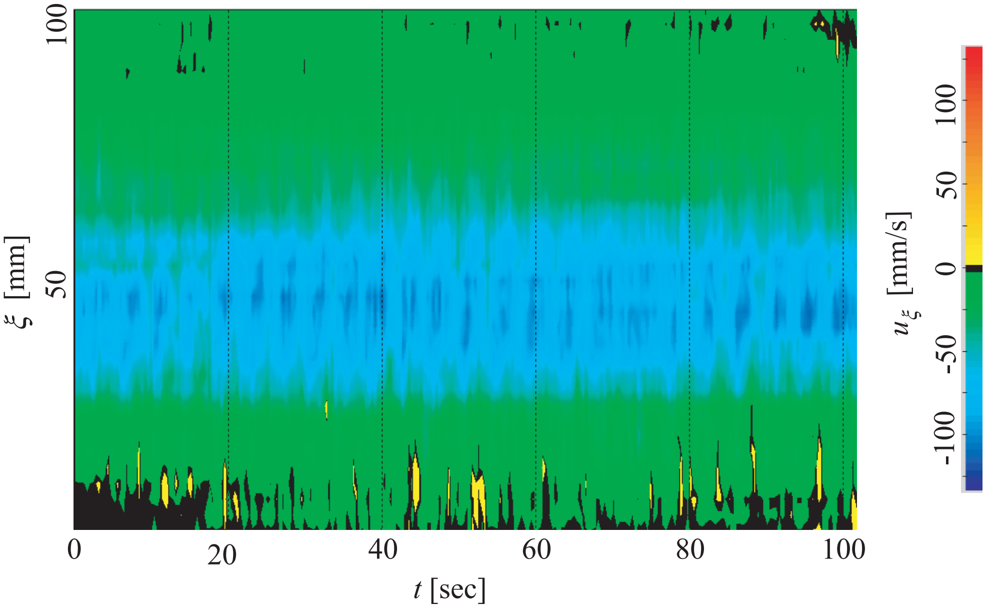

Figure 5.6: Spatio-temporal map of measured velocity, where color represents velocity.

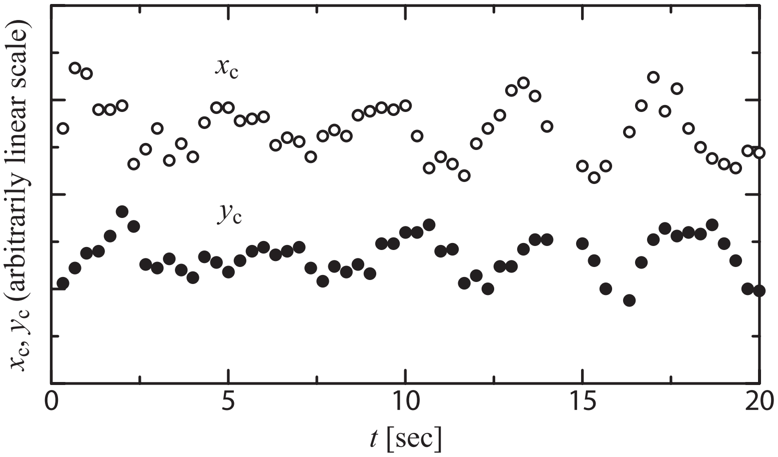

Figure 5.7: Variation of the center position of rotation in the liquid gallium layer, where $x_c$ and $y_c$ represent the horizontal and the vertical position of the center.

### 5.3.5 Trial measurement 2

Convective motion is very slow, which is approximately $O(1)$ mm/s. Furthermore, liquid gallium is opaque, and then it is hard to judge a validity of a measured velocity profile. We performed a trial measurement in transparent fluid in order to confirm effectiveness of UVP measurement of convective motion.

Figure 5.8 shows a schematic illustration of an experimental setup for this measurement. Fluid layer has 200 mm width, 30 mm depth and 20 mm height. The lateral wall is Plexiglas, and the top and the bottom plate are aluminum and copper. Flowing waters, whose temperature is controlled by a thermostatic bath, keep surface temperatures constant at the top and the bottom boundary of the fluid layer. Working fluid is 28 wt % glycerol solution. Convective flow pattern appearing in such configuration is well investigated, it becomes roll pattern as illustrated. US transducer emits US burst, which has 4 MHz basic frequency and 5 mm effective diameter, from outside of the fluid layer and UVP measures velocity along $x$ axis. The working fluid contains US reflectors, which are 50 $\mu$m nylon powder. We kept cooling temperature $T_1$ at 15 °C and heating temperature $T_2$ at 25 °C, and then setting Rayleigh number was $800R_c$, where $R_c$ is critical Rayleigh number of R-B convection.

A measured velocity oscillates on the measurement direction $x$ as shown in Figure 5.9(a), which is a temporally averaged velocity profile measured at a higher position of the fluid layer. An observed convective motion appearing in the fluid layer is roll pattern and Figure 5.9(b) is a sketch of the observed pattern. UVP measures approaching component of velocity toward the transducer as negative, and v.v. The measured velocity profile represents the observed convective motion very well to some extent such as rotating direction of rolls, number of roll, etc. We concluded that a velocity profile measured by UVP can visualize very slow convective motion.

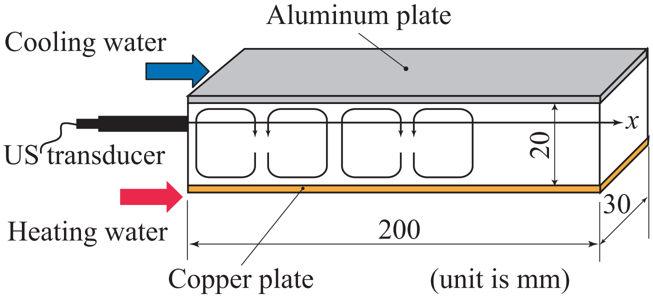

Figure 5.8: Schematic illustration of experimental apparatus for trial measurement of convective motion. Working fluid is 28 wt % glycerol solution.

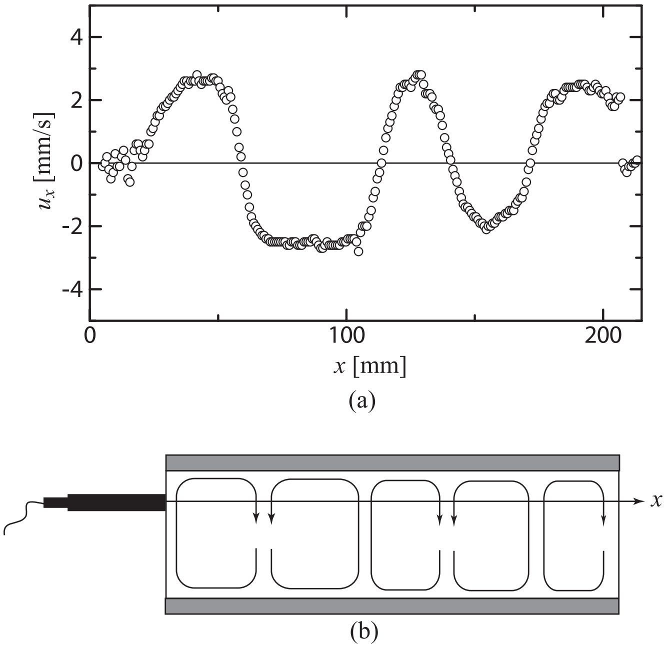

Figure 5.9: (a) Temporally averaged velocity profile measured at a higher position of the fluid layer. (b) Sketch of observed convective motion appearing in the fluid layer.

## 5.4 Experimental setup

A container for the liquid gallium layer consists of three parts, the lateral wall, the top plate and the bottom plate. Figure 5.10 (a) shows a photograph of the container and Figure 5.10 (b) also shows a schematic diagram of the container. The container has a slab shape, i.e. height $L$ is 50 mm, width 200 mm ($= 4L$) and depth 50 mm ($= L$). This shape of the fluid layer may restrict a convective flow pattern appearing in the fluid layer. We expected that roll pattern shall appear, which has a rotating axis parallel to $y$ axis. The lateral wall of the container is Pilex glass, which can wet with liquid gallium very well. Pilex glass has acoustic impedance $Z = 13.1 \times 10^6$ kg/(m$^2$s), which is very close to that of liquid gallium (see Table 5.1), therefore an US burst easily passes through the lateral wall. Furthermore, faces of the both ends at which US transducer is located have small thickness, 7 mm, than other faces, 10 mm in order to reduce attenuation of ultrasound. The top and the bottom plates have a circular channel with 12 mm diameter between 25 mm thickness copper plate and acryl plate. Temperatures of flowing waters in the channels were controlled by thermostatic bathes, AS-One model CH-202 and AS-One model LTB400. These water flows kept surface temperatures at the both plates constant. We kept cooling temperature $T_1$ at 32 °C, which is higher than the melting temperature of gallium, and varied Rayleigh number in a range of $R = 200$ to $800R_{\rm c}$ by changing heating temperature $T_2$, where $R_{\rm c}$ is the critical Rayleigh number of R-B convection in a shallow fluid layer, $R_{\rm c} = 1707.7$.

Since liquid gallium has high surface tension and is easy to oxidize, we filled liquid gallium into the container by following process. Figure 5.11 shows a schematic illustration of the filling process of liquid gallium into the container. The container was connected with a gallium tank and with a buffer tank, which was also connected with a vacuum pump. At first, the vacuum pump removes air from the buffer tank and the container. And then, liquid gallium was filled by pressurized argon gas until the container is totally filled with liquid gallium. Overflowed gallium remained in the buffer tank. Liquid gallium was well deoxidized by the developed deoxidization system shown in Section of trial measurement 1.

US transducer was located at an end of the fluid container and US burst emitted by the transducer propagated in the gallium layer parallel to $x$ direction. US burst has 4 MHz basic frequency and 5 mm effective diameter. UVP measured velocity along the propagation line of US burst. As already mentioned in Section 5.3.3, reflection particle of US burst is $ZrB_2$

fine powder. It is slightly heavier than liquid gallium and we could not receive the US echo two hours after a beginning of the measurement.

Table 5.2 shows specifications of the experimental setup.

Table 5.2: Specifications of the experimental setup

| | |
|---|---|
| Fluid container | |
| Size | 200 mm × 50 mm × 50 mm (4 : 1 : 1) |
| Lateral wall | Pilex glass with 7 mm thickness at the both ends other 10 mm |
| Top and bottom plate | 25 mm thick copper plate |
| Heating | Flowing water, thermostatic bath, AS-One model CH-202 |
| Cooling | Flowing water, thermostatic bath, AS-One model LTB400 |
| Working fluid | Liquid gallium |
| US burst | 4 MHz basic frequency and 5 mm effective diameter |
| US reflector | 50 $\mu$m $ZrB_2$ fine powder |
| Filling Ga | Vacuum pump, buffer tank, gallium tank and Ar gas pressurization |

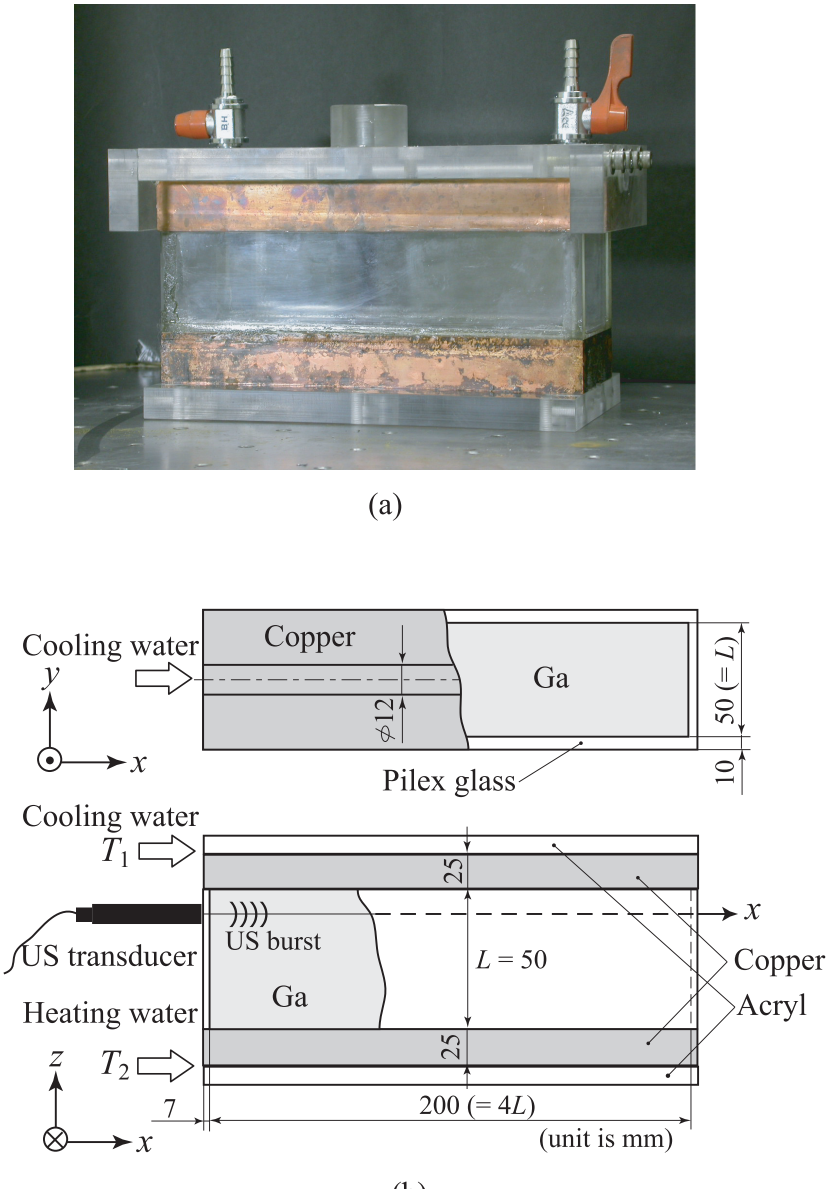

Figure 5.10: (a) Photograph and (b) schematic diagram of the experimental apparatus for the liquid gallium layer.

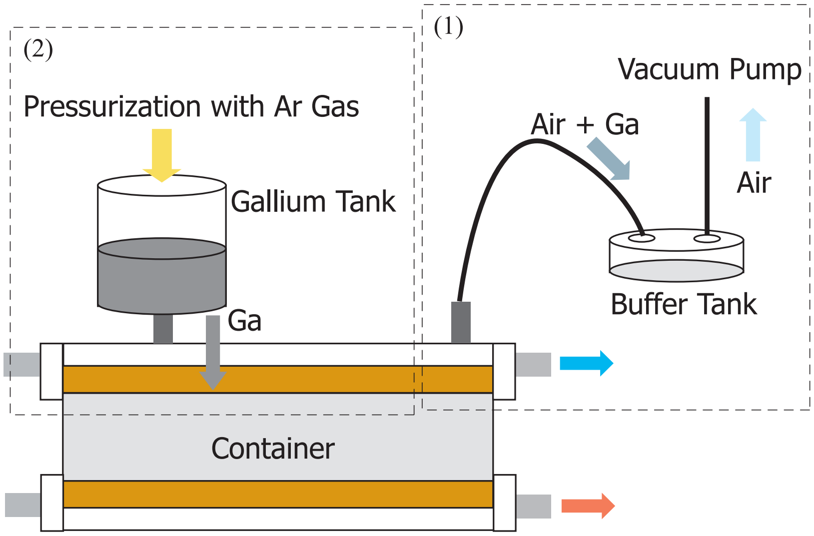

Figure 5.11: Schematic illustration of a filling process of liquid gallium to the container: (1) Vacuum pump removes air from the container and buffer tank (2) Pressurization with argon gas injects liquid gallium to the container.

## 5.5 Results and discussions

### 5.5.1 Velocity profile & flow pattern

Figure 5.12 shows temporally averaged velocity profiles measured at each height of the fluid layer, where the horizontal axis $x$ represents distance from the US transducer. Schematic illustrations attached in the figures represent approximate measurement positions for each profile. Sampling period of the profile is 80 msec and the number of profiles for the average is 1024. Spatial resolution on the $x$ axis is 1.44 mm. Rayleigh number determined by Equation (5.1) and by Table 5.1 was $770R_{\mathrm{c}}$ at which convective motion is unsteady.

At a lower position of the fluid layer (Figure 5.12(a)), velocity oscillates on the measurement direction and the profile has two periods of variation. Magnitude of measured velocity is in a range from 0 to ±10 mm/s. At a higher position (Figure 5.12(b)), velocity also oscillates and a measured velocity profile is approximately symmetrical with that measured at the lower position. Furthermore, range of magnitude of velocity is similar. On the contrary, at a middle position, the measured profile has very small velocity and has no typical variation on the measurement direction (Figure 5.12(c)).

We can easily imagine a flow pattern from these velocity profiles as a schematic illustration shown in Figure 5.13. The estimated flow pattern matches to with the expected flow pattern, which is roll structure arranged parallel to $y$ direction. At the setting Rayleigh number, $R = 770R_{\mathrm{c}}$, state of convection is turbulence according to the flow régime diagram drawn by Krishnamurti [36] (See Figure 1.1). There is, however, the quasi-regular convective flow pattern in the present system due to effects of side boundary. Numerical study of low $Pr$ fluid, $Pr = 0.01$, reported that regular rolls appear in the fluid layer at a Rayleigh number, $R = 16R_{\mathrm{c}}$ [70]. But it is extremely small than in present study by one order.

### 5.5.2 Spatio-temporal velocity distribution

As already mentioned in the earlier section, UVP can measure an instantaneous velocity profile, and then we can investigate spatio-temporal variation of convective motion. Figure 5.14 shows spatio-temporal velocity distributions measured at various Rayleigh numbers, where the horizontal and the vertical axes are time and position respectively, color map represents velocity. Black points appearing in the figures represent "zero" data induced by lack of reflection particle of US burst, which is discussed in Appendix 2. A vertical cross section of these figures represents an instantaneous velocity profile. These velocity distribution were measured at a lower position of the fluid layer like Figure 5.12(a).

At $R = 214R_c$, there are four convection rolls in the fluid layer (Figure 5.14(a)), where counterclockwise rotation of a roll is represented by yellow and clockwise rotation green. Convective motion is unsteady and these rolls vary slowly as expressed by moving boundary between yellow and green. Many notches exist at the boundaries, however, these notches don't express a small scale - convective motion but are scatters on measurements. At higher Rayleigh number, $R = 428R_c$, there are also four rolls in the fluid layer and magnitude of velocity slightly increases in comparison with the distribution measured at lower Rayleigh number (Figure 5.14(b)). A band enclosed with broken line repeats expansion and contraction of the roll with keeping its position on $x$ axis as shown in Figure 5.15(a) by a schematic illustration. This movement is very slow and its period is approximately 60 sec (it corresponds 0.017 Hz on frequency). At further high Rayleigh number, $R = 770R_c$, we can see a different motion of a convection roll (Figure 5.14(c)). There are also four rolls, which has the same size with that measured at lower Rayleigh numbers. But enclosed roll moves on the $x$ axis periodically without changing its size as in contract to Figure 5.15(b). Furthermore, a motion of neighboring rolls of the focused roll corresponds to that at lower $R$ as shown by illustrations. Convective motion becomes faster than in lower $R$ and its frequency determined by Fourier analysis is 0.059 Hz.

## 5.6 Conclusion

UVP, Ultrasonic Velocity Profiler, is a powerful tool to investigate fluid flow of opaque liquid and we applied it to velocity measurement of thermal convection of liquid gallium layer as first step of investigation of low Prandtl number, Rayleigh-Bénard convection. Two trial measurements were performed prior to the experiments; a measurement of a fluid flow of liquid gallium driven by rotating magnetic field showed effectiveness of UVP measurement of liquid gallium flow, and a measurement of thermal convection of glycerol solution, which is transparent, confirmed validity of low speed flow measurement by UVP. We developed deoxidization system of liquid gallium by using a magnetic stirrer.

Experimental apparatus for liquid gallium was developed, where problems due to using liquid gallium, wetting of liquid gallium, transmission of ultrasound, etc. are completely solved. We successfully measured a velocity profile of the convective motion in the liquid gallium layer and visualized convective flow pattern appearing in the layer. Estimated flow pattern is quasi-regular roll pattern, which consists of 4 rolls arranged parallel to the narrow side of the fluid layer. Generally, it has been mentioned that a flow state is turbulence at the setting Rayleigh number and there is no typical pattern in the fluid layer. This roll pattern may be induced by effect of boundary of slab shape fluid layer, but it has never reported at low Prandtl number fluid. At a targeted range of Rayleigh number in this study, convective motion is unsteady, and spatio-temporal velocity distributions represented two different, periodic motions of convection roll. Until now, such periodic motions have been taken as periodic variation of Nusselt number or other secondary variables, and then we showed it as variation of velocity profile for the first time.

In this study, we solved problems on the velocity profile measurement of liquid metal by using ultrasound, e.g. seeding of US reflectors, wetting and transmission of ultrasound, and then we established the method. There are processes in which liquid metal flow is utilized in the industrial field, and this measurement method can be applied to diagnosing the processes.

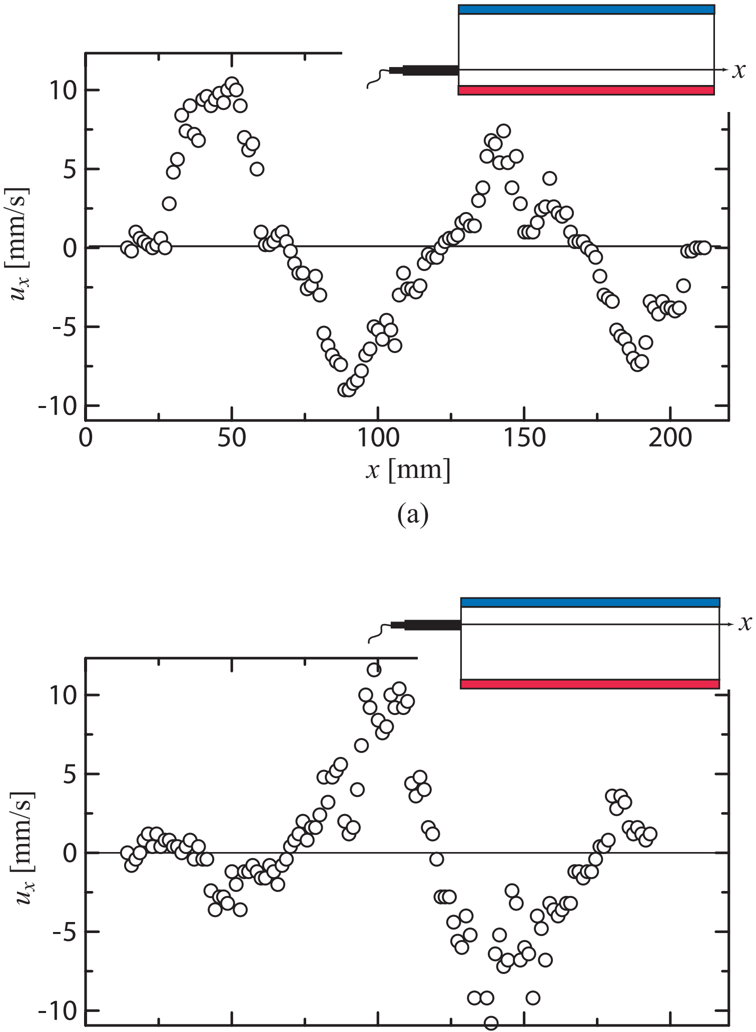

(a)

(b)

Figure 5.12: Temporally averaged velocity profiles measured by UVP (a) at a lower position, (b) a higher position and (c) a middle position, where $R = 770R_c$. Schematic illustrations in the figures roughly express measurement positions.

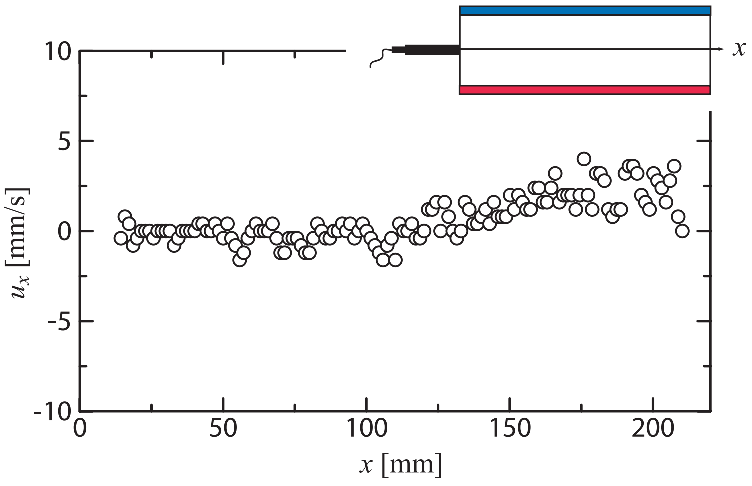

(c)

Figure 5.12: Temporally averaged velocity profiles measured by UVP (a) at a lower position, (b) a higher position and (c) a middle position, where $R = 770R_\mathrm{c}$. Schematic illustrations in the figures roughly express measurement positions.

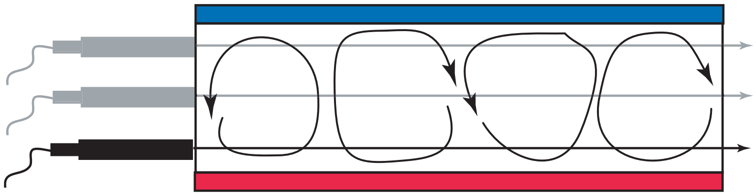

Figure 5.13: Schematic illustration of the estimated flow pattern from measured velocity profiles at each height of the fluid layer.

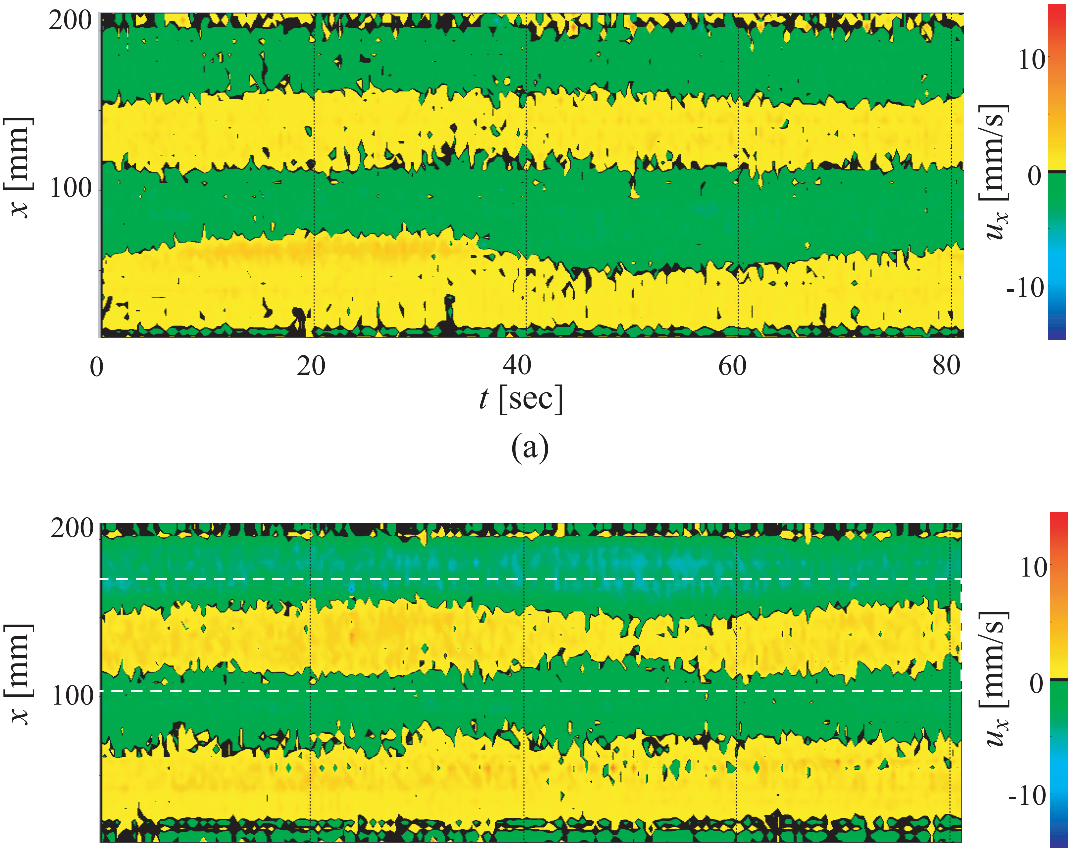

(a)

(b)

Figure 5.14: Spatio-temporal velocity profiles measured at a lower position of the fluid layer; (a) $R = 214R_{\mathrm{c}}$, (b) $R = 428R_{\mathrm{c}}$ and (c) $R = 770R_{\mathrm{c}}$.

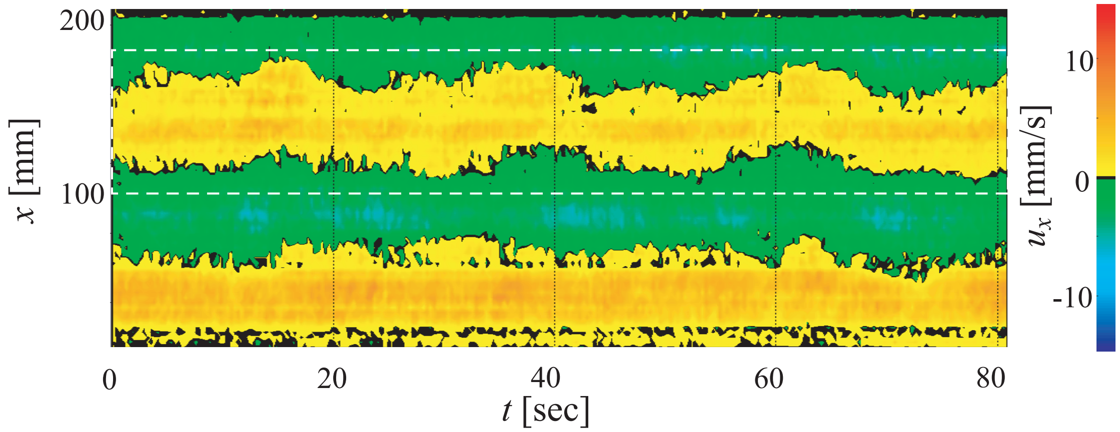

(c)

Figure 5.14: Spatio-temporal velocity profiles measured at a lower position of the fluid layer; (a) $R = 214R_c$, (b) $R = 428R_c$ and (c) $R = 770R_c$.

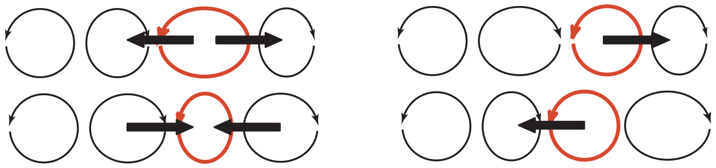

(a) (b)

Figure 5.15: Schematic illustration of motions of convection roll; (a) a roll repeats expand and reduction with keeping its position, (b) a roll moves on the horizontal direction periodically without changing its size.

## Chapter 6

# Conclusion

In this work, mainly two research themes were investigated; (A) natural convection induced by internally heated convection, and (B) ultrasonic velocity profile measurement of low Prandtl number, Rayleigh-Bénard convection. In Chapter 2, theoretical estimation of effect of heat source distribution on internally heated convection was performed. In Chapter 3 and 4, internally heated convection was investigated experimentally in order to reexamine characteristics of the convection. In Chapter 5, a velocity profile in the convection layer of liquid gallium was measured by UVP, Ultrasonic Velocity Profiler. The results obtained in each Chapter already summarized as Conclusion individually, thus we rewrite these conclusions as the conclusion of this thesis.

Linear stability analysis was used to clarify the effects of heat source distribution on internally heated convection. The conditions for the onset of convection, namely the critical Rayleigh number $R_\mathrm{c}$ and critical wavenumber $k_\mathrm{c}$, were determined for non-uniform distributions of heat source in which heat source is concentrated in the lower or the upper part of the fluid layer. Concerning the effects of the heat source distribution a function of $R_\mathrm{c}$ and $k_\mathrm{c}$, (defined with respect to the characteristic length of the source distribution), the following conclusions have been drawn. Concentration of the heat source near the bottom boundary lowers $R_\mathrm{c}$ and eases convection occurring, namely it lowers the temperature difference at which convection occurs. Variation of $k_\mathrm{c}$, however, is small, and there is only a slight influence of this distribution on the size of the convection cell. Concentration of the heat source near the top boundary increases $R_\mathrm{c}$ and prevents convection occurring. When the concentration is extreme, with extremely small $\eta$, $k_\mathrm{c}$ changes greatly in contrast to when the heat source is concentrated near the lower boundary. Furthermore, an asymmetry of the vertical velocity $\tilde{w}$ appears, and then convective flow near the bottom boundary becomes weak. These variations of the characteristics of convective motion may be caused by a quasi-stable layer formed on the lower part of the fluid layer. In common with both heat source distributions, even a slight deviation from uniform heating induces a large difference in the total power input, even though the temperature profiles are similar.

"Mixed convection" where wall heating at the bottom boundary is combined with internal heating was also investigated. The dimensionless parameter $\Theta$, defined as the ratio of internal to external Rayleigh number, determines the form of the temperature profile. A local stable layer in which temperature increases in the vertical direction is formed near the bottom boundary when $\Theta$ is greater than 1, and a temperature profile similar to pure internally heated convection for $\Theta < 1$. For large values of $\Theta$ a strong asymmetry in the vertical velocity $\tilde{w}$ appears, and flow near the bottom boundary becomes weak. When the heat source distribution is non-uniform and concentrated near the upper boundary, an asymmetry appears even for small internal Rayleigh numbers; that is, small value of $\Theta_\eta$. The local stable layer formed in this case is thicker than for uniform internal heating. It spreads into the upper half of the fluid layer even for a small value of $\Theta_\eta$. Such a local stable layer might cause a large change in $R_\mathrm{c}$ and $k_\mathrm{c}$.

The system investigated in this study is typical in nature and may be different in industrial configurations. The results, however, might be common characteristics related to many convective phenomena. Asymmetry of convective motion caused by a local stable layer is typical of internally heated convection with distributed internal heat source. It is often explained that such asymmetry is caused by temperature dependence of physical properties such as kinematic viscosity. But it might happen even in the ideal system without such a temperature dependence.

As mentioned in the Chapter 1, an improved experiment for internally heated convection will be explained in Chapter 3 and we have found that the cell undergoes elongation with increasing $R_\mathrm{I}$. The wavelength changes by nearly 100% in the range $R_\mathrm{I} = 2700$ to 8100. In my experiment, the heat source is not strongly concentrated near the upper boundary as modeled here, and this elongation of the cell might not be caused by non-uniform distribution of heat source as concluded from the present results.

In order to confirm the cell dilatation, an experiment that is more closely approximated by the theoretical models was performed. The thermal boundary condition at the bottom plate became nearly adiabatic by using vacuumed glass as the bottom plate, and the non-uniformity of the internal heating was reduced by increasing the height of the fluid layer. Fluid motion and the temperature field were visualized to estimate the cell dilatation using Kalliroscope and Thermo-chromic Liquid Crystals (TLC) suspension respectively. With the improvements of the experimental setup in the present study, cell dilatation could be observed in digital photographs for each $R_{\rm I}^{*}$. We conclude, therefore, the dilatation of convection cell with respect to internal Rayleigh number is characteristic of natural convection induced by internal heat generation.

By using the Fourier transform, the wavenumber of the convection cells for each $R_{\rm I}^{*}$ was calculated from brightness information, extracted from images of the flow obtained using Kalliroscope or TLC for visualization. The cell dilatation could be expressed quantitatively from measurements of the cell wavenumber as a function of internal Rayleigh number. The technique we used to determine the wavenumber removed the subjectivity inherent in the methods used by previous authors. The present results were compared with the results in an earlier study [23] and the influence of the thermal boundary condition at the bottom of the fluid layer on the variation of wavenumber was discussed. We mentioned that a local stable layer with a positive vertical temperature gradient, which is induced by imperfection of thermal insulation at the bottom boundary, reduces the internal Rayleigh number substantially.

As a result of the cell dilatation, an expanded cell breaks up and a smaller cell appears in the expanded cell like double structure as mentioned in Schwiderski & Schwab [23]. Such a structure does not appear in the process of the transition to turbulent flow in standard Rayleigh-Bénard convection, as shown in the phase diagram [36].

In order to investigate natural convection induced by internal heat generation quantitatively, measurement of temperature field in the fluid layer was performed using TLC, Thermo-chromic Liquid Crystal. Calibration system was developed in order to convert color information extracted from visualized images to temperature field by taking a picture of a horizontal temperature gradient in the shallow fluid layer. Calibration curve between a Hue that is one of color information component on HSI color system and a temperature was determined as a function of Hue to fourth power, and every visualized image taken at each internal Rayleigh number was converted to temperature field. There is only small error in the temperature conversion.

Individual cells on the horizontal temperature field were extracted based on some assumptions. Variation of the area of cells, which is determined from extracted cells, with respect to reduced internal Rayleigh number, $R_{\mathrm{I}}^*$ were shown. We determined the slope of the variation and showed that the slope changes at $R_{\mathrm{I}}^* \sim 5$. Variation of deviation of the area versus $R_{\mathrm{I}}^*$ was also investigated and there is no typical variation. Irregularity of hexagonal cell was defined by using a deformation from equivalent circle of cell, and variation of irregularity versus $R_{\mathrm{I}}^*$ was shown. There are also no typical variation as well as variation of deviation of the area. We concluded that convection cell appearing in internally heated convection is initially irregular at onset of convection. Standard deviation of temperature determined from overall temperature field changes a slope of its variation with respect to $R_{\mathrm{I}}^*$ at $R_{\mathrm{I}}^* \sim 4$ as well as variation of area of cell. We discussed that there is transition point at this Rayleigh number and it may be induced by transition of the flow pattern. Temperature profile from the center to the apex of the cell extracted from converted temperature field was compared with the profile given by liner theory. As the results, we found that descending flow exists in a cell with comparably wide area and ascending flow bringing up high temperature fluid is localized near the apexes of cell. Critical Rayleigh number was determined experimentally by variation of temperature difference between the center and the apex of the cell, and it agrees well with theoretical value estimated by linear stability analysis.

UVP, Ultrasonic Velocity Profiler, is a powerful tool to investigate fluid flow of opaque liquid and we applied it to velocity measurement of thermal convection of liquid gallium layer as first step of investigation of low Prandtl number, Rayleigh-Bénard convection. Two trial measurements were performed prior to the experiments; a measurement of a fluid flow of liquid gallium driven by rotating magnetic field showed effectiveness of UVP measurement of liquid gallium flow, and a measurement of thermal convection of glycerol solution, which is transparent, confirmed validity of low speed flow measurement by UVP. We developed deoxidization system of liquid gallium by using a magnetic stirrer.

Experimental apparatus for liquid gallium was developed, where problems due to using liquid gallium, wetting of liquid gallium, transmission of ultrasound, etc. are completely solved. We successfully measured a velocity profile of the convective motion in the liquid gallium layer and visualized convective flow pattern appearing in the layer. Estimated flow pattern is quasi-regular roll pattern, which consists of 4 rolls arranged parallel to the narrow side of the fluid layer. Generally, it has been mentioned that a flow state is turbulence at the setting Rayleigh number and there is no typical pattern in the fluid layer. This roll pattern may be induced by effect of boundary of slab shape fluid layer, but it has never reported at low Prandtl number fluid. At a targeted range of Rayleigh number in this study, convective motion is unsteady, and spatio-temporal velocity distributions represented two different, periodic motions of convection roll. Until now, such periodic motions have been taken as periodic variation of Nusselt number or other secondary variables, and then we showed it as variation of velocity profile for the first time.

In this study, we solved problems on the velocity profile measurement of liquid metal by using ultrasound, e.g. seeding of US reflectors, wetting and transmission of ultrasound, and then we established the method. There are processes in which liquid metal flow is utilized in the industrial field, and this measurement method can be applied to diagnosing the processes.

# Appendix 1:
# Observation of Mixed Convection

## Introduction

In the previous sections, we focused our interest on internal heating and then it was assumed that the bottom of the fluid layer is an adiabatic boundary to exclude an effect of the external heating from the bottom. A vacuumed glass realized such adiabatic boundary condition and some characteristics of internally heated convection have been confirmed. There is, however, no such idealized condition in nature and in industrial problems. There are usually two kinds of heat source, internal and external heat source, in atmosphere, sea and so on. Convective motion in such an actual system may depend on a magnitude and a ratio of heat amount of both heat sources. For example, more than 80 % of heat amount driving the mantle is internal, and thus internal heating may dominant in the mantle convection [13]. Although such "mixed convection" (mixture of Rayleigh-Bénard convection and internal heat source convection) exists everywhere, a convective motion in a mixed convection has not been clarified even for small Rayleigh number.

As already mentioned in Section 2.5, form of a base temperature profile (a temperature profile in the conduction state) for the vertical direction is determined by the ratio of the internal to external Rayleigh numbers as follows

$$\Theta = R_{\mathrm{I}}/R.$$

Characteristics of form of the temperature profile becomes different whether $\Theta > 1$ or not. Namely, when $\Theta > 1$, a local stable layer in which temperature gradient is positive is formed near the bottom boundary. This layer may affect a convective flow pattern for the horizontal plane at onset of convection because the flow pattern is determined by the base temperature profile for the vertical direction and by a shape of the lateral boundary. Critical Rayleigh number and critical wavenumber calculated by Sparrow *et al.* [26] is given in Table 1. Critical wavenumber increases with respect to $\Theta$ for $\Theta > 1$ but it is constant for $\Theta < 1$. Namely, cell size may be independent of magnitude of internal heating at onset of convection for $\Theta < 1$. In this section, we investigate the flow pattern for each value of $\Theta$ qualitatively.

At first, 2-dimentional roll pattern is formed on pure Rayleigh-Bénard convection without internal heating. Internal heating is added gradually to the fluid layer and convective flow pattern is observed for each value of $\Theta$. This observation is repeated for a region of $R$ at which a roll stably exits in the fluid layer. This corresponds to an investigating stability of a roll pattern under internal heating.

Table 1: Critical wavenumber and critical Rayleigh number for mixed convection [26]

| $\Theta$ | $k_c$ | $R_c$ |
|---|---|---|
| 0 | 3.12 | 1707.765 |
| 0.1 | 3.12 | 1707.636 |
| 0.25 | 3.12 | 1706.953 |
| 0.5 | 3.12 | 1704.453 |
| 1 | 3.13 | 1694.953 |
| 1.5 | 3.14 | 1679.407 |
| 2.5 | 3.18 | 1632.886 |
| 5 | 3.30 | 1462.863 |
| 7.5 | 3.43 | 1279.267 |
| 10 | 3.53 | 1118.430 |
| 25 | 3.68 | 878.339 |
| 20 | 3.74 | 717.201 |
| 30 | 3.82 | 521.403 |
| 40 | 3.86 | 408.558 |
| 70 | 3.92 | 247.075 |
| 100 | 3.94 | 176.936 |
| $\infty$ | 4.00 | — |

## Configuration

Coordinate system and main symbols are defined again in Figure 1. A heating boundary at the bottom has constant temperature $T_2$, $T_2 > T_1$. It is assumed that internal heat generation $H$ is uniform for the fluid layer. The control parameter of the temperature profile $\Theta$ is rewritten by using these symbols as follows,

$$\Theta = \frac{HL^2/2\lambda}{T_2 - T_1}. \tag{1}$$

Internal and external Rayleigh numbers are defined as

$$R_{\mathrm{I}} = \frac{g\beta H L^5}{2\lambda\kappa\nu}$$

and

$$R = \frac{g\beta(T_2 - T_1)L^3}{\kappa\nu}.$$

## Experimental apparatus and method

### Apparatus

An experimental apparatus for the investigation of mixed convection mainly consists of two parts, a fluid container with a heating plate and a cooling plate as the rid of the container. The cooling plate is the same component used in the experiment for the internally heated convection. Detail of the cooling plate is described explained in Section 3.3. Figure 2 shows a schematic illustration of the fluid container and Figure 3 is a photograph of the container with a heating block which includes a channel to circulate heating water. Size of the fluid container is also same as the apparatus used for Chapter 3 and 4, namely the horizontal cross section is nearly square which is 220 mm (including 5 mm gaps at the both side of the layer) times 210 mm. Lateral walls of the container are made of 10 mm thick Plexiglas, and one pair of the sides has a notch to set an electrode. Another pair of the side has a step shape notch to support the cooling plate, and height of the fluid layer is set as 7 mm. The bottom of the fluid container is a glass plate with thickness of 2 mm. Heating water controlled by a temperature control bath is circulated under the bottom plate of the fluid layer to keep bottom temperature constant. The bottom of the channel of heating water is made of glass 5 mm thick for visualization of the fluid layer, and other parts are made of Plexiglas. Thermal insulating blocks cover the channel to reduce heat loss. Table 2 shows a specification of the fluid container and the heating system.

Electric equipment in order to pass electric current to the fluid layer, electrode, power supply, current meter and voltmeter, are same to the experimental setup used in Chapter 3 and 4. Working fluid is the same too.

As mentioned above, the heating plate is made of glass and whose thermal conductivity is smaller than aluminum used for the cooling plate. And then, temperature difference between the top and the bottom surface of the heating plate cannot be neglected. Measuring a

Table 2: Specifications of the experimental setup

| | |
|---|---|
| Fluid container | |
| Size | 220 mm(including 5mm gaps) × 210 mm × 7 mm |
| Lateral wall | 10 mm thick Plexiglas |
| Bottom plate | 2 mm thick glass |
| Heating system | |
| Channel | 30 mm height |
| Control | thermostatic bath, AS-One model LTB400, 0.1 °C acculacy |

temperature at the bottom surface of the fluid layer directly, however, is not possible because a thermal indicator such as a naked thermocouple which does not affect a convective motion cannot be used to determine the bottom temperature due to an electric current passing in the fluid layer. In order to estimate a temperature at the bottom boundary, a following method is used.

Following assumptions as illustrated in Figure 4 are used: (1) Thermal insulation of the channel is perfect except the part in contact with the fluid layer, and exchange of heat occurs only in this area. (2) Temperature at the upper surface of the channel $T_{\mathrm{m}}$ is equal to the mean temperature at the horizontal half position of the channel. (3) Temperature gradient in the glass plate is constant at every position. Based on the above assumptions, specific heat flux through the glass plate $q$ is derived as

$$\begin{aligned} q &= \frac{Q}{S} \\ &= -\lambda_{\mathrm{g}} \frac{dT}{dz} \sim \lambda_{\mathrm{g}} \frac{T_{\mathrm{m}} - T_2}{L_{\mathrm{g}}}, \end{aligned}$$

where $Q$ represents amount of total heat flux through the glass plate, $\lambda_{\mathrm{g}}$ thermal conductivity of the glass, $L_{\mathrm{g}}$ thickness of the glass plate, $S$ contact area with the fluid layer. $Q$ is also derived as

$$Q = Q_{\mathrm{f}} c_p \rho (T_{\mathrm{i}} - T_{\mathrm{o}}),$$

where, $Q_{\mathrm{f}}$ is flow rate of heating water, $c_p$ and $\rho$ are specific heat and density of water respectively. $T_{\mathrm{i}}$ and $T_{\mathrm{o}}$ are inflow and outflow temperature. From these temperatures,

$$T_{\mathrm{m}} = \frac{T_{\mathrm{i}} - T_{\mathrm{o}}}{2}.$$

By algebraic operation of above equations, the temperature at the bottom surface of the fluid layer $T_2$ is determined as

$$T_2 = \frac{T_\mathrm{m}}{2} - \frac{QQ_\mathrm{f}}{\lambda_\mathrm{g} S} L_\mathrm{g}. \tag{2}$$

Temperature $T_\mathrm{i}$ and $T_\mathrm{o}$ are determined by standard thermometers with 0.1 °C minimum scale.

### Visualization

Convective motion of the mixed convection was visualized by Kalliroscope [43], and visualized photographs were taken by a digital camera, Nikkon D1, from the bottom of the fluid layer.

### Rayleigh-Bénard Convection

As already mentioned, in this chapter, we investigate a stability of roll pattern appearing in Rayleigh-Bénard convection under internal heating. In investigations for Rayleigh-Bénard convection, conventionally, height of the fluid layer is set small, say 4 mm or lower in order to reduce the influence of the temperature dependence of physical properties such as kinematic viscosity, and a larger horizontal fluid layer is used to reduce an influence of the lateral wall. In the present apparatus, however, the fluid layer is thicker than apparatus used in other investigations in order to reduce non-uniformity of internal heat generation and the horizontal area is smaller than in earlier works. In order to confirm reliability of the apparatus, we produce 2-dimentional rolls in the Rayleigh-Bénard convection without internal heating.

Figure 5 shows visualized photographs of convective motion in the fluid layer for each value of Rayleigh number $R$, where $R_\mathrm{c}$ is critical Rayleigh number for Rayleigh-Bénard convection calculated by Reid & Harris [38], $R_\mathrm{c} = 1707.68$. At $R \sim 0.9R_\mathrm{c}$, convective motion appears only near the both sides of the fluid layer as shown in Figure 5(a), and it may be caused by free surface in the gap between the cooling plate and the lateral wall. At $R \sim 2.5R_\mathrm{c}$, as shown in Figure 5(b), a roll appears covering the fluid layer, and these cells line parallel to the side of the fluid layer near the lateral wall. Near the center of the fluid layer, however, roll cells lose a directional character and meander complexly. Furthermore, some polygonal cells appear in the fluid layer and these cells may be caused by the thicker fluid layer than in conventional apparatus. Figure 6 is the phase diagram of Rayleigh-Bénard convection drawn by Krishnamurti [36]. Regarding this diagram, in the present apparatus, roll cells appear in the range of Rayleigh numbers indicated on the diagram with a red broken line. Experiments to observe a convective motion are carried out in this range.

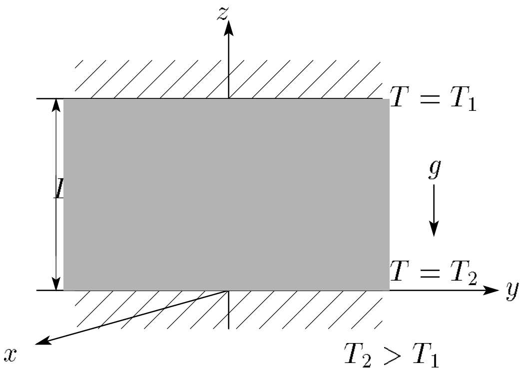

Figure 1: Coodinates and main symbols for mixed convection, internal heat generation $H$ is constant, and bottom temperature $T_2$ is larger than $T_1$.

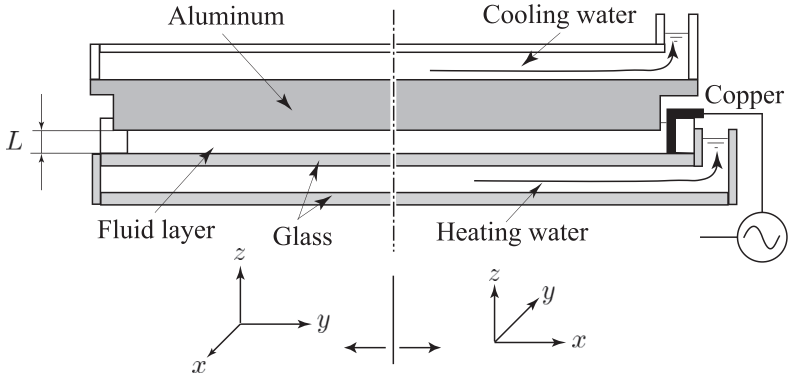

Figure 2: Schematic illustration of experimental apparatus, left part shows $y - z$ cross section and right part $z - x$ cross section.

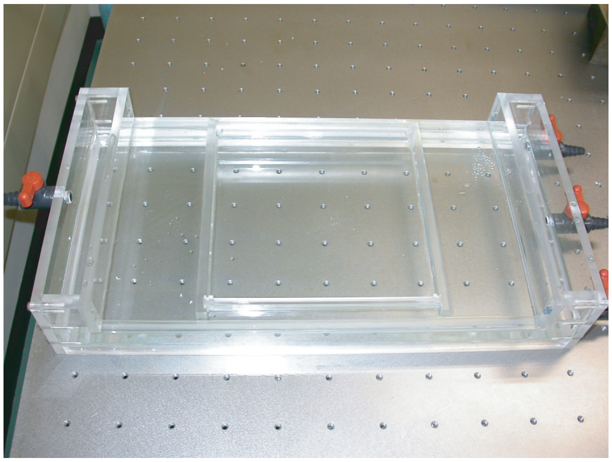

Figure 3: Photograph of heating plate with channel for heating water.

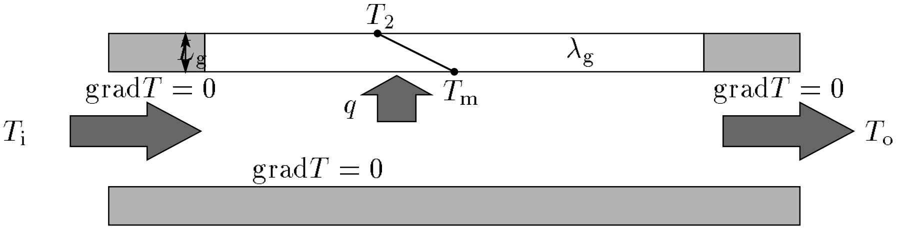

Figure 4: Schematic illustration for model of heat transfer at the bottom boundary of the fluid layer.

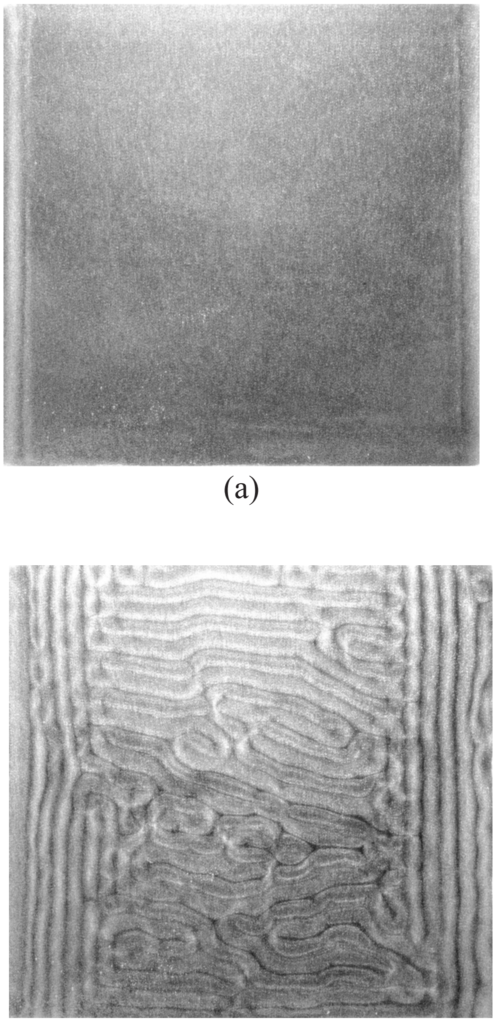

(a)

(b)

Figure 5: Visualized photographs of convective motion generated by external heating at the bottom boundary: (a) $R/R_c \sim 0.9$, (b) $R/R_c \sim 2.4$

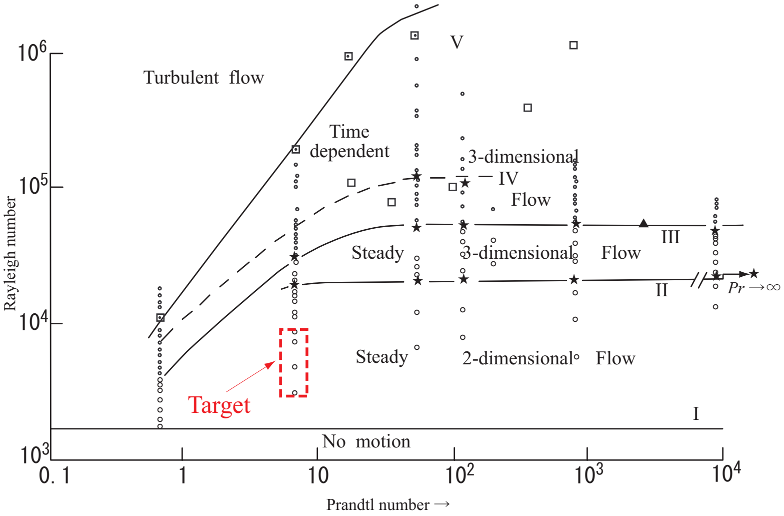

Figure 6: The régime diagram for Rayleigh-Bénard convection written by Krishnamurti [36].

## Results

### Convective flow pattern

Convective flow pattern of the mixed convection was observed for each condition of $R$ and $\Theta$ in order to make a flow regime by pattern formation. The pattern, however, depends on almost only $\Theta$ and can be classified to mainly three cases, $\Theta < 1$, $\Theta > 1$ and $\Theta \sim 1$.

### $\Theta < 1$

Figure 7(a) shows visualized photograph of roll pattern in pure Rayleigh-Bénard convection with $R = 4599$ ($R/R_{\mathrm{c}} = 2.69$). There are regular rolls overall the fluid layer. After roll pattern became stable, electric current was added to the fluid layer, where control parameters were $R_{\mathrm{I}} = 2024$ ($R_{\mathrm{I}}^{*} = 1.46$) and $\Theta = 0.45$. In this case, roll cells are not transformed by passing electric current as shown in Figure 7(b), and then rolls remain stably in the fluid layer under internal heating. For wide range of $R$, $1.4 \leq R/R_{\mathrm{c}} \leq 5$, an observation of the convective pattern showed the almost same result in the case until $\Theta \sim 1$.

As already mentioned in previous section, some polygonal cells appeared near the copper electrodes located at the both sides of the fluid layer for small $R$. Figure 8(a) is an example of such condition, $R = 6051$ ($R/R_{\mathrm{c}} = 3.54$). There are polygonal cells circled with a black line among regular rolls in the initial state without internal heating. These rolls may be produced by an influence of the copper electrodes and by negligibly large, initial perturbation. Figure 8(b) shows the convective pattern under internal heating with $\Theta = 0.55$. All rolls also remain stably in the fluid layer, and the polygonal cells circled with a yellow line remain in this condition. The cells circled with a red line, however, disappear by adding internal heat generation. In addition to this, a complexly meandering roll breaks up and reconnects with another roll various points on the fluid layer, and then these cells become more regular. From above observations, we concluded that adding weak internal heat generation, $\Theta < 1$, to Rayleigh-Bénard convection regularizes cells and a roll cell stably exists in this condition of internal heating. We call this region of $\Theta$ **Roll** region where a roll stably exists.

Figure 9(b) shows an enlarged image extracted from Figure 9(a), where the condition is $R = 8539$ ($R/R_{\mathrm{c}} = 5.00$). Figure 9(c) shows the enlarged image of the roll cell under internal heating with $\Theta = 0.80$. Comparing with both images, cell shape is similar, but thickness of roll in the case with internal heating is smaller than in pure Rayleigh-Bénard convection, namely wavenumber of a roll increases with internal heat generation. This observation is parallel to internally heated convection without wall heating in which wavenumber of a roll cell increases with respect to internal heat generation. As already mentioned in Introduction, critical wavenumber in linear theory increases with respect to $\Theta$ for $\Theta > 1$, however, for $\Theta < 1$, does not vary. The reduction of cell size observed in this investigation may be induced by a non-linear effect and may increase heat transport.

### $\Theta > 1$

If internal heat generation becomes significantly large beyond $\Theta = 1$, rolls dramatically changes in contrast with case of $\Theta < 1$ in which a roll is stable. Figure 10 shows a process of the change of a cell shape, where conditions are $R = 8539$ ($R/R_c = 5.00$) and $\Theta = 1.20$. Figure 10(a) shows pure Rayleigh-Bénard convection and roll exist overall the fluid layer. After adding internal heat generation setting $\Theta = 1.20$, rolls cannot exist stably and break up into small pieces. The peaces combine with other peace and are transformed into a polygonal cell as shown in Figure 10(b) and (c). This process of the transform is repeated and finally, polygonal cells prevail over the fluid layer (Figure 10(d)). Almost all of these polygonal cells are irregular hexagonal cell with descending flow at the center of the cell (HD) and this pattern is similar to the internally heated convection without wall heating at the bottom as mentioned in Chapter 3 and 4. The observation indicates that stability of the convective motion is changed from roll cell into HD, and critical value of $\Theta$ for the bifurcation exist near $\Theta = 1$ but slightly larger. For other cases of $R$, similar results are obtained by observation although a critical value of $\Theta$ deviates. We call this region of $\Theta$ **HD** region where HD stably exists in the fluid layer.

### $\Theta \sim 1$

The state of the convection does not change suddenly into another state, but it proceeds gradually, and thus, there is a transition state from **Roll** to **HD** region. In the observations of the convective pattern, cases with $\Theta \sim 1$, approximately $0.9 < \Theta < 1.1$, cannot be classified to either cases mentioned above, namely there are some kinds of shape of convection cell such as roll and HD in the fluid layer. This region of $\Theta$, in which various shapes be coexisted, may be classified as the transition region from **Roll** to **HD** region. In this region, a roll certainly changes into HD through a process. But there are different processes and initial condition appears to determine which process will be selected preferentially.

Figure 11(a) to (c) shows change of a roll in this transition region, where $R = 4599$ ($R/R_\mathrm{c} = 2.69$) and $\Theta = 0.63$, 0.95, 1.03 respectively. At first, a black band appears on a roll and a cell separate at this position. Straight part of a roll remains for some time, but a curved part rapidly changes into a polygonal cell as circled with red line in figures. Such a curved part may have lower stability and is easy to become a polygonal cell. A polygonal cell formed from a curved part of a roll, however, does not always become HD directly, also becomes an irregular hexagonal cell with ascending flow at the center of the cell (HU). Selection of circulatiion direction depends on the direction of the original roll (Figure 11(d)). A remaining roll and HU gradually change into HD with increase of $\Theta$ through a process of breakup and deformation, and finally, almost all cells become HD when $\Theta$ increases well over $\Theta = 1$. In this region near $\Theta = 1$, these are cells with several shapes, which are roll, polygonal cell including HD and HU, and then we call this region **Mixture** region.

### Phase diagram

Convective flow pattern can be classified into three cases as mentioned in the last section, namely roll for $\Theta < 1$, HD for $\Theta > 1$ and mixture of roll, HD and HU for $0.9 < \Theta < 1.1$. In this classification, however, boundaries of each ranges of $\Theta$ is not clear. In order to determine the ranges of $\Theta$ for each case, results of observation for various conditions of $R$ and $\Theta$ are classified into the three cases according to the following criterion.

| | |
|---|---|
| **Roll** | All roll remains stably. |
| **Mixture** | A polygonal cell including HD and HU appears. |
| **HD** | Almost all cell becomes HD. |

Figure 12 is a flow regime of pattern formation, where white, gray and black symbols express **Roll**, **Mixture** and **HD** respectively. By these symbols, the regime can be separated roughly to three regions by $\Theta = 0.8$ and $\Theta = 1.2$ expressed by the broken lines in the figure, and these values are unrelated to $R$. Therefore we concluded that the critical value of $\Theta$ for transition from **Roll** to **Mixture** state is 0.8 and the critical value for transition from **Mixture** to **HD** state is 1.2. They do not depend on $R$.

### Hysteresis

In the observation to make the flow regime, $R$ was fixed and $R_{\mathrm{I}}$ was increased to increase $\Theta$. We have studied whether convection state mentioned above depends on a history of changing direction of $\Theta$. As is shown in Figure 13, three cases are investigated, namely (A) $R_{\mathrm{I}}$ increases monotonically from **Roll** region to **HD** region, (B) $R_{\mathrm{I}}$ decreases until $\Theta < 0.8$, **Roll** region, after flow pattern reaches **HD** state, and (C) $R$ decreases to increase $\Theta$ from **Mixture** state to **HD** region. The case (A) is the same way to the previous observations. In the case (B), the flow pattern reaches **HD** state by increasing $R_{\mathrm{I}}$ (B1) and goes back to **Roll** state from **HD** state by decrease $R_{\mathrm{I}}$ (B2). In the case (C), the flow pattern becomes **Mixture** state by increasing $R_{\mathrm{I}}$ (C1), and becomes **HD** state by decreasing $R$ as an increase of $\Theta$. From these observations, the flow pattern does not depend on a history of changing $\Theta$ and on how to change $\Theta$. Therefore we concluded that there is no histeresys of the flow pattern formation in the mixed convection.

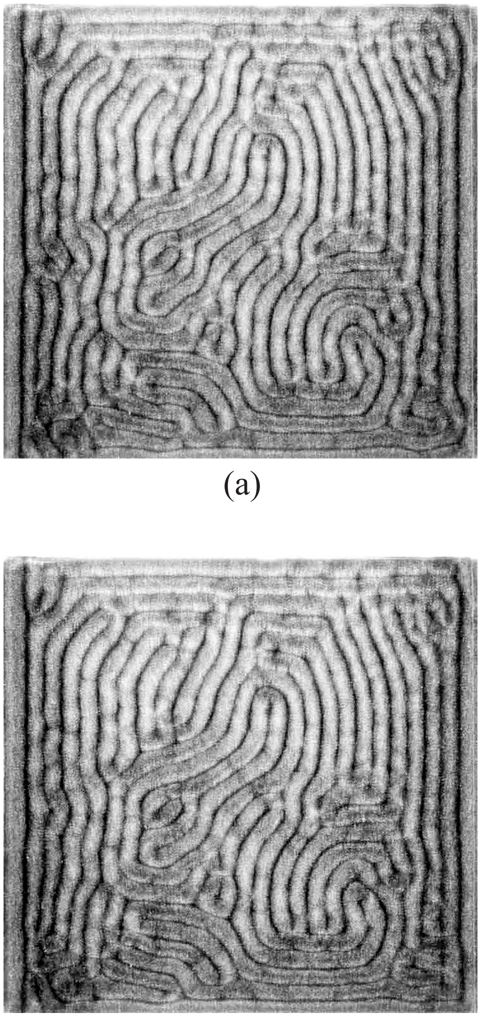

(a)

(b)

Figure 7: Convective flow pattern at $R/R_{\mathrm{c}} = 2.69$; (a) Pure Rayleigh-Bénard convection. (b) Adding internal heat generation with $\Theta = 0.45$.

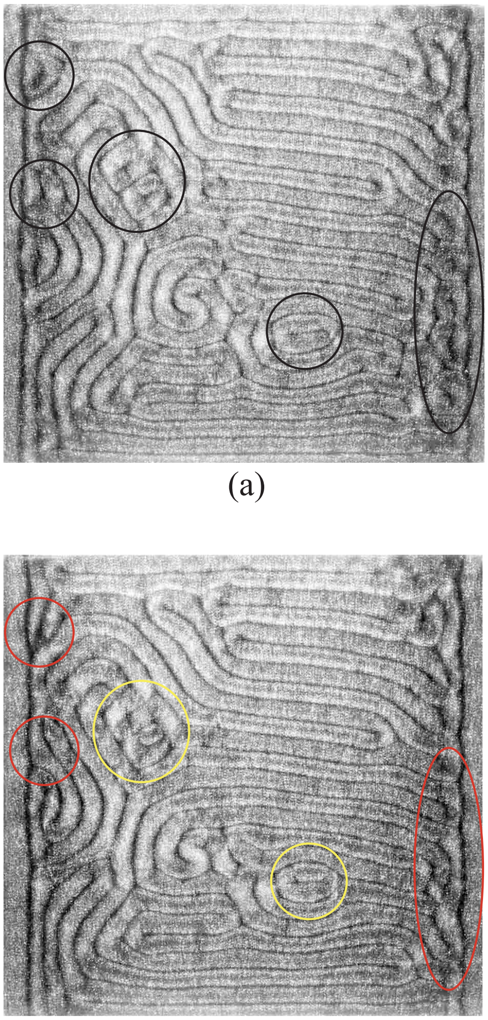

(a)

(b)

Figure 8: Convective flow pattern at $R/R_c = 3.54$; (a) Pure Rayleigh-Bénard convection. (b) Adding internal heat generation with $\Theta = 0.55$. Circles show polygonal cell produced by initial perturbation.

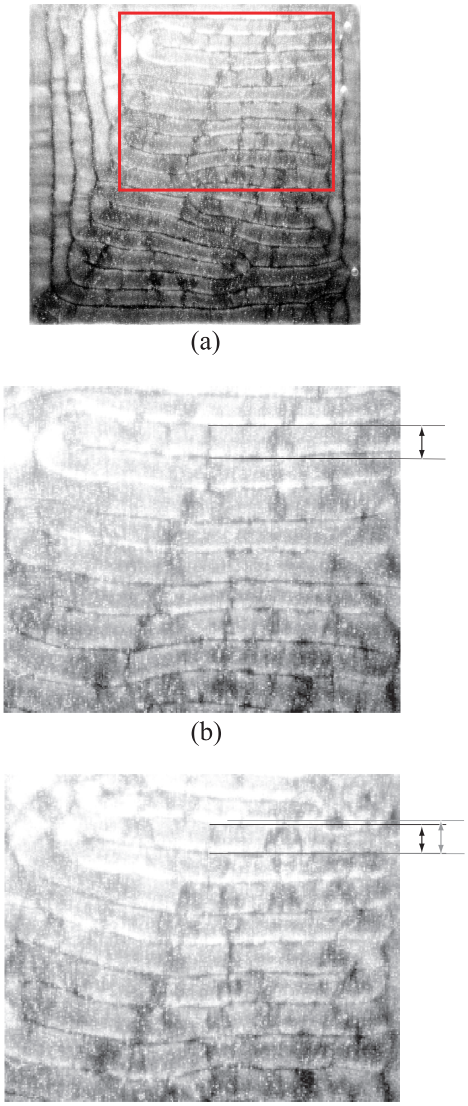

(a)

(b)

(c)

Figure 9: Decrease of cell size by internal heating; (a) Pure Rayleigh-Bénard convection at $R/R_{\mathrm{c}} = 5.00$. (b) Enlarged picture extracted from (a). (c) Adding internal heat generation with $\Theta = 0.80$.

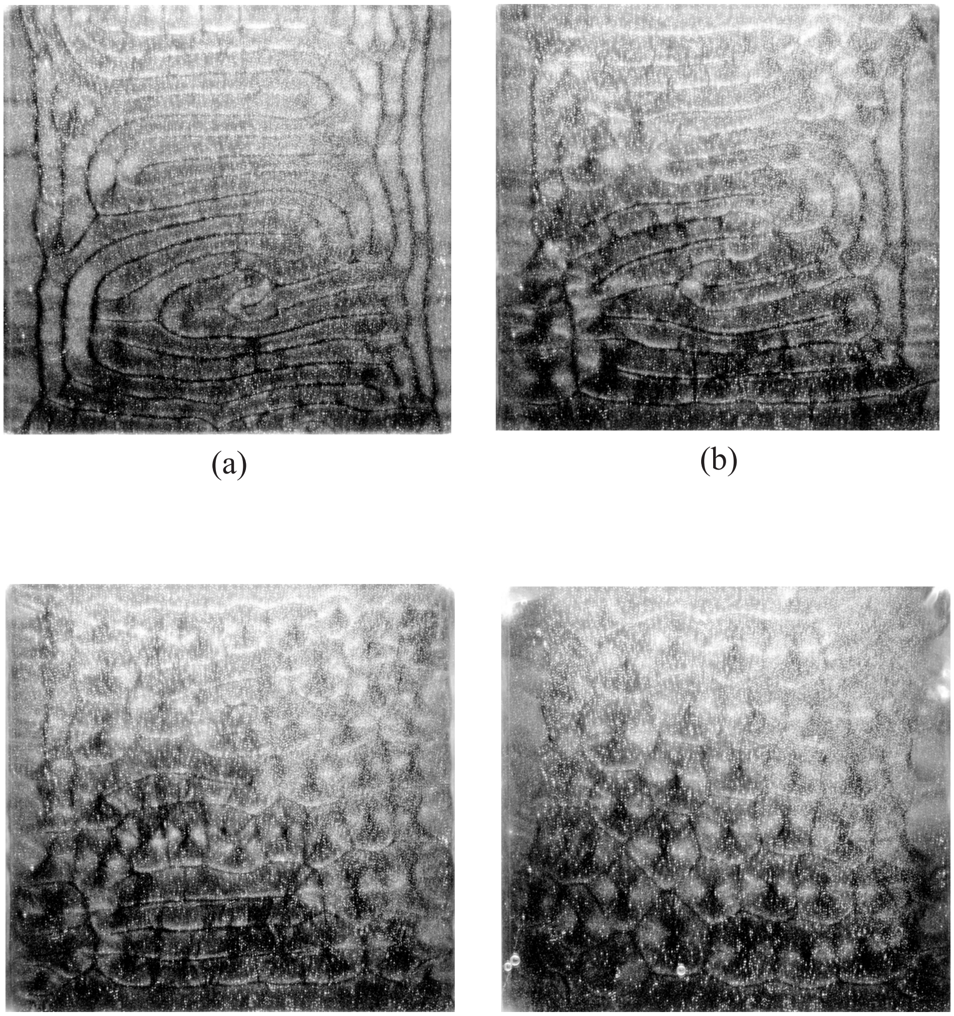

(a) (b)

(c) (d)

Figure 10: Time series showing a transition from roll cell to HD at $R/R_c = 5.00$. (a) Roll cells before internal heaeting. (b), (c) Transitional state.(d) Fully developed HD.

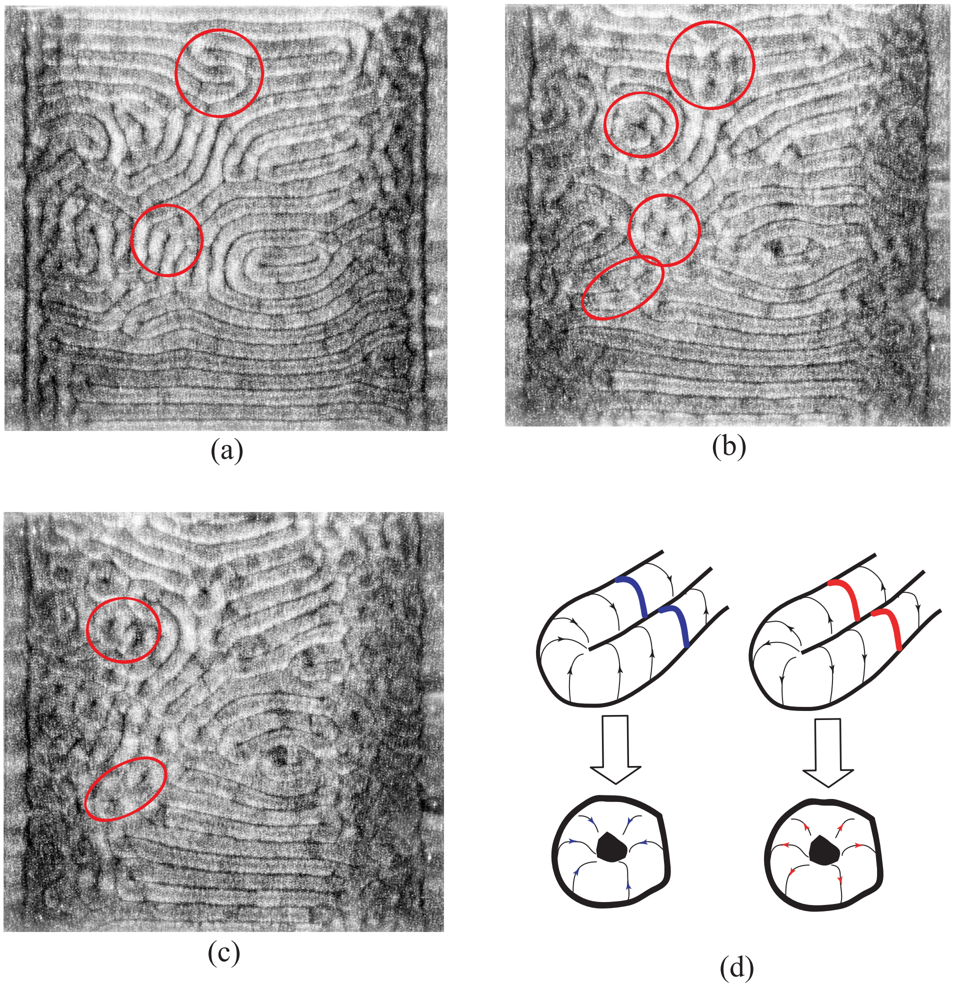

Figure 11: Detail of the transition from roll cell to HD at $R/R_c = 2.69$. (a)$\Theta = 0.63$, (b)$\Theta = 0.95$, (c)$\Theta = 1.03$. (d) Schematic illustration of transition from roll to HD and HU.

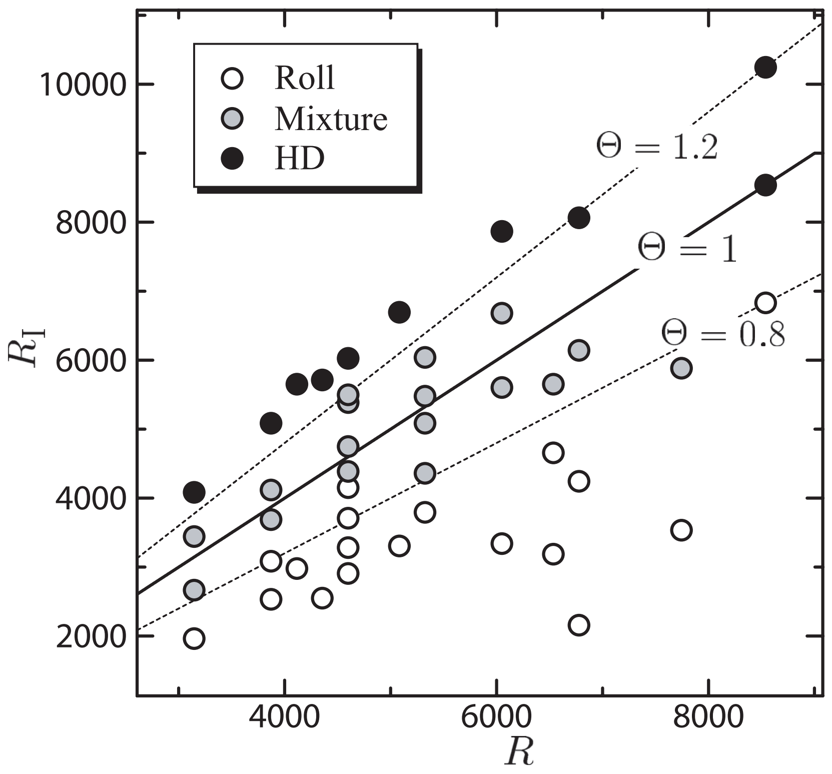

Figure 12: Regime of convective flow pattern determined by visual observation. Solid line shows $\Theta = 1$ and broken lines show $\Theta = 0.8$ and 1.2.

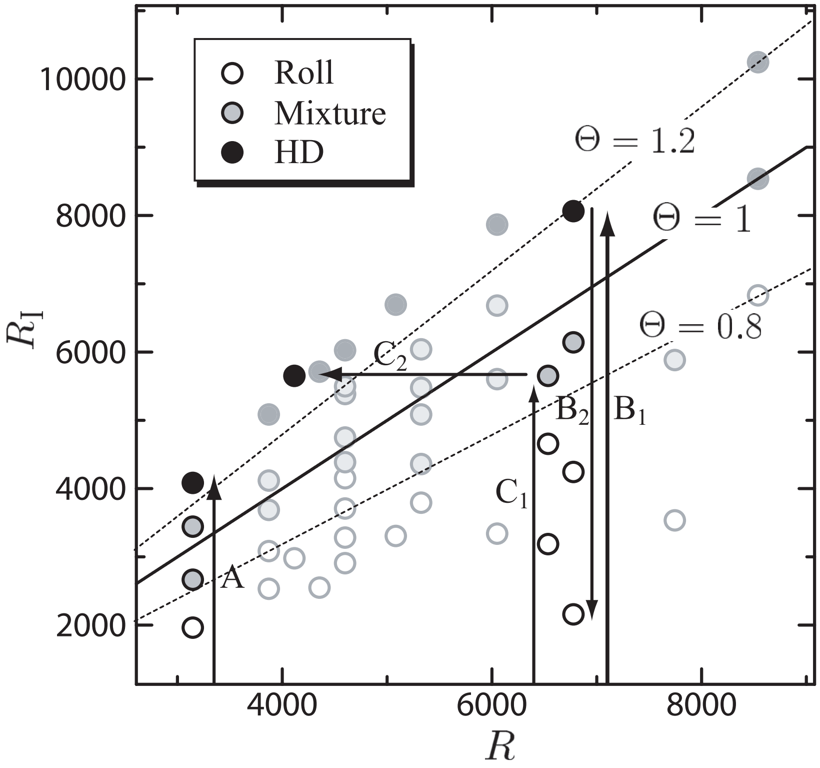

Figure 13: Transition of convective flow pattern along a path of changing $\Theta$.

# Appendix 2:
# Optimum Seeding for Velocity Profile Measurement by UVP

## Introduction

UVP (Ultrasonic Velocity Profiler [64]) is a powerful tool in the experimental fluid dynamics [65, 66] and the fluid engineering [67, 68] because it can measure an instantaneous velocity profile, and is applicable to a fluid flow of opaque liquid [67, 69]. The latter is a typical advantage in comparison with optical methods of velocity measurement such as PIV. Thanks to transmission property of ultrasound, UVP is applied in industries, for instance a flow metering in a large pipe [68] where a container wall is opaque, and a quality control in food processing [71, 72], in which fluid is generally opaque.

The measurement by UVP requires suspending a reflection particle in a flow. It is, however, less important when target flow velocity is sufficiently high. In this case, a small amount of impurity in liquid fully reflects an ultrasound pulse. In contrast to this, when target flow or measuring velocity component is extremely low, seeding a reflection particle in liquid becomes a serious problem because an error on velocity measurement by UVP strongly depends on particle flux through the measurement volume rather than concentration of the particle. However, if we mixed much amount of particles in liquid, substantial physical properties of liquid may change. In this paper, we attempted to find an optimum seeding for velocity measurement by UVP.

## Measurement volume and particle concentration

In velocity profile measurement by UVP, a measurement volume is like a disk and they are in a flow discretely arranged (Figure 14). The volume is determined by a pulse length (wavelength of ultrasound, cycles in a pulse) and an effective diameter of ultrasonic (US) burst.

Theoretically, if one or more reflection particle exists in the volume during the measurement, UVP can measure velocity at the volume. Assuming that one particle is in the measurement volume $V_{\mathrm{m}}$, concentration of particles in liquid $\gamma_{\mathrm{p}}$ becomes

$$\gamma_{\mathrm{p}} \simeq \frac{V_{\mathrm{p}}}{V_{\mathrm{m}}} = \frac{2d^3}{3WD^2}, \tag{3}$$

where $V_{\mathrm{p}}$ is a volume of the particle, $V_{\mathrm{p}} = \pi d^3/6$, and $d$, $D$, $W$ are a diameter of the particle, an effective diameter of US burst emitted from an US transducer, width of the measurement volume respectively. In the actual measurement system, $\gamma_{\mathrm{p}}$ is very small, which is approximately $10^{-3}$ %. This corresponds to 10 mg of particles for 1 $\ell$ water if particle has the same density with water. When fluid velocity is sufficiently high, required concentration of particles approaches this value. But if flow is slower, the required concentration strongly depends on velocity, namely enough amount of particle flux moving through the measurement volume is required. Particle flux, $f_{\mathrm{n}}$, which is the number of particle passing through the measurement volume per unit time, is given as

$$f_{\mathrm{n}} = \frac{\pi}{4} D^2 \gamma_{\mathrm{p}} U / V_{\mathrm{p}}, \tag{4}$$

where $U$ is velocity of fluid flow. The measurement requires that the particle flux $f_{\mathrm{n}}$ in a measurement time $\Delta t$ is larger than;

$$f_{\mathrm{n}} \Delta t \geq 1, \tag{5}$$

and then

$$\gamma_{\mathrm{p}} \geq \frac{2d^3}{3D^2 \Delta t} \frac{1}{U}. \tag{6}$$

As expressed in this inequality, required particle concentration $\gamma_{\mathrm{p}}$ is inversely proportional to the velocity.

## Experimental estimation of an optimum seeding

### Flow in a rotating cylinder

In order to estimate an optimum seeding, which is the minimum required particle concentration, we performed UVP measurement of a fluid flow in a rotating cylinder (Figure 15). This flow has been used for a calibration of UVP system. After enough time from start of the rotation, flow becomes rigid body motion, namely azimuthal velocity component $u_\theta$

becomes $u_\theta = r\omega$, where $r$ is radial position and $\omega$ is angular velocity of the cylinder. UVP can measure velocity component $u_x$ for the direction of propagating US burst $x$. When an US transducer is located outside of the cylinder parallel to the horizontal centerline of the cylinder with distance $\Delta y$, we can obtain a velocity profile in the cylinder along the measurement line as shown in Figure 15. Velocity does not depend on $x$ and the profile becomes constant, where the constant value is

$$u_x = \omega \Delta y. \tag{7}$$

This flow is basically steady for the constant rotating speed and the velocity profile measured by UVP also becomes constant temporally. Length of the measured velocity profile $L_x$ is determined as

$$L_x = \left(D_\mathrm{c}^2/4 - \Delta y^2\right)^{1/2}, \tag{8}$$

where $D_\mathrm{c}$ is an inner diameter of the cylinder.

### Experimental setup and measured velocity profile

Figure 16 shows an experimental setup for the measurement of the flow in the rotating cylinder. 700 mm × 700 mm acrylic bath is filled with water. A hollow acrylic cylinder, which has 150 mm outer diameter, 2.5 mm thickness and 50 mm height, is located at the center of the bath and is rotated by a motor with constant rotating speed. An US transducer with 4 MHz basic frequency is placed outside the cylinder with a few mm gap from the wall of the cylinder and its setting height is middle height of the cylinder. Nylon powder with diameter $d$ = 50 $\mu$m was used as reflection particle of US burst and its specific gravity is 1.06. In order to balance specific gravity of working fluid with that of the particle, 23 wt % glycerol solution was chosen as the fluid. Sound speed of the solution measured by time of flight method is 1601 m/s. Specifications of the measurement condition for the calculation of the measurement volume is given in Table 3.

Figure 17 shows a temporally averaged velocity profile of the flow in the rotating cylinder measured by UVP, UVP monitor Model UVP-Duo (Met-Flow S. A.), where $\Delta y$ and $\omega$ are 20 mm and 4.20 rad/s respectively. A solid line in the figure expresses the theoretical velocity profile, where $u_x$ is calculated by substituting $\omega$ and $\Delta y$ into Equation (7) and the side boundaries of the profile is determined by the inner diameter of the cylinder $D_\mathrm{c}$ and $\Delta y$

according to Equation (8). In comparison between both profiles, the measured profile is pretty much the same as the theoretical profile although it has slight deviation near the far sidewall boundary.

### Experimental estimation of an optimum seeding

As expressed in Equation (6), velocity can be measured by UVP when $\gamma_{\mathrm{p}}U$ is larger than a constant value which depends on measuring volume, particle size and measuring time. We investigate to find a necessary and sufficient value of $\gamma_{\mathrm{p}}U$ by estimating error of measurement at several conditions of $U$ and $\gamma_{\mathrm{p}}$. Figure 18(a) shows an instantaneous velocity profile measured in high particle concentration ($\gamma_{\mathrm{p}} = 0.02$). As shown in this figure, deviation of the profile is small and measured velocity is nearly constant inside the cylinder as predicted by the theory. In comparison with this, the profile measured in insufficient particle concentration (Figure 18(b)) has large deviation. Error caused by insufficient particle is defined as follows. UVP repeats emission and reception of ultrasound with several times in order to take an instantaneous velocity profile (repetition number is 32 in this measurement). Insufficient particle causes error on measured value and the error appears in the profile as deviation. Furthermore, if there is no particle in the measurement volume during measurement, a measured velocity becomes zero. In this estimation, velocity, which is smaller than ten times velocity resolution of the measurement, is attributed an error caused by insufficiency of the particle. The number of spatial sampling points for the estimation is 20 in the range of $x = 40 \sim 70$ mm by taking into account and divergence of US beam with respect to distance from an US transducer and deviation near the lateral wall. The number of profiles is 512 so that a total sampling number is about 10 000.

The error is estimated for many cases for $\gamma_{\mathrm{p}} = 0.002 \sim 0.05$ % and $w = 1.0 \sim 7.2$ rad/s. Figure 19 shows the result of the estimation of the error rate. The horizontal axis and the vertical axis in the figure represent particle flux through the measurement volume $\gamma_{\mathrm{p}}U_{\mathrm{m}}$ and error rate respectively, where $U_{\mathrm{m}}$ is temporal and spatial average of measured velocity $u_x$. $\gamma_{\mathrm{p}}$ can be converted into averaged number of particle in the measurement volume $n_{\mathrm{p}}$ and it is shown with $\gamma_{\mathrm{p}}$ in the legend, and then $\gamma_{\mathrm{p}}U_{\mathrm{m}}$ can be also converted into particle number flux $n_{\mathrm{p}}U_{\mathrm{m}}$. Results for different $\gamma_{\mathrm{p}}$ have similar trend, i.e. error rate monotonically decreases with respect to $\gamma_{\mathrm{p}}U_{\mathrm{m}}$. A solid line shows an approximate line of data by least square approximation. Slope of this line on the log-log plot is -1.1 and then measurement error decreases inversely proportional to $\gamma_{\mathrm{p}} U_{\mathrm{m}}$. Optimum seeding may be determined from this relation. For instance, in order to keep a measurement deviation below 0.1 %, $\gamma_{\mathrm{p}} U_{\mathrm{m}}$ must be set larger than 1 mm/s. In another expression, particle number flux must be set over 1700 mm/s.

## Conclusion

In order to estimate an optimum seeding of reflection particle on UVP measurement, we measured velocity profile in the rotating cylinder and estimated error caused by lack of the reflection particle for various cases of particle concentration $\gamma_{\mathrm{p}}$ and velocity $U$. The error rate depends on the particle flux through the measurement volume $\gamma_{\mathrm{p}} U$ and decreases inversely proportional to $\gamma_{\mathrm{p}} U$. An optimum seeding might be estimated based on this relation. For instance, we need 0.1 % of the particle concentration when a target velocity of the UVP measurement is few mm/s.

Table 3: Specifications of measurement condition.

| | Symbol | Unit | Value |
|---|---|---|---|
| Sound speed in glycerol solution | $c$ | m/s | 1601 |
| US burst | | | |
| Basic frequency | $f$ | MHz | 4 |
| Number of cycles | $N$ | | 4 |
| Effective diameter | $D$ | mm | 5 |
| Width of measurement volume | $W$ | mm | 0.801 |
| Diameter of particle | $d$ | $\mu$m | 50 |

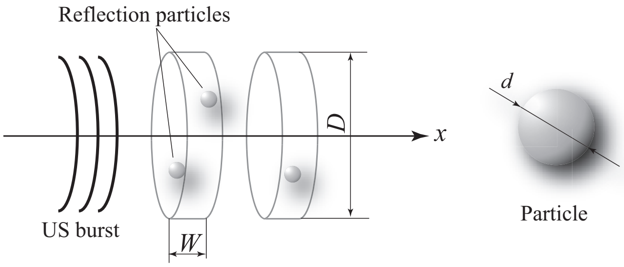

Figure 14: Schematic illustration of measurement volume and reflection particle, where disk-form measurement volumes exist along the measurement direction $x$ discretely.

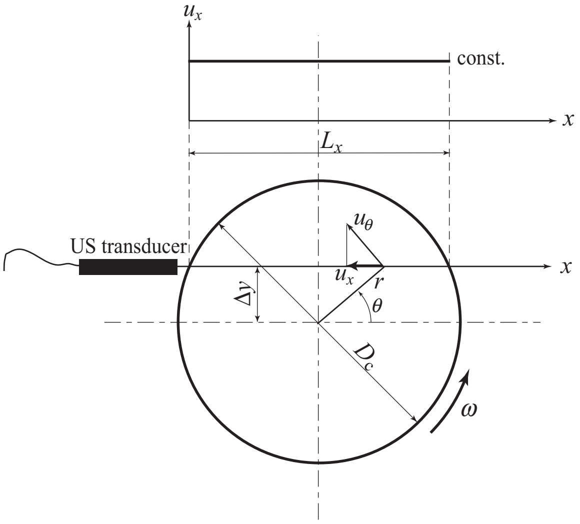

Figure 15: Schematic sketch of the flow in the rotating cylinder with angular velocity $\omega$ and a measured velocity profile, where the inside of the circle is filled with liquid.

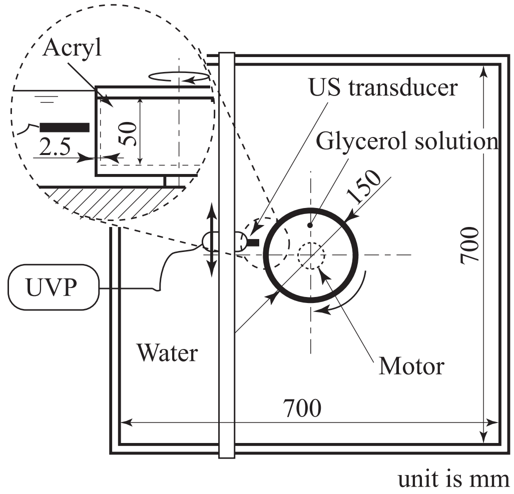

Figure 16: Schematic illustration of experimental setup, which is mainly consist of outer bath and rotating cylinder located at the center of the bath.

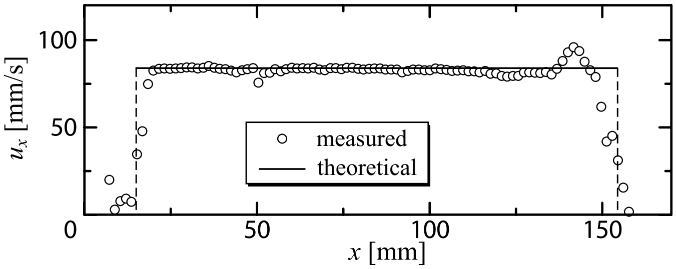

Figure 17: Temporally averaged velocity profile measured by UVP and theoretical profile, where setting velocity is 80 mm/s.

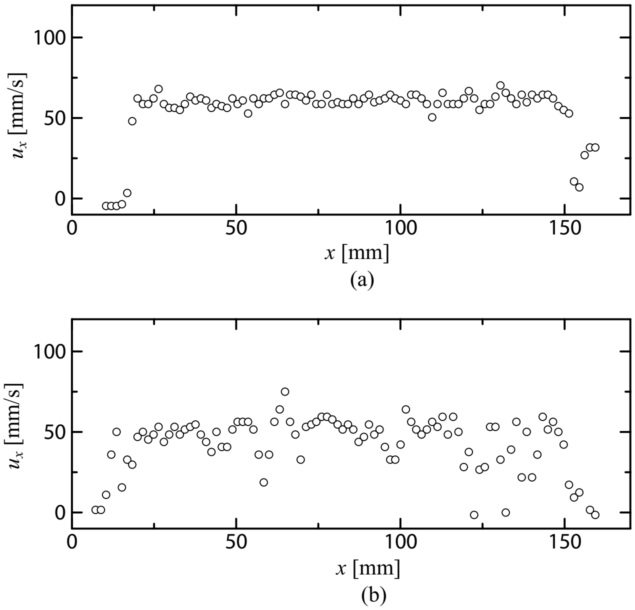

Figure 18: Measured velocity profile of the flow in the rotating cylinder by UVP (a) in rich particle concentration, $\gamma_{\mathrm{p}} = 0.02$, and (b) in poor concentration, $\gamma_{\mathrm{p}} = 0.004$.

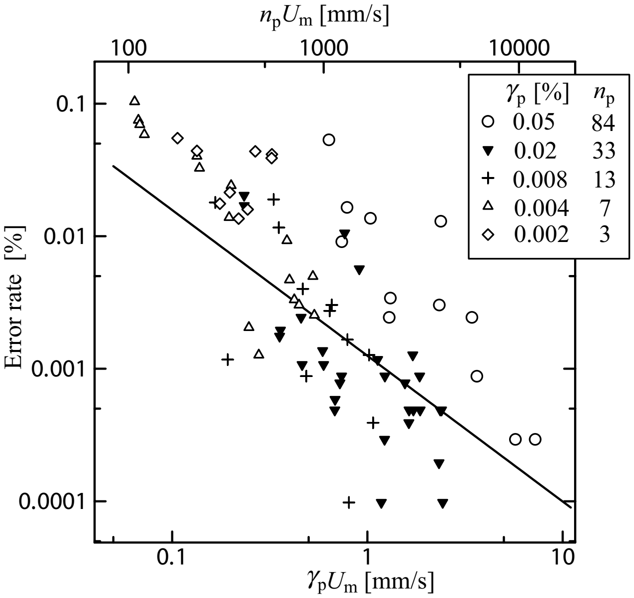

Figure 19: Error rate caused by lack of the particle versus particle flux through the measurement volume $\gamma_pU_m$ or particle for each particle concentration $\gamma_p$, where $n_pU_m$ represents particle number flux converted from $\gamma_pU_m$. Solid line represents approximate line of data calculated by least square approximation.

# Appendix 3:
# Sound Speed Measurement of Liquid Gallium

## Introducton

UVP (Ultrasonic Velocity Profiler [64]) achieves efficient mapping of flow field, then it has been used for the fluid dynamics, for example analysis of flow transition and weakly turbulent flow [65, 66]. Furthermore, UVP is applied to a high-precision flowmeter for a pipe flow substituting usual flowmeters, e.g. orifice flowmeter, electromagnetic flowmeter, etc, because it can measure flow in existing piping facilities [68]. The greatest advantage of UVP is to be able to measure a fluid flow of opaque liquid in the contrast to optical methods such as PIV. UVP is very useful as mentioned above, but it requires that sound speed of liquid and its temperature dependence are well known in order to measure flow with high accuracy.

Since gallium has conveniently low melting temperature (29.8 °C) and is relatively easy to deal with compared with other liquid metal, e.g. mercury and sodium, it has been used for a laboratory experiment of a flow of low Prandtl number liquid and a flow with liquid-solid phase change [59, 61, 63]. Its sound speed, however, is measured only at 30 °C near the melting point and that is insufficient on UVP measurement. In this paper, we develop a measurement system in order to determine a sound speed of various liquids accurately and investigate temperature dependence on sound speed of liquid gallium by using the developed system.

## Measurement method of sound speed

### Usual measurement method and its problem on accuracy

Generally, the Acoustic Time of Flight Measurement method (AtoM) [73] is used as a sound speed measurement. In this method, an ultrasonic (US) pulse is emitted from a US transducer located at one side of a liquid container to opposite side (Figure 20). An US pulse propagates in liquid and another transducer receives it with time delay $\Delta t$. If a propagation length L is already known, a sound speed of liquid, $c$, is given as $c = L/\Delta t$ by measuring $\Delta t$. The pulse-echo time of flight method [73], in which a receiving transducer is replaced with a reflector and a reflected pulse is received by the same transducer emitting a pulse, is also well used.

In this measurement principle, it is a premise to measure a sound speed accurately that the length of bath $L$ as the propagation length of the pulse was measured accurately. However, in fact, $L$ contains various errors which are hard to be estimated, e.g. deformation of the bath caused by temperature changing, in addition to errors at the making and the setup of the system. Thus this method is not best in a situation with temperature changing.

### Fundamental concept of present measurement method

As the aforementioned, a method of sound speed measurement based on a propagation length $L$ is not best owing to uncertainties caused by deformation of a bath. We propose a method of sound speed based on a moving length $\Delta l$ from an initial length L substituting the usual method. Measurements of a time of flight $\Delta t$ at various values of $l$, $l = L + \Delta l$, gives us a relationship $l - \Delta t$ as shown in Figure 21(a), where an approximated line is given by a least square approximation. Sound speed $c$ is a function of temperature $T$, and is given as a gradient of a function $l$, $l(\Delta t, T) = c(T)\Delta t + L^*$. If $\Delta l$ can be changed accurately with sufficiently small error $\delta l$, it is not necessity to measure $L$ strictly. The intercept $L^*$ in the equation contains a measurement error A and an error $B(T)$ related to changing temperature $T$, which contains a deformation of a bath, in addition to $L$. In the usual method, as shown in Figure 21(b), an error caused by changing temperature on a measurement of $L$, $\delta L$, is represented as a temporal error $\delta t'$ on a measurement of time of flight, and sound speed $c$ is measured as $c'$ which contains the error. Such error is hard to be estimated comparison with a measurement error of time dt. On the other hand, in the present method, such error is confined into $L^*$ and does not influence to determine c which is a slope of a function. Therefore, present method may be effective to determine a temperature dependence of a sound speed in which changing temperature is necessary.

## Experimental setup

A measurement setup was constructed in order to realize the basic concept of the present method (Figure 22) and it consists of two acrylic cylinders labeled A and B, an US transducer located perpendicular to the bottom plate of the cylinder A, a function generator and a digital oscilloscope. Figure 23 shows photographs of the experimental apparatus; (a) Exterior of the apparatus including the outer cylinder B, (b) The inner cylinder A and a reflector of an US pulse made with stainless steel as the bottom plate of the cylinder A. Two nozzles setting at the sidewall of the cylinder B are connected with the constant-temperature bath (AS-ONE, model CH-202). A slide unit with a micrometer is built on the acrylic rid of the cylinder B in order to move the transducer accurately on the vertical direction. A movable length of this unit is 13 mm and accuracy of movement is 10 $\mu$m. The reflector can be replaced easily by a flange located at the end of the cylinder. Acrylic reflector was also used in addition to the stainless steel one. Thickness of the both reflectors is 5 mm. Sample liquid filled the inner cylinder A and its temperature was kept constant by flowing water in the outer cylinder B. The temperature of the flowing water was controlled by the constant-temperature bath.

The pulse-echo time of flight method was used to measure a propagation time of an US pulse $\Delta t$. An US pulse generated by the US transducer with the function generator (Tabor, model 8551) is emitted to the reflector. The same transducer receives an US echo reflected from the surface of the reflector, and an oscilloscope (Iwatsu, model DS-8812) determines the propagation time $\Delta t$ by detecting the echo signal.

## Results

### Test measurement - sound speed measurement of water

A sound speed measurement of distilled water was performed as a test of the measurement system. A stainless steel reflector was used because of its high acoustic impedance related with a reflection rate. The function generator generated 3 cycles of a triangle like signal, where basic frequency and amplitude were 4 MHz and 10 V respectively. Bulk temperature of distilled water was 20.7 °C in this experiment. A transducer was moved with 0.5 mm intervals and a propagation time was measured by a digital oscilloscope at each position. In the present method, measuring a strict propagation time in which an US pulse propagates in a length of $2l$ is unnecessary and only **time difference** caused by movement of a transducer is important. Here, a propagation time was determined as time between pulse emission to a detection of a second top of a reflected echo signal which has triangle form, where a time resolution of the oscilloscope is 8 nsec.

Measurement result is shown in Figure 24, where each circle represents measured data and a line shown in the figure is an approximated line calculated by the least squire method. A sound speed calculated as a slope of the line is $c = 1479$ m/s, and it is well corresponding to measurement result at 20 °C, $c = 1483$ m/s.

### Sound speed measurement of liquid gallium

Dissipation of ultrasound in liquid gallium is larger than in water, and then amplitude of an US pulse was increased up to 16 V. Acoustic impedance in gallium is larger by 10 times as much as that in water. An acrylic US reflector, which has smaller acoustic impedance than stainless steel, was used in order to achieve sufficiently large reflection rate (A stainless steel reflector was also used but an echo signal is small.). Reflection rate for gallium is 0.44 in stainless steel and is 0.70 in acryl. Changing temperature range of gallium is 30 to 50 °C.

Figure 25 shows measurement result, where approximate line given by the measured values is $c(T) = -0.6163T + 2891.9$. Standard deviation of scatter of data is $\sigma = 3.403$. A sound speed of gallium shows a tendency to decrease generally with respect to temperature. A rate of decrease in gallium is comparable to that in mercury.

## Additional remarks for liquid gallium

Typical photographs taken in or after a measurement are shown in Figure 26. Following remarks don't have direct relation with a sound speed measurement but may be important in all experiment with using liquid gallium. Figure 26(a) shows the inner cylinder filled with liquid gallium, where gallium is covered with distilled water in order to prevent oxidation of gallium. There are many white patches at a surface of a column of liquid gallium. These are small bubbles generated from a thin water layer between gallium and the inner cylinder. Because gallium does not wet to acryl, such thin water layer appears at the interface. Gallium is very easy to be oxidized, and a gallium oxide will disturb a measurement of the sound speed. Therefore we paid attention removing these bubbles in the middle of experiment. Figure

26(b) and Figure 26(c) are respectively a stainless steel reflector and an US transducer after an experiment. White things put at the surfaces are oxides of gallium. Just gallium is hard to wet to something without metals, but its oxide is easy to stick at everything as shown in the figures.

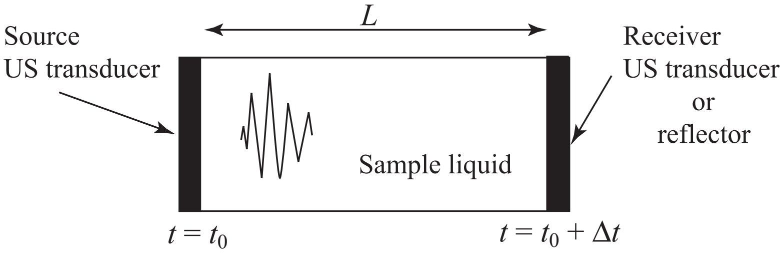

Figure 20: Diagram of sound speed measurement by AtoM method [73], where Dt represents time of fright of an ultrasonic pulse propagating in liquid with length L.

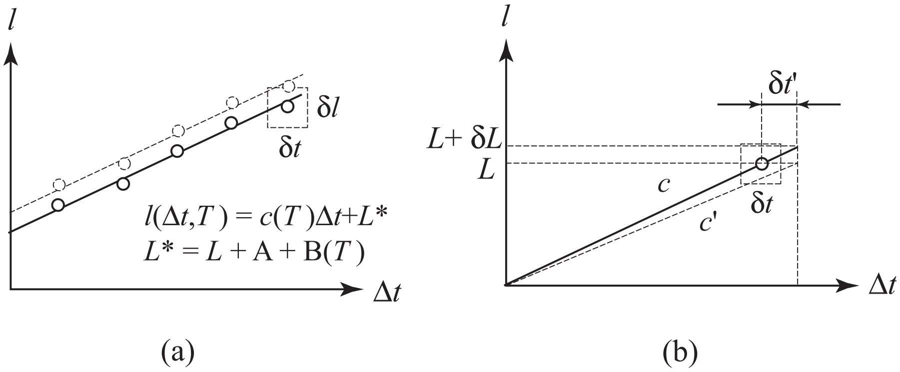

Figure 21: Schematic illustration of fundamental concept for (a) present method and (b) usual method, where $l$ and $\Delta t$ represent a propagation length and time of flight of ultrasound, $\delta t$ and $\delta l$ represent a measurement error of $\Delta t$ and $l$. Sound speed is determined as slope of a function $l(\Delta t)$.

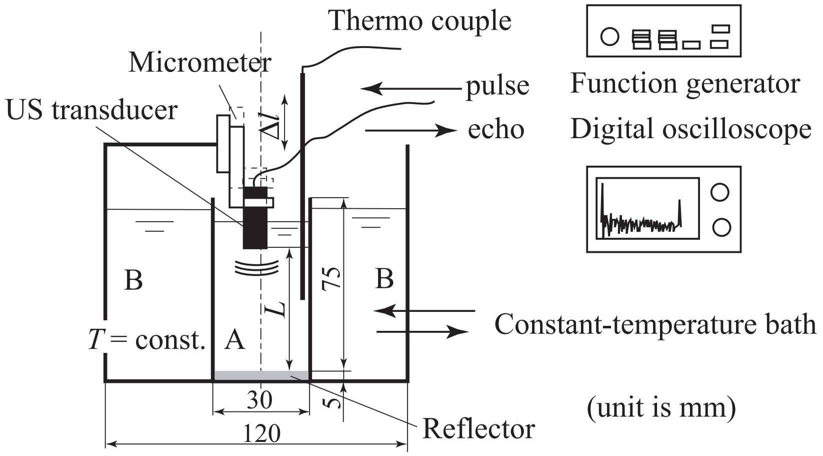

Figure 22: Schematic illustration of experimental setup that mainly consists of two cylinders, ultrasonic transducer, function generator, digital oscilloscope and constant-temperature bath.

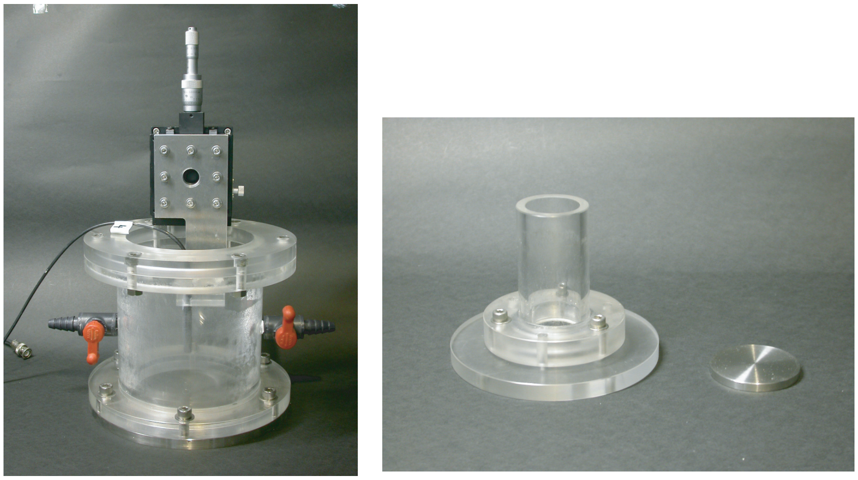

(a) (b)

Figure 23: Photographs of experimental apparatus; (a) Exterior, (b) Inner cylinder and reflector.

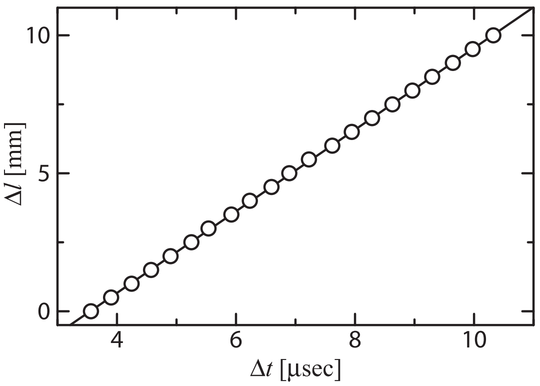

Figure 24: Result of sound speed measurement for distilled water.

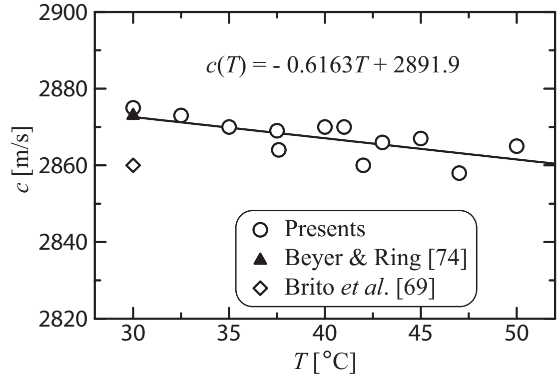

Figure 25: Temperature dependence of sound speed in liquid gallium.

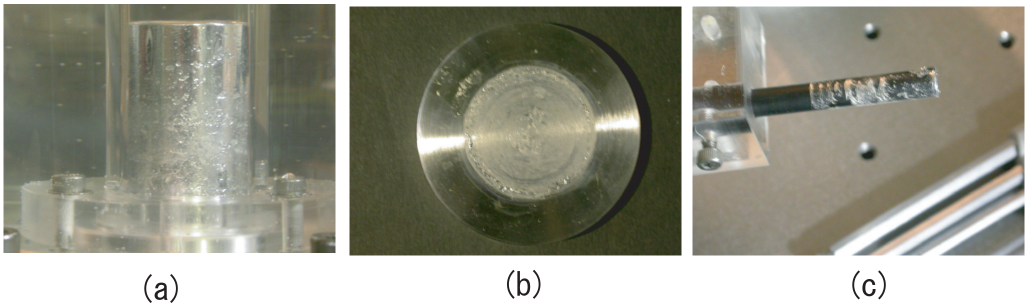

Figure 26: Typical photographs taken in or after a measurement, (a) Liquid gallium filled in inner cylinder, (b) Stainless steel reflector of ultrasonic pulse after measurement, (c) Ultrasonic transducer after measurement.

# Design of the apparatus

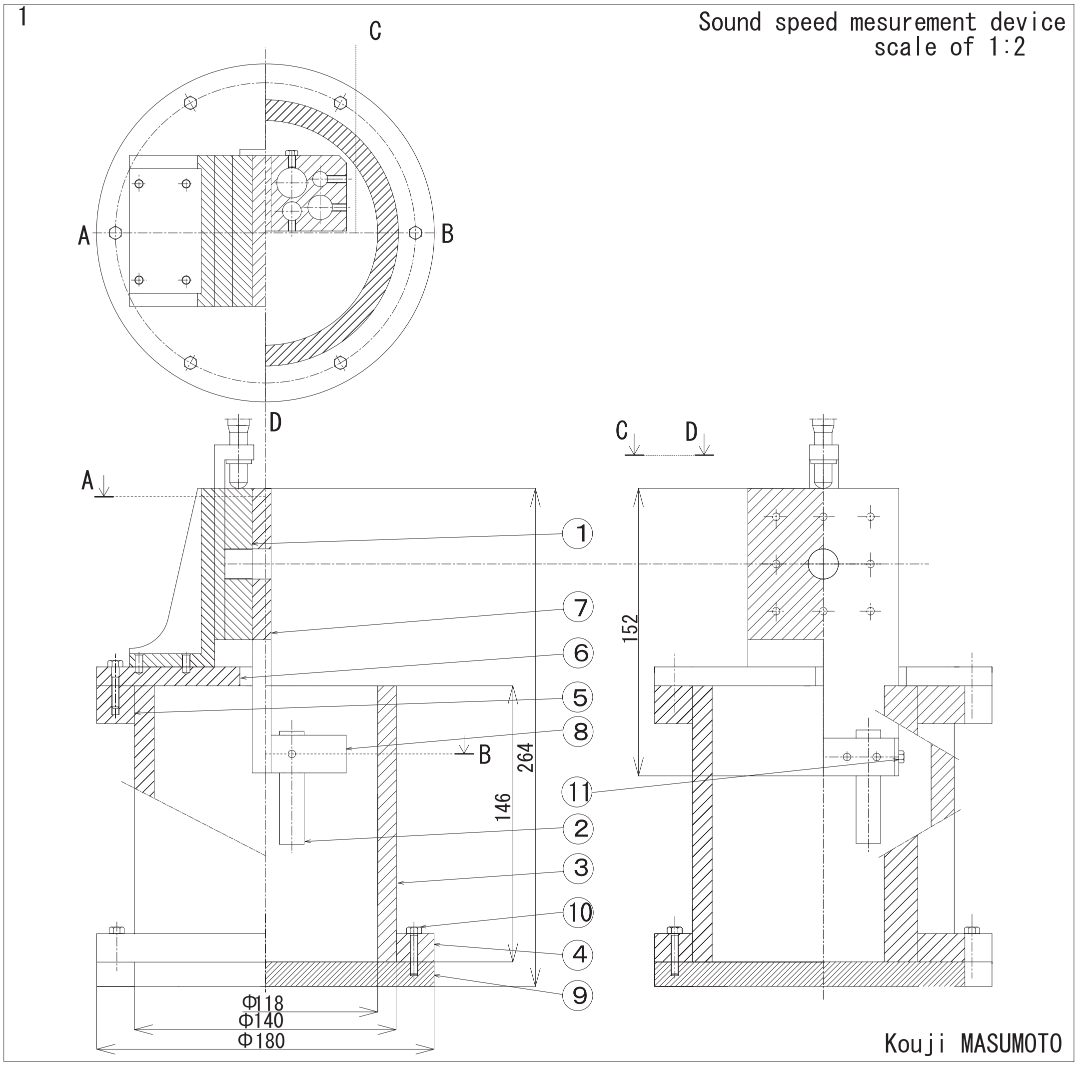

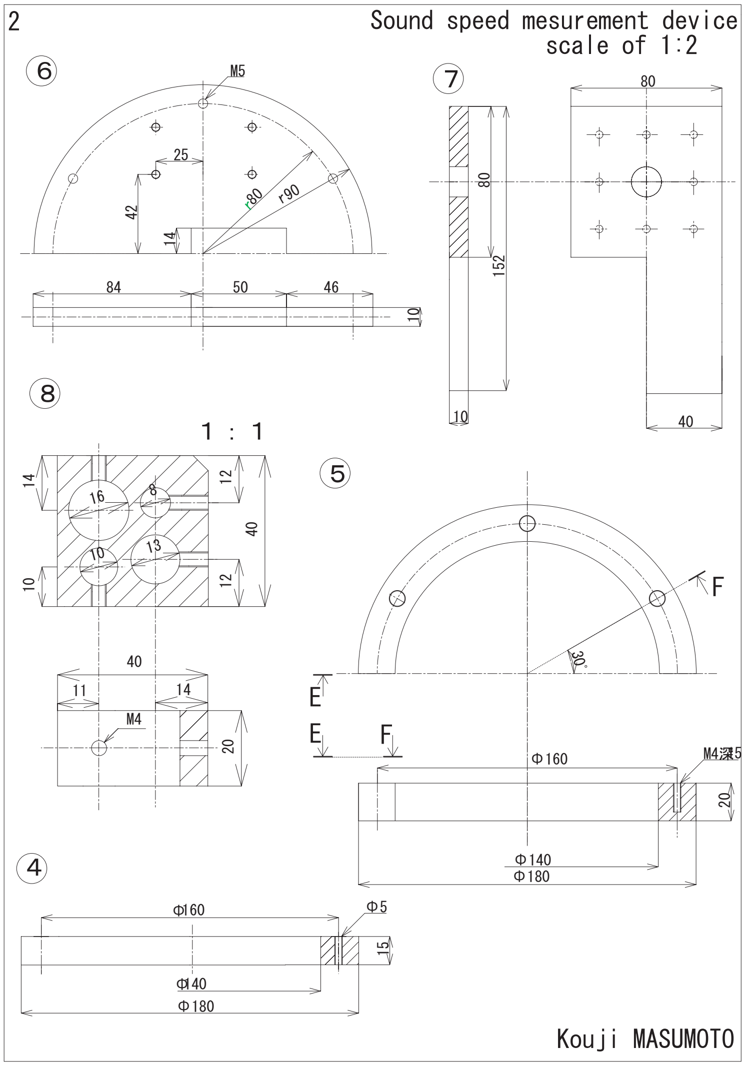
2
Sound speed mesurement device
scale of 1:2
⑥
M5
25
42
14
r80
r90
84
50
46
10
⑦
80
80
152
10
40
⑧
1 : 1
14
16
8
12
40
10
13
10
12
40
11
14
M4
20
⑤
F
30°
E
E
F
Φ160
M4深5
20
Φ140
Φ180
④
Φ160
Φ5
15
Φ140
Φ180
Kouji MASUMOTO

Sound speed mesurement device
scale of 1:2

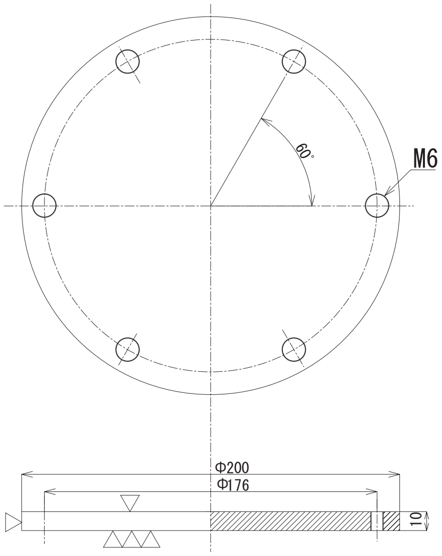

Kouji MASUMOTO

# Appendix 4:
# Visualized Photographs of Internally Heated Convection

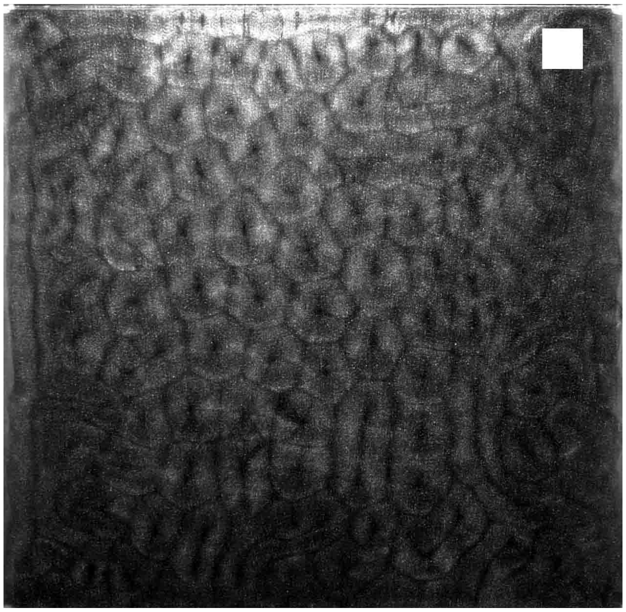

$R_I{}^* \sim 2$

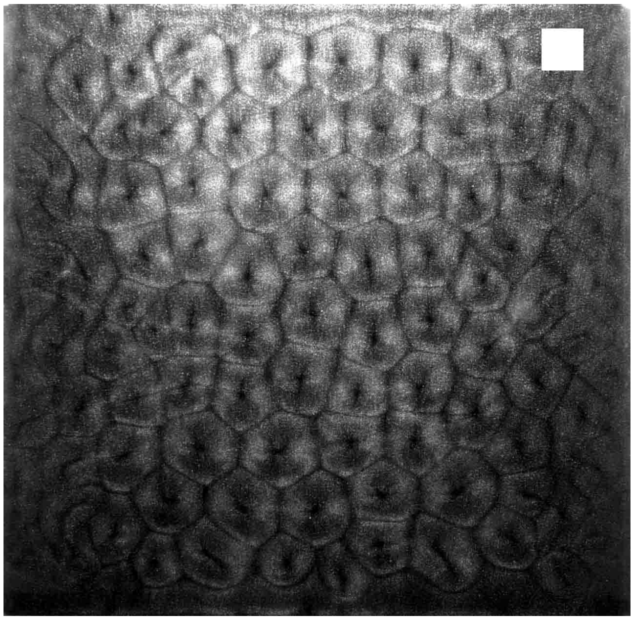

$R_I{}^* \sim 3$

Figure 27: Visualized flow pattern

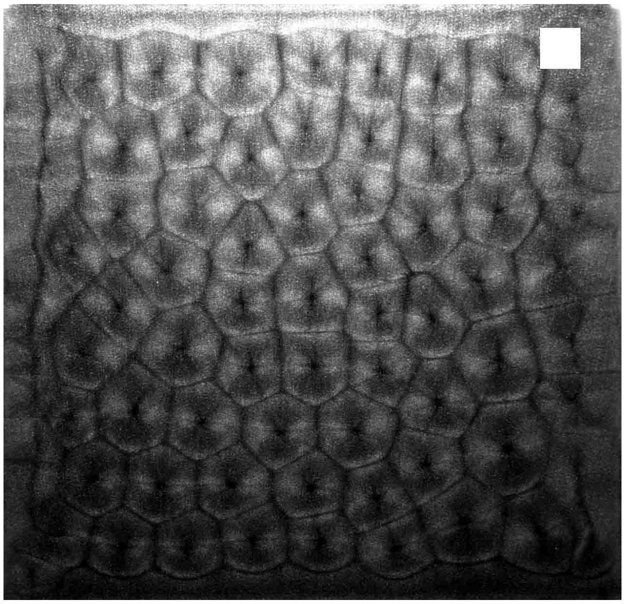

$R_I^* \sim 4$

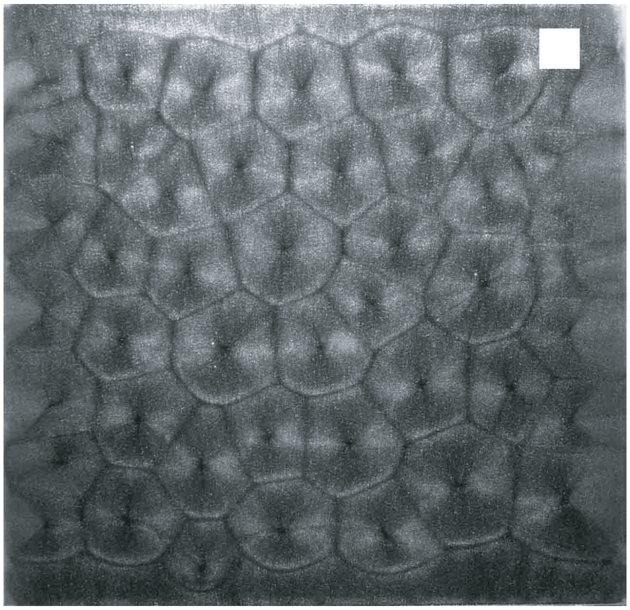

$R_I^* \sim 5$

Figure 27: Visualized flow pattern

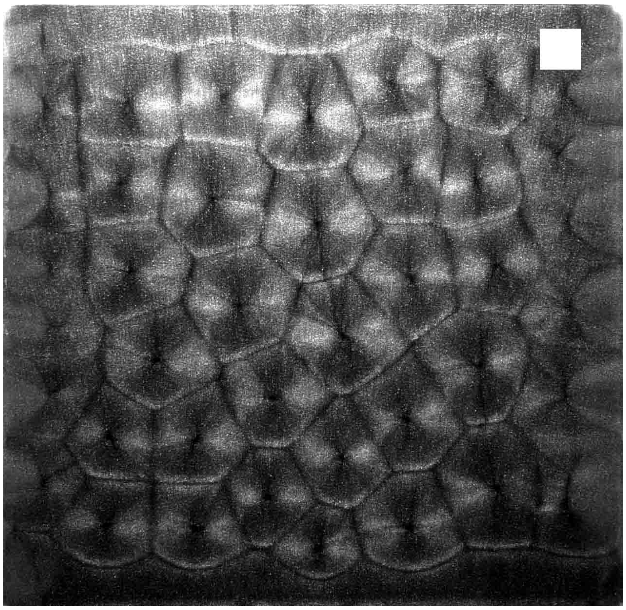

$R_{\mathrm{I}}* \sim 6$

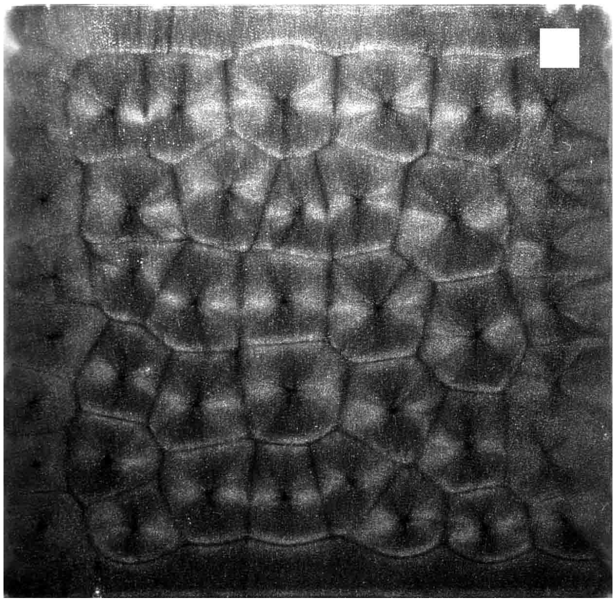

$R_{\mathrm{I}}* \sim 7$

Figure 27: Visualized flow pattern

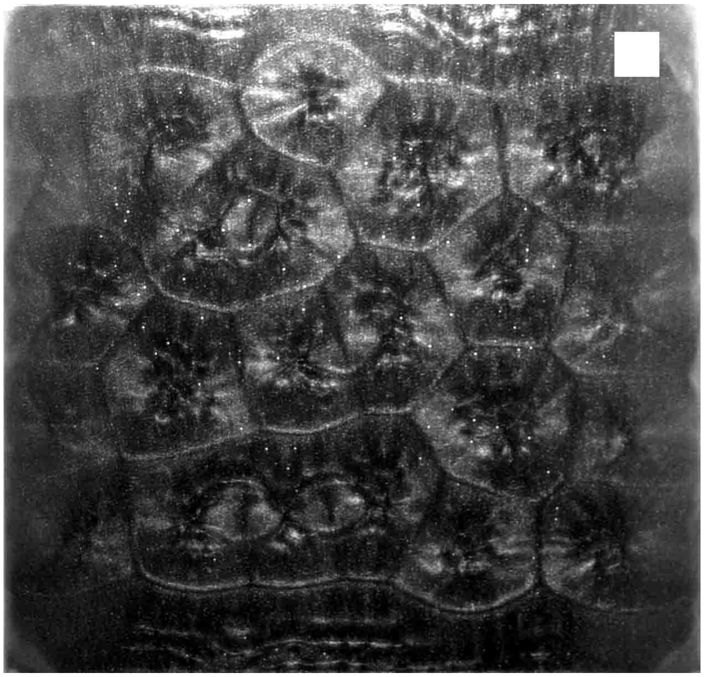

$R_I^* \sim 22$

Figure 27: Visualized flow pattern

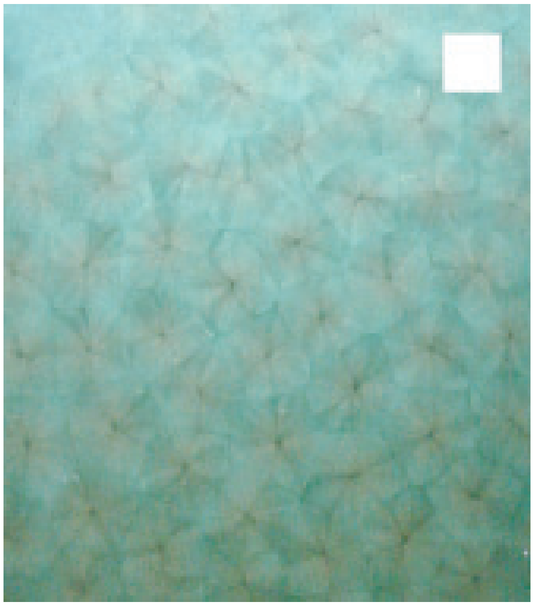

$R_I* \sim 1.7$

$R_I* \sim 3.2$

Figure 28: Visualized temperature field

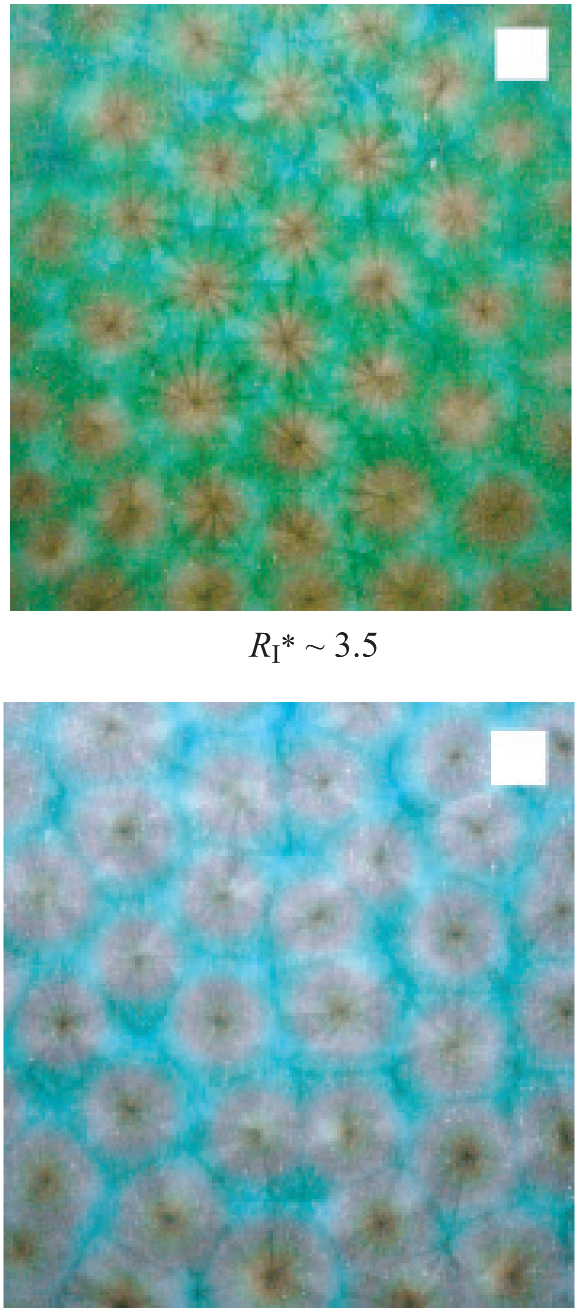

$R_I^* \sim 3.5$

$R_I^* \sim 4.2$

Figure 28: Visualized temperature field

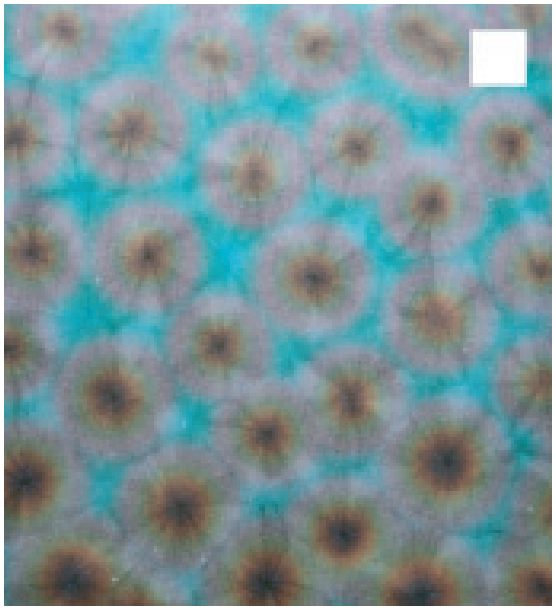

$R_I^* \sim 5.5$

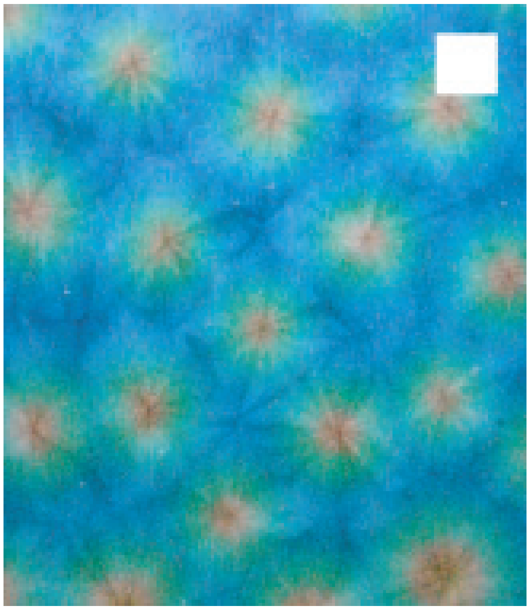

$R_I^* \sim 6.0$

Figure 28: Visualized temperature field

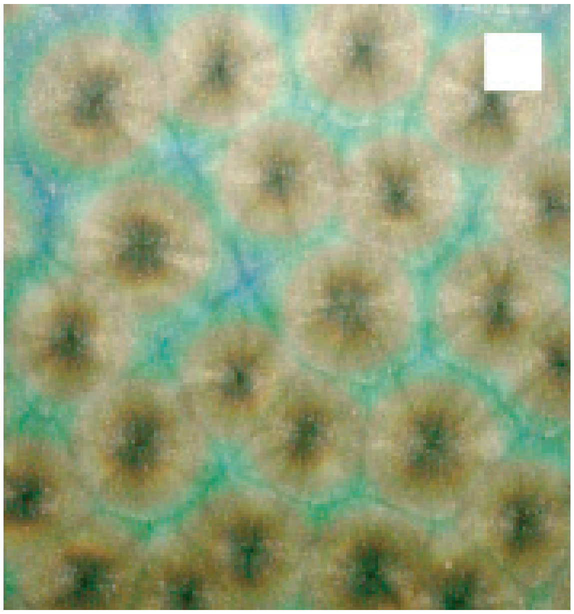

$R_I^* \sim 10.0$

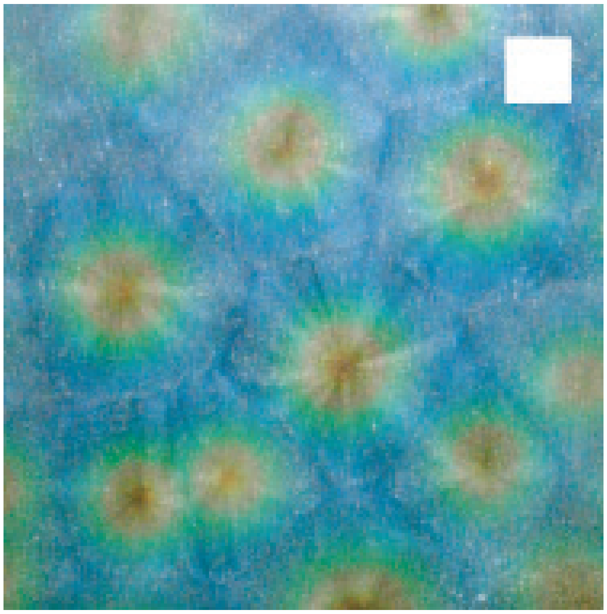

$R_I^* \sim 12.1$

Figure 28: Visualized temperature field

# References

[1] H. Bénard, "Les tourbillons cellulaires dans une nappe liquide", *Annales de chimie et de physique*, (1901), **23**, pp.62-144.

[2] Lord Rayleigh, "On convection currents in a horizontal layer of fluid when the higher temperature is on the under side", *Phil Mag*, (1916), **32**, pp.529-546.

[3] M. Golubitsky, J. W. Swift and E. Knobloch, "Symmetries and Pattern Selection in Rayleigh-Bénard Convection", *Physica D*, (1984), **10**, pp.249-276.

[4] S. Chandrasekhar, "Hydrodynamic and Hydromagnetic Stability", Oxford Univ. Press, (1961).

[5] H. T. Rossby, "A study of Bénard convection with and without rotation", *J. Fluid Mech.*, (1969), **36**, pp.309-338.

[6] M. J. Block, "Surface tension as the cause of Bénard cells and surface deformation in a liquid film", *Nature*, (1956), **178**, pp.650-651.

[7] J. R. A. Person, "On convection cells induced by surface tension", *J. Fluid Mech*, (1958), **4**, pp.489-500.

[8] E. L. Koschmieder, "Bénard Cells and Taylor Vortices", Cambridge Univ. Press, (1993).

[9] D. J. Tritton, "Internally heated convection in the atmosphere of Venus and in the laboratory", *Nature*, (1975), **257**, pp.110-112.

[10] A. Yücel and Y. Bayazitoglu, "Onset of Convection in Fluid Layers with Non-uniform Volumetric Energy Sources", *Trans. ASME, J. Heat Trans.*, (1979), **101**, pp.666-671.

[11] R. Krishnamurti, "Convection induced by selective absorption of radiation: A laboratory model of conditional instability", *Dynamics of Atmospheres and Oceans*, (1997), **27**, pp.367-382.

[12] D. P. Mckenzie, J. M. Roberts and N. O. Weiss, "Convection in the earth's mantle: toward a numerical simulation", *J. Fluid Mech.*, (1974), **62**, pp.465-538.

[13] D. L. Turcotte, J. Schubert and G. Schubert, "Geodynamics 2nd eddition", Cambridge Univ. Press, (2001).

[14] G. T. Jarvis, "Time-dependent convection in the Earth's mantle", *Phys. Earth Planet. Int.*, (1984), **36**, pp.305-327.

[15] G. Schubert, D. L. Turcotte, P. Olson, "Mantle Convection in the Earth and Planets", Cambridge Univ. Press, (2001).

[16] A. O. EL Moctar, H. Peerhossaini, J. P. Bardon, "Numerical and Experimental Investigation of Direct Electric Conduction in a Channel Flow", *Int. J. Heat & Mass Trans.*, (1996), **39**, pp.975-993.

[17] R. R. Nourgaliev, T. N. Dihn and B.R. Sehgal, "Simulation and analysis of transient cooldown natural convection experiments", *Nuc. Eng. & Design*, (1997), **178**, pp.13-27.

[18] M. S. Young and M. H. Jae, "Transient confined natural convection with internal heat generation", *Int. J. Heat & Fluid Flow*, (1997), **18**, pp.328-333.

[19] A. Liapat and A. C. Baytas, "Numerical comparison of conjugate and non-conjugate natural convection for internally heated semi-circular pools", *Int. J. Heat & Fluid Flow*, (2001), **22**, pp.650-656.

[20] T. Marimbordes, A. Ould EL Moctar and H. Peerhossaini, "Active control of natural convection in a fluid layer with volume heat dissipation", *Int. J. Heat & Mass Trans.*, (2002), **45**, pp.667-678.

[21] C. Sotin, S. Labrosse, "Three-dimensional thermal convection in an iso-viscous, infinite Prandtl number fluid heated from within and from below: applications to the transfer of heat through planetary mantles", *Phys. Earth Planet. Int.*, **112** (1999), pp.171-190.

[22] D. J. Tritton and M. N. Zarraga, "Convection in horizontal layers with internal heat generation : Experiments", *J. Fluid Mech.*, (1967), **30**, pp21-32.

[23] E. W. Schwiderski and H. J. A. Schwab, "Convection experiments with electrolytically heated fluid layers", *J. Fluid Mech.*, (1971), **48**, pp.703-719.

[24] C. R. Carrigan, "Multiple-Scale Convection in the Earth's Mantle: A Three-Dimensional Study", *Nature*, (1982), **215**, pp.965-967.

[25] C. R. Carrigan, "Convection in an Internally Heated, High Prandtl Number Fluid: A Laboratory Study", *Geophys. Astrophys. Fluid Dynamics*, (1985), **32**, pp.1-21.

[26] E. M. R. Sparrow, R. J. Goldstein and V. K. Jonsson, "Thermal instability in a horizontal fluid layer: effect of boundary conditions and non-linear temperature profile", *J. Fluid Mech.*, (1964), **18**, pp.513-528.

[27] P. H. Roberts, "Convection in horizontal layers with internal heat generation : theory", *J. Fluid Mech.*, (1967), **30**, pp.33-49.

[28] M. Tveitereid, E. Palm, "Convection due to internal heat sources", *J. Fluid Mech.*, (1976), **76**, pp.481-499.

[29] R. Thirby, "Convection in an internally heated layer", *J. Fluid Mech.*, (1970), **44**, pp.673-693.

[30] J. A. Whitehead and M. M. Chen, "Thermal instability and convection of a thin fluid layer bounded by a stratified region", *J. Fluid Mech.*, (1970), **40**, pp.549-**.

[31] K. Ukaji, "Thermal and Dynamical Structures of Convective Motions in a rotating Fluid Annulus Subject to Internal Heating", *J. Meteorological Society of Japan*, (1979), **57**, pp.532-547.

[32] P. L. Read, "Regimes of axisymetric flow in an internally heated rotating fluid", *J. Fluid Mech.*, (1986), **168**, pp.255-289.

[33] M. Tveitereid, "Thermal Convection in a Horizontal Fluid Layer with Internal Heat Sources", *Int. J. Heat Mass Trans.*, (1978), **21**, pp.335-339.

[34] S. A. Weinstein and P. Olson, "Planforms in thermal convection with internal heat sources at large Rayleigh and Prandtl numbers", *Geophys. Res. Lett.*, (1990), **17**, pp.239-242.

[35] B. Travis, S. Weinstein and P. Olson, "Three-dimensional convection planforms with internal heat generation", *Geophys. Res. Lett.*, (1990), **17**, pp.243-246.

[36] R. Krishnamurti, "On the transition to turbulent convection. Part 2. The transition to time-dependent flow", *J. Fluid Mech.*, (1970), **42**, pp.309-320.

[37] Y. Yamanaka, K Kakimoto, H. Ozoe, S. W. Churchill, "Rayleigh-Bénard oscillatory natural convection of liquid gallium heated from below", *Chemical Eng. J.*, (1998), **71**, pp.201-205.

[38] W. H. Reid and D. L. Harris, "Some further results on the Bénard problem", *Phys. Fluids*, (1958), **1**, pp.102-110.

[39] F. A. Kulacki and R. J. Goldstein, "Hydrodynamic Instability in Fluid Layers with Uniform Volumetric Energy Sources", *Appl. Scientific Res.*, (1975), **31**, pp.81-109.

[40] W. J. Hiller and T. A. Kowalewski, "Simultaneous measurement of temperature and velocity field in thermal convective flows", *Proc. 4th Int. Symposium Flow Visualization*, (1986), pp.617-622.

[41] C. D. Richards and R. F. Richards, "Transient temperature measurements in a convectively cooled droplet", *Exp. in Fluids*, (1998), **25**, pp.392-400.

[42] D. G. Christopherson, "Note on the vibration of membranes", *Quart. J. Math. (Oxford series)*, (1940), **11**, 63.

[43] Kalliroscope Co, Ltd., http://www.kalliroscope.com/.

[44] K. Park, G. L. Grawford, R. J. Donnelly, "Determination of transition in Couette flow in finite geometries", *Phys. Rev. Lett.*, (1981), **47**, pp.1448-1450.

[45] P. Matisse, M. Gorman, "Neutrally buoyant anisotropic particles for flow visualization", *Phys. Fluids*, (1984), **27**, pp.759-760.

[46] R. Krishnamurti, "Finite amplitude convection with changing mean temperature. Part 1. Theory", *J. Fluid Mech.*, (1968), **33**-3, pp.445-455.

[47] R. Krishnamurti, "Finite amplitude convection with changing mean temperature. Part 2. An experimental test of the theory", *J. Fluid Mech.*, (1968), **33**-3, pp.457-463.

[48] R. Krishnamurti, "On Cellular Cloud Patterns. Part 1: Mathematical Model", *J. Atmos. Sci.*, (1975), **32**, pp.1353-1363.

[49] R. Krishnamurti, "On Cellular Cloud Patterns. Part 2: Laboratory Model", *J. Atmos. Sci.*, (1975), **32**, pp.1364-1372.

[50] R. Krishnamurti, "On Cellular Cloud Patterns. Part 3: Applocability of the Mathematical and Laboratory Models", *J. Atmos. Sci.*, (1975), **32**, pp.1373-1383.

[51] R. C. J. Somerville and T. Gal-chen, "Numerical Symulation of Convection with Mean Vertical Motion", *J. Atmos. Sci.*, (1979), **36**, pp.805-815.

[52] Private comunication with M. Yoshizaki, Meteorological Research Institute, Japan.

[53] Private comunication with H. Ichikawa, Earthquake Research Institute, University of Tokyo, Japan

[54] M. Ciofalo, M. Signorino, M. Simiano, "Tomographic particle-image velocimetry and thermography in Rayleigh-Bénard convection using suspended thermochromic liquid crystals and digital image processing", *Exp. in Fluids*, (2003), **34**, pp.156-172.

[55] D. Dabiri, M. Gharib, "Digital particle image thermometry: The method and implementation", *Exp. in Fluids*, (1991), **11**, pp.77-86.

[56] N. Fujisawa, R. J. Adrian, "Three-dimensional Temperature Measurement in Turbulent Thermal Convection", *J. Visualization*, (1999), **1**, pp.355-364.

[57] I. Kimura, Y. Kuroe, M. Ozawa, "Application of neural networks to quantitative flow visualization", *J. Visualization Image Process*, (1993), **1**, pp. 261-269.

[58] N. Fujisawa, S. Funatani, "Simultaneous measurement of temperature and velocity in a turbulent thermal convection", *Exp. in Fluids*, (2000), **29**, pp.158-165.

[59] J. Aubert, D. Brito, H-C. Nataf, P. Cardin, J-P. Masson, "A systematic experimental study of rapidly rotating spherical convection in water and liquid gallium", *Phyis. of Earth & Planet. Int.*, (2001), **128**, pp.51-74.

[60] Manfored G. Braunsfurth and T. Mullin, "An experimental study of oscillatory convection in liquid gallium", *J. Fluid Mech.*, (1996), **327**, pp.199-219.

[61] D. Brito, P. Cardin, H.-C. Nataf, G. Marolleau, "Experimental study of a geostrophic vortex of gallium in a transverse magnetic field", *Phyis. of Earth & Planet. Int.*, (1995), **91**, pp.77-98.

[62] A. Juel, T. Mullin, H. B. Hadid, D. Henry, "Magnetohydrodynamic convection in molten gallium", *J. Fluid Mech.*, (1999), **378**, pp.97-118.

[63] D. Brito, D. Elbert, P. Olson, "Experimental crystallization of gallium: ultrasonic measurements of elastic anisotropy and implications for the inner core", *Phyis. of Earth & Planet. Int.*, (2001), **129**, pp.325-346.

[64] Y. Takeda, "Instantaneous Velocity Profile Measurement by Ultrasonic Doppler Method", *invited paper to the JSME Int. J.*, (1995), **B38**, pp.8-16.

[65] Y. Takeda, W. E. Fischer, J. Sakakibara, "Decomposition of modulated waves in a rotating Couette System", *Science*, (1994), **263**, pp.502.

[66] Y. Takeda, "Quasi-periodic state and transition to turbulence in a rotating Couette system", *J. Fluid Mech.*, (1996), **389**, pp.81-99.

[67] Y. Takeda, "Measurement of velocity profile of mercury flow by ultrasound Doppler shift method", *Nuclear Tech.*, (1987), **79**, pp.120-124.

[68] M. Mori, Y. Takeda, T. Taishi, N. Furuichi, M. Aritomi, H. Kikura, "Development of a novel flow metering system using ultrasonic velocity profile measurement", *Exp. in Fluids*, (2002), **32**, pp.153-160.

[69] D. Brito, H.-C. Nataf, J. Aubert, J.-P. Masson, "Ultrasonic Doppler velocimetry in liquid gallium", *Exp. in Fluids*, (2001), **31**, pp.653-663.

[70] H. Ozoe and T. Hara, "Numerical analysis for oscillatory natural convection of low Prandtl number fluid heated from below" *Num. Heat Trans.*, Part A, (1995), **27**, pp.307-317.

[71] B. Ouriev, E. Windhab, P. Braun, Y. Zeng and B. Birkhofer, "Industrial Application of Ultrasound Based in-Line Rheometry: Visualization of Steady Shear Pipe Flow of Chocolate Suspension in Pre-Crystallization Process", *Review of Scientific Instruments*, (2003), **74-12**, pp.5255-5259.

[72] B. Ouriev and E. Windhab, "Transient Flow of Highly Concentrated Suspensions Investigated Using the Ultrasound Velocity Profiler-Pressure Difference Method" *Meas. Sci. Technol.*, (2003), **14-11**, pp.1963-1972.

[73] M. J. W. Povey, "Ultrasonic Techniques for Fluids Characterization", Academic Press, (1997).

[74] R. T. Beyer and E. M. Ring, "Liquid metals: Chemistry and Physics", Marcel Dekker, New York (Chapter 9), (1972).

# Publication & Presentation

Chapter 2

## Theoretical Study on Effect of Distributed Internal Heat Source

Accepted by *Int. J. Heat & Mass Trans.*,

as "Effects of Heat Source Distribution on Natural Convection induced by Internal Heating".

Presented at *55th Annual Meeting, DFD-APS*, (2002),

as "Stability Analysis for the Natural Convection in Horizontal Fluid Layer driven by Internal Heat Generation".

Chapter 3

## Experiment on Internally Heated Convection

Submitted by *Phys. of Fluids*,

as "Dilatation of Convection Cell in the Natural Convection induced by Internal Heating".

Presented at *56th Annual Meeting, DFD-APS*, (2003),

as "Experimental Study on the Natural Convection induced by Internal Heating".

Chapter 4

## Temperature Behavior in Internally Heated Convection

Presented at *56th Annual Meeting, DFD-APS*, (2003),

as "Temperature Behavior of the Natural Convection induced by Internal Heating".

Chapter 5

## Ultrasonic Velocity Profile Measurement of Liquid Gallium Convection

Presented at *SEDI 2004*, (2004),

as "Measurements of velocity field for R-B convection and the characteristics of the flow pattern in liquid metal".

Presented at *57th Annual Meeting, DFD-APS*, (2004),

as "Ultrasonic Velocity Profile Measurement for Thermal Convection of Liquid Gallium".

## Appendix 2

## Optimum Seeding for Velocity Profile Measurement by UVP

Submitted by *Meas. & Sci. Technol.*,

as "Optimum seeding for velocity profile measurement by UVP".